# Precision Measurements with Rydberg States of Rubidium

by

Andira Ramos

A dissertation submitted in partial fulfillment
of the requirements for the degree of
Doctor of Philosophy
(Physics)
in The University of Michigan
2019

Doctoral Committee:

Professor Georg Raithel, Chair
Professor Timothy Chupp
Professor Duncan Steel
Associate Professor Kai Sun
Dr. Nicolaas Johannes Van Druten, University of Amsterdam.
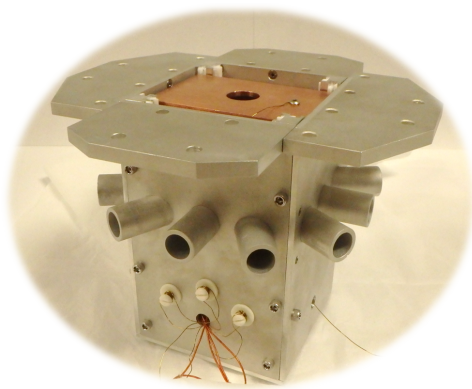
Andira Ramos

andramos@umich.edu

ORCID iD: 0000-0002-0086-8446

To my wonderful parents.

ACKNOWLEDGEMENTS

Graduate school has not been easy and I am extremely grateful to all the people in my life who have been there to help me through this journey. First, I want to thank my advisor, Georg Raithel, whose endless enthusiasm for physics is contagious. Georg, I truly appreciate the time you spent to answer questions, run calculations and listen to ideas, I know you were always very busy and yet somehow made sure to find time for meetings. You were always patient, understanding and supportive, I am happy to have had you as my research advisor.

Getting to work with current and past members of the Raithel group has also been amazing. Thanks to Jamie MacLennan, Ryan Cardman, Michael Viray, Lu Ma and Xiaoxuan Han. Jamie, your support knows no limits and it is a big reason why I have made it this far. Thank you for staying in the lab until the morning hours to keep me company while I ran experiments, thank you for editing applications, emails, and even this thesis (you are hired for life), thank you for the many surprise treats that so often cheered me up when the experiment was not cooperating. Most importantly, thank you for your friendship, it really means a lot. Ryan, thank you for being so willing to take over the experiment with such short notice before I left to Amsterdam, you did a wonderful job while I was gone. I really enjoyed running experiments with you and getting the chance to brainstorm together, you always impressed me with your clear grasp of physics theory and I know you have a bright future as a researcher. Michael, thank you for the work you do for the group and the graduate students in the department in general, you are great at creating and maintaining community.

very kind and made me feel welcomed from the very beginning. You all made the Netherlands feel like home, thank you.

Besides my research advisors, I was also very lucky to find a mentor in Dr. Christine Aidala. Thank you, Christine, for offering ice cream and listening to my worries during difficult times in my first year. You helped me feel like I belonged in the program and for that I will be forever grateful.

To my wonderful husband, Daniel, thank you for the many leaps of faith you have taken with me, from moving away from your family to quitting your job and moving to another continent, having you there with me through this journey has made it so much brighter. Thank you for your constant support, love and kindness, you have no idea how much energy you give me to keep on moving forward. I love you.

Thank you to my family who throughout these years has always been sending me love and warnings about winter storms. Spatially to my dear parents, Marisol and Rolando, who left two countries, family, friends and careers behind so that I could have better opportunities. I am deeply grateful for all the sacrifices you have made for me and I am always striving to make you proud. Thank you for your boundless love and support, you make me feel like I can do anything I set my mind to.

Lastly, I want to thank my committee, Duncan Steel, Tim Chupp, Kai Sun and

Klaasjan van Druten for their helpful revisions of this document.

TABLE OF CONTENTS

LIST OF FIGURES

LIST OF TABLES

ABSTRACT

Rydberg atoms can be excellent tools for precision metrology thanks to their long lifetimes and interactions with external fields and other atoms that scale with large powers of the principal quantum number. In this thesis I present a detailed description and characterization of an experimental setup I built to perform precision measurements with Rydberg atoms. In particular, this machinery was constructed to perform a precision measurement of the Rydberg constant, R_∞, using circular Rydberg atoms for which I also calculate and describe the expected sources of systematic uncertainties and how to manage them. Moreover, in this thesis I present precision measurements of the rubidium-85 $nS_{1/2}$ hyperfine structure (HFS) splittings.

Circular states are chosen for the precision measurement of R_∞ because they have longer lifetimes than low-l Rydberg atoms, negligible quantum-electrodynamics (QED) and no nuclear-overlap corrections. Due to these advantages, the measurement can help solve the "proton radius puzzle", which has cast doubts on the values of the proton radius and the Rydberg constant. In the pursued experiment, the atoms are trapped using a ponderomotive optical lattice, and transitions are driven using a recently-demonstrated lattice-modulation technique to perform Doppler-free spectroscopy. These methods allow us to exploit the long lifetime of the circular states while also yielding the necessary narrow linewidths. The circular-state transition frequency yields R_∞, after accounting for systematics. Laser wavelengths and beam geometries are selected such that the lattice-induced transition shift is minimized. The selected transitions have no first-order Zeeman and Stark corrections, leaving

only manageable second-order Zeeman and Stark shifts. For Rb, the projected relative uncertainty of R_∞ in a measurement under the presence of the Earth's gravity is 10^{-11}, with the main contribution coming from the residual lattice shift. This could be reduced in a future micro-gravity implementation.

I perform a precision measurement of the HFS splitting in rubidium-85. The splittings between the $F = 2$ and $F = 3$ of $nS_{1/2}$ atomic levels are obtained by driving $nP_{3/2} \rightarrow nS_{1/2}$ microwave transitions for $n = 43$ to 46. From the splittings the HFS constant is determined to be 15.37(17) GHz which is almost an order of magnitude improvement in precision from the value available in the literature. These experiments also prove the capabilities of the experimental setup.

CHAPTER I

Introduction

The exaggerated properties of Rydberg atoms have made them attractive for a wide range of experiments and applications in atomic, molecular and optical (AMO) physics. Rydberg atoms have been studied since the 1880s with the discovery of the Balmer series [8] but it was not until the 1970s, when the emergence of the laser made excitation to higher-n Rydberg states possible, that Rydberg atoms took center stage with studies of their properties, fine-structure levels, behaviour in applied external fields, and state-changing and ionization collisions [9]. By the 1990s, efforts in AMO physics were mostly turned to the development of cooling and trapping techniques, including optical molasses, magneto-optical traps (MOT), magnetic and optical traps, evaporative cooling [10–12], and Bose-Einstein condensates (BEC) [13, 14]. Still, in these years some interest remained on Rydberg atoms, in particular circular Rydberg atoms were used in cavity quantum electrodynamics (QED) experiments which led to a Nobel prize [15].

Since the 2000s Rydberg atoms have become a hot topic once more. Predictions of exotic molecular states composed in part of Rydberg atoms [16] gave way to many experiments to explore the exaggerated properties of these Rydberg molecules. Also, Rydberg atoms were introduced as candidates for quantum information [17] triggering another set of efforts world-wide [18]. Moreover, Rydberg atoms are popular

Table 1.1:
Scaling laws for Rydberg atoms. The Rydberg/ground comparison is done by dividing the respective properties for a Rydberg state (n=50) by those of a ground state (n=1) of the hydrogen atom.

	Scaling	Rydberg/ground Comparison
Size	n^2	2.5×10^3
Lifetime (low l)	n^3	1.25×10^5
Lifetime (high l)	n^5	3.1×10^8
Energy spacing between Rydberg levels	n^{-3}	8×10^{-6}
Polarizability	n^7	7.8×10^{11}

building blocks for emerging quantum technologies from DC [19] and RF electric-field sensors [20–22], to being one of the most promising avenues for making quantum computing a reality [18].

Rydberg atoms are also great candidates for precision measurements. Their long lifetimes enable longer interaction times with probing fields and hence narrower peak linewidths which in precision measurements is key for determining transition frequencies accurately. Moreover, their weakly bound electron makes it possible to trap Rydberg atoms and drive microwave transitions between these states using optical ponderomotive potentials. These lead to efficient trapping [1] and to Fourier-limited linewidths [23]. In the work discussed here, I present experiments that exploit these properties.

1.1   Rydberg Atoms

An atom is considered a Rydberg atom when it is excited to a high principal quantum number, n, and hence the valence electron is weakly bound to the nuclear core. With a high n come the exaggerated properties shown in Table 1.1 [24] where for contrast, the values of such properties for a Rydberg state of $n = 50$ and the hydrogen ground state, $n = 1$, are shown.

The large size of Rydberg atoms can be derived classically by employing the simplified Bohr atomic model where the electron is pictured to have a circular orbit around the positively charged atomic nucleus and they are bound by their Coulomb interaction

$$\frac{m_e v^2}{r} = \frac{ke^2}{r^2},$$ (1.1)

where m_e, e, v are the electron mass, charge and linear speed respectively, r is the distance between the electron and the nucleus and k is Coulomb's constant. Note that throughout this thesis, I will use SI units unless otherwise stated.

Using Bohr's idea that angular momentum is quantized, $L = n\hbar$ (where $L = rvm_e$ and $\hbar$ is the reduced Planck's constant) and substituting into Eq. 1.1, one obtains an expression for the distance from the nucleus as a function of the principal quantum number that shows the n^2 scaling

$$r = \frac{n^2\hbar^2}{m_e ke^2}.$$ (1.2)

Another important feature of this expression is its inverse relation with mass. In other words, if we were to substitute the electron with a more massive particle that is also negatively charged (such as a muon), we would obtain an orbital radius that is smaller. The relevance of this point will become clear towards the end of this chapter.

Even though the Bohr model of the atom was useful for understanding the discrete atomic energy levels of hydrogen, it did not describe properties like electron spin and atomic lifetimes [25, 26]. The advent of quantum mechanics resolved the dead-end that semi-classical approaches led to. In context with my work, the lifetime scaling of atomic energy levels is important and in order to calculate them we must take a full quantum route. To do so, let us introduce the Einstein coefficient, $A_{n'l',nl}$, which describes the rate at which spontaneous emissions from the excited state $n'l'$ to the

lower state nl occur [24] and it is

$$A_{n'l',nl} = \frac{e^2 \omega_{nl,n'l'}^3}{3\pi\epsilon_0 \hbar c^3} \frac{l_{max}}{2l+1} | \langle n'l'|\hat{r}|nl\rangle |^2, \tag{1.3}$$

where $\omega_{nl,n'l'}$ is the transition frequency between states $n'l'$ and nl, c is the speed of light, ϵ_0 is the permittivity of free space, l is the angular momentum quantum number, l_{max} is the largest value between l and l' and $\langle n'l'|\hat{r}|nl\rangle$ is the radial matrix element with $\hat{r}$ the position operator.

To explain the long lifetimes $(1/A_{n'l',nl})$, we consider the radial matrix element and $\omega_{nl,n'l'}$. When the transition frequency is large, the radial matrix element is small and vice versa, resulting in long Rydberg-state lifetimes. The exact scaling shown in Table 1.1 for low l comes from the fact that at large n the transition frequency between Rydberg and low-lying states is approximately independent of n (since the larger the n the smaller the spacing between states becomes, as shown by the n^{-3} scaling in Table 1.1), leaving only the radial matrix element squared which due to the small wavefunction overlap has an n^{-3} dependency.

For high l, due to selection rules, the only decay channels are to nearby high-n, high-l states, which means that the transition frequency is no longer n-independent and that it is governed by a n^{-3} scaling, n^{-9} when raised to the third power. This combined with the n^4 scaling from the radial matrix element squared results in a transition rate scaling of n^{-5} and therefore a lifetime scaling of n^5.

Of course, there are external effects that can decrease a state's lifetime such as blackbody radiation and atom-atom collisions. The former has a high impact on Rydberg atoms because the typical blackbody spectrum matches well with the transition frequencies between Rydberg states. A more thorough discussion on this topic will be done in Chapter II.

Finally, the scaling of the energy spacing between the Rydberg levels simply comes

from the energy having a n^{-2} dependency and therefore $dE/dn = -2n^{-3}$. The scaling of the polarizability results from a combination of the scaling of the dipole matrix elements squared (n^4) and the transition energies (n^{-3}) [24, 27].

1.2 Rydberg Constant

The Rydberg constant, R_∞, is a key physical constant which is employed in determining atomic energy levels of any atom through the Rydberg formula,

$$E_n = \frac{chR_\infty}{n^2},$$

(1.4)

where E_n is the atomic energy associated with the principal quantum number, n.

Moreover, the Rydberg constant is related to other fundamental constants by

$$R_\infty = \frac{m_e e^4}{8\epsilon_0^2 h^3 c} = \frac{\alpha^2 m_e c}{2h},$$

(1.5)

where α is the fine structure constant. The fact that atomic levels of all existing elements can be calculated using R_∞ and that several constants depend on it make the Rydberg constant a highly important fundamental constant.

This has led to decades of measurements to determine R_∞ precisely (see Table 1.2). Most commonly, to obtain the Rydberg constant, transition frequencies between low-lying states of hydrogen and deuterium (an isotope of hydrogen with a single neutron in the nucleus) are measured, limited typically by statistical uncertainties, AC Stark shifts and second-order Doppler shifts. Over the years, improvements to the precision of R_∞ were attained in part thanks to the introduction of lasers and advancements in laser stability and frequency reference sources. This resulted in an improvement in the relative uncertainty of R_∞ of four order of magnitudes over three decades [28, 29] (see Table 1.2).

Table 1.2:
The Rydberg constant values and their relative uncertainties through the years as determined by the Committee on Data for Science and Technology (CODATA). These values take into account experimental results obtained world-wide with the most competitive uncertainties up to a given year.

Year	Rydberg constant value (m^{-1})	Relative Uncertainty	Ref.
1973	10 973 731.77(83)	7.5 $\times 10^{-8}$	[28]
1986	10 973 731.534(13)	12 $\times 10^{-10}$	[30]
1998	10 973 731.568 549(83)	7.6 $\times 10^{-12}$	[31]
2002	10 973 731.568 525(73)	6.6 $\times 10^{-12}$	[29]
2006	10 973 731.568 527(73)	6.6 $\times 10^{-12}$	[32]
2010	10 973 731.568 539(55)	5.0 $\times 10^{-12}$	[33]
2014	10 973 731.568 508(65)	5.9 $\times 10^{-12}$	[34]

Besides low-lying states of hydrogen, there has also been a study involving circular Rydberg states of hydrogen [35] (relative uncertainty of 2.1×10^{-11}) and a proposal involving circular states of lithium [36] (expected relative uncertainty of about 10^{-10}). However, it has been the experiments with low-lying states which have led to the current value of the Rydberg constant of 10 973 731.568 508(65) m^{-1} with an uncertainty of almost 1 part in a trillion or more specifically 5.9×10^{-12} [34]. This makes R_∞ one of the currently best-known constants.

1.2.1   The Proton Radius Puzzle

The value of the Rydberg constant started to be questioned in 2010, with the appearance of the "proton radius puzzle" [37]. The puzzle arouse when a spectroscopy experiment done with muonic hydrogen yielded a proton radius significantly smaller (5.6σ away) than previously obtained values [38]. Muonic hydrogen consists of a hydrogen atom where the electron has been replaced by a muon, a particle that is also negatively charged but about 207 times more massive than the electron. As a result, the orbit of the muon is smaller than that of the electron (see Eq. 1.2), making it more susceptible to nuclear effects.
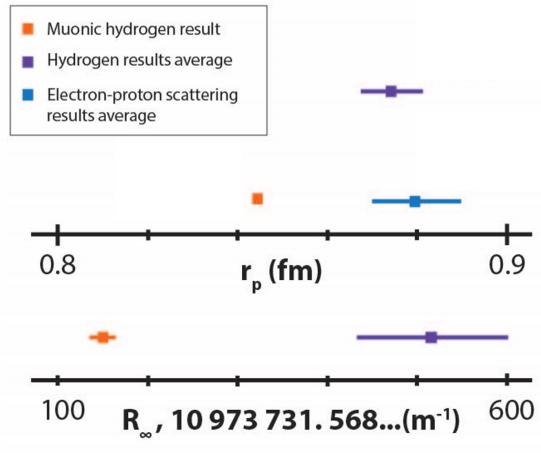
Figure 1.1: Proton radius (top) and Rydberg constant (bottom) values obtained using different approaches. The error bars for the proton radius obtained with muonic hydrogen spectroscopy are not visible in the scale on the top.

This led to the value of the proton radius extracted from the muonic spectroscopy to have a relative uncertainty that is an order of magnitude better than that of CODATA, which combines results from hydrogen spectroscopy and electron scattering experiments [34] (see Fig. 1.1). The smaller proton radius value and higher precision of the muonic hydrogen results triggered many efforts throughout various sub-fields of physics to both check previous results and to search for new physics [38].

The proton size and the Rydberg constant are connected through the finite nuclear size correction [33, 39]

$$
\begin{aligned}
E_{NS} &= \delta_{l0} \frac{2}{3} \left(\frac{m_r}{m_e} \right)^3 \frac{\alpha^2 m_e c^2}{n^3} \left(\frac{2\pi Z \alpha r_N}{\lambda_c} \right)^2 & (1.6) \\
&= \delta_{l0} \frac{4}{3} \left(\frac{m_r}{m_e} \right)^3 \frac{h R_\infty c}{n^3} \left(\frac{2\pi Z \alpha r_N}{\lambda_c} \right)^2, & (1.7)
\end{aligned}
$$

where Z is the effective nuclear charge ($Z = 1$ for hydrogen and alkali metals), $m_r = m_e m_N / (m_e + m_N)$ is the reduced mass with m_N the nuclear mass, r_N is the root-mean-square (rms) charge radius of the nucleus, λ_C is the Compton wavelength of

the electron and the second line is obtained using Eq. 1.5. This correction accounts for the finite size of the nucleus, which is typically approximated to be a point-charge. To extract the proton radius, Eq. 1.4 and Eq. 1.6, along with other energy shifts and quantum-electrodynamics (QED) corrections, are added and compared to experimentally obtained atomic transition frequencies. Hence, the discrepancy found in the radius of the proton could be actually due to a discrepancy in R_∞ or the other corrections being added to the energy level calculations.

If the source of the discrepancy were R_∞, the Rydberg constant would have to be changed by more than 5σ or, put a different way, its value would change by 0.000351 m^{-1} [34] (see Fig. 1.1). Consequently, the constants which are related to R_∞ would also need to be adjusted (see Eq. 1.5), causing a domino effect. Another possibility is that the QED corrections used to extract the proton radius are the source of the discrepancies, in particular the two-photon exchange contributions [38].

In an attempt to solve the puzzle, there has been several efforts involving spectroscopy of other muonic atoms [40], improved spectroscopic measurements of hydrogen transitions [41, 42], a proposal to measure the Rydberg constant using high-angular-momentum states of hydrogen-like ions [43], new electron-proton scattering experiments [38], and a proposal to perform a muon-proton scattering experiment [44], to name a few. Despite these efforts, the puzzle remains unsolved. Part of my thesis work has been to build and characterize an experimental setup geared to measuring the Rydberg constant independently from the radius of the proton. This would serve as part of an elimination process to find the true cause of the puzzle and consequently aid in solving it.

1.2.2   Measuring R_∞ with Circular States

We propose an experiment to obtain an independent measurement of the Rydberg constant using cold, trapped circular Rydberg atoms. Circular Rydberg atoms
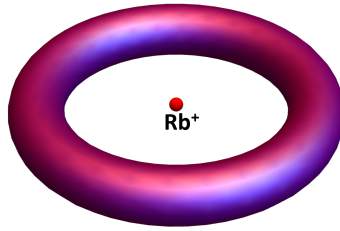
Figure 1.2: Sketch of the probability density $|\psi|^2$ of the Rydberg electron in a circular state. Near the Rb$^+$ core, $|\psi|^2 = 0$. (figure not to scale).

are those where the magnetic quantum number, m_l, is the highest possible $(n-1)$. Since circular atoms are also Rydberg atoms, they have the exaggerated properties presented in Table 1.1. Moreover, they have even longer radiative lifetimes (on the order of ms) [24], small QED corrections [45] and no overlap with the nucleus, hence eliminating nuclear charge distribution effects (see Fig. 1.2).

In contrast with previous efforts to measure R_∞ [29, 33], it is proposed to trap cold rubidium Rydberg atoms using a ponderomotive potential optical lattice (POL) [1] instead of using cold atomic beams of hydrogen or deuterium. Trapping the atoms allows for increased interaction times which can be fully exploited thanks to the long lifetimes of circular states and leads to narrower spectral lines. The use of rubidium makes using well established cooling techniques possible, this reduces Doppler effects and limits the fields inhomogeneities the atoms are exposed to.

Another key departure from previous efforts is that transition frequencies between two high-m_l states will be measured and used to extract the Rydberg constant. Typically, transitions always involving at least one S-state in hydrogen or deuterium are used, resulting in a heavy dependence on QED theory and the proton size. The use of circular states removes these dependencies and allows us to verify whether R_∞ is the source of the proton radius puzzle.

The use of rubidium, however, means that quantum defects, corrections added to the hydrogenic energy eigenvalues to account for the ionic core of rubidium, need to

be included. This correction, however, is not predicted to prevent us from reaching comparable precision to the one currently available. Still, careful consideration must be given to any sources of systematic uncertainties that can shift or widened the spectral line if we are to achieve such precision.

1.3 Thesis Outline

This dissertation presents experimental process towards a proposed precision measurement of the Rydberg constant using circular Rydberg atoms. I start by introducing the mathematical formalism needed to work with circular and near-circular states in Chapter II. I apply this formalism to obtain expressions for the energy-level shifts affecting the transition of interest in the Rydberg constant measurement. This makes identifying the main sources of uncertainty possible. Furthermore, it gives information on the feasibility of the experiment and what uncertainty sources need to be lowered to achieve a competitive result.

Two of the largest sources of uncertainty are due to electric and magnetic fields, hence good control of these is imperative to obtain a precise enough R_∞. A comprehensive description of the experimental setup is given in Chapter III. In particular, I discuss details on the control and characterization of the electric and magnetic fields, as well as the laser system, microwave spectroscopy and cooling used and cicularization methods considered.

This same experimental setup is used to make precision measurements of the $nS_{1/2}$ hyperfine structure splittings in rubidium-85 which are presented in Chapter IV. These measured splittings lead to a determination of the hyperfine structure constant that is almost an order of magnitude more precise than the currently best available in the literature. This experiment also serves to prove the capability of the experimental setup to achieve good field control.

In Chapter V, I present the values of the expected energy shifts in the Rydberg

constant measurement along with a detailed discussion of the uncertainties in each shift, their sources and how to mitigate them. Lastly, in Chapter VI I discuss the improvement of these uncertainties in micro-gravity conditions, the implications of the expected ground-based uncertainty to the proton radius puzzle and future experiments that can be performed in the newly constructed experimental setup.

Finally, in the Appendix, I discuss the work I did while at the University of Amsterdam (as part of a grant from the National Science Foundation) where I implemented an optical lattice to an existing atom-chip setup to improve atomic confinement.

CHAPTER II

Theoretical Background

To extract exact energy levels from which to determine atomic constants, any possible perturbations to the spectral lines must be taken into account. Included in these perturbations are energy shifts and spectral-line broadening. Energy shifts are detrimental because they alter the actual frequency value that one is trying to measure while spectral-line broadening makes it more difficult to determine the line center accurately. Hence, these undesired effects should be accounted for and minimized or even eliminated whenever possible.

In this chapter, I present a careful analysis of the expected perturbations for the proposed measurement of the Rydberg constant along with ways that I can use to minimize or eliminate them experimentally. In Chapter V, I show an expected uncertainty budget and discuss the different sources of uncertainty.

2.1   Mathematical Formalism for Circular States

Circular states are degenerate with other high-l hydrogenic states unless a static electric field is applied. Consequently, whenever circular states are being used, a DC electric field needs to be present to prevent mixing with the hydrogenic manifold and l is no longer a good quantum number. Under this new symmetry it becomes more natural to switch from spherical to parabolic coordinates. In the Paschen-Back

regime, the new quantum numbers become $\{|n, n_1, n_2, m_l, m_s\rangle\}$ [46], where m_s is the spin quantum number, and n_1 and n_2 are the parabolic quantum numbers which can have values from zero to $n-1$. These parabolic quantum numbers describe the amount of confocal parabolas, and hence the number of nodes, that outline the shape of the probability distribution of the Rydberg electron. The parabolic quantum numbers are related by $n = n_1 + n_2 + |m_l| + 1$.

In Fig. 2.1 four examples of cuts on the x-z plane of the probability density of parabolic states are shown, with the quantization axis (defined by the electric field) along the z-direction. The top left panel shows an example of a circular state. For this state, $n_1 = n_2 = 0$, which leads to no confocal parabolas. The top right panel shows the case where $n_1 = 0, n_2 = 1$, where a parabola with positive concavity and its focus along $x = 0$ can be drawn between the two pairs of lobes. Therefore, n_2 defines the number of confocal parabolas with positive concavity. Similarly, in the bottom left panel $n_1 = 2, n_2 = 0$, hence there are no parabolas facing up but two facing down as determined by n_1. Finally, in the bottom right panel, $n_1 = n_2 = 1$ and two confocal parabolas, one facing up and one facing down, can be drawn between the lobes.

Another important detail that the parabolic quantum numbers n_1 and n_2 can give is the polarization direction of the probability distribution. For example, for the top right panel $n_2 > n_1$ and therefore the Rydberg electron is more likely to be found in the negative z direction. Similarly, in the bottom right panel $n_1 > n_2$ and the Rydberg electron is more likely to be found in the positive z direction. Whenever $n_1 = n_2$, like it is the case for the top left and bottom right panels, the electron is equally likely to be found in the positive or negative z direction.
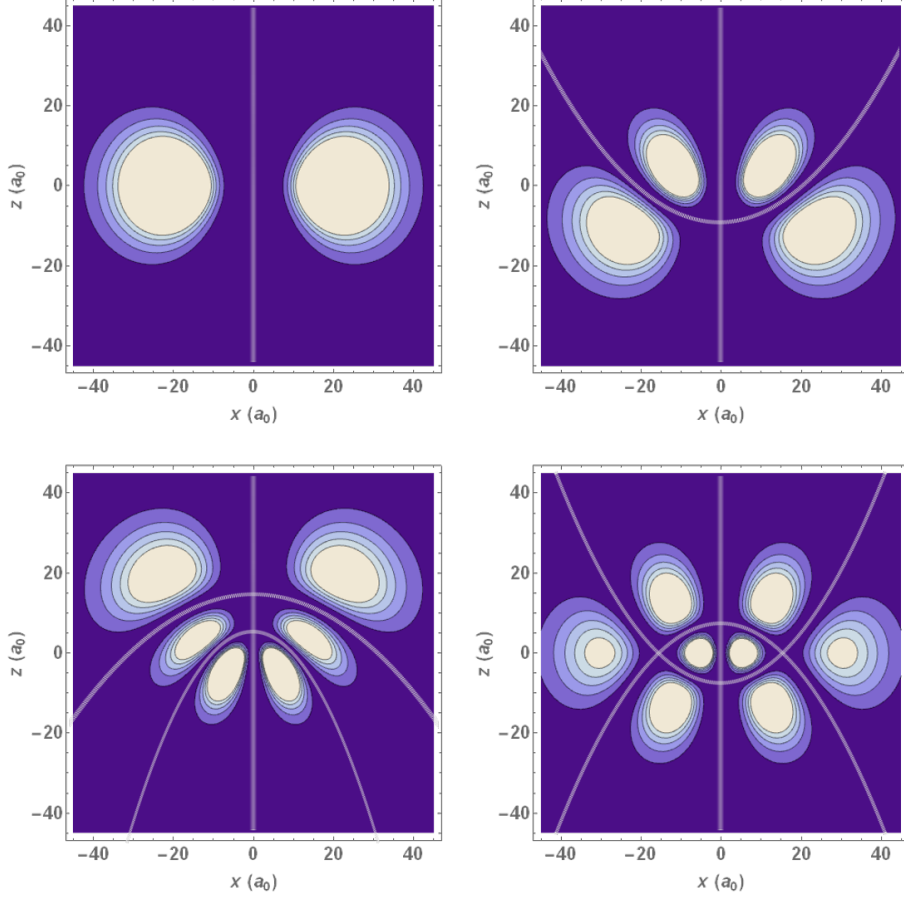
Figure 2.1: Rydberg electron probability distributions for different parabolic quantum numbers. Top left: $n_1 = n_2 = 0, m_l = 4$; top right: $n_1 = 0, n_2 = 1, m_l = 3$; bottom left: $n_1 = 2, n_2 = 0, m_l = 2$; bottom right: $n_1 = n_2 = 1, m_l = 2$ (all have $n = 5$).

2.1.1 Parabolic Coordinates

Parabolic coordinates are related to spherical coordinates as follows [24]:

$$\xi = r + z = r(1 + cos\theta) \tag{2.1}$$

$$\eta = r - z = r(1 - cos\theta) \tag{2.2}$$

$$\phi = tan^{-1}(y/x), \tag{2.3}$$

where the constant surfaces of ξ or η form paraboloids with the z-axis as their symmetry axis (see Fig. 2.1). The Schrödinger equation in this coordinate system with

14

an electric field along the z direction can still be separated [46] and the resulting normalized wavefunction is

$$\psi_{n,n_1,n_2,m_l} = \frac{n_1!^{1/2}n_2!^{1/2}}{(n_1+m_l)!^{3/2}(n_2+m_l)!^{3/2}}e^{-Z/2n(\xi+\eta)}\frac{e^{im_l\phi}}{\sqrt{n\pi}}\left(\frac{Z}{n}\right)^{m_l+3/2}$$
$$\times(\xi\eta)^{m_l/2}L_{n_1}^{m_l}\left(\frac{Z\xi}{n}\right)L_{n_2}^{m_l}\left(\frac{Z\eta}{n}\right),$$

(2.4)

where $L_p^q(x)$ are the generalized Laguerre polynomials.

2.1.2 Relation between Spherical and Parabolic States

Due to their toroidal shape, circular states can also be expressed in the spherical basis with l as a good quantum number ($l = n-1$ for all circular states). However, as soon as the parabolic quantum numbers differ from zero, we can no longer use a single spherical wavefunction to describe the atomic state but a sum of them. Parabolic and spherical bases are related by [24]

$$|n, n_1, n_2, m_l\rangle = \sum_l C_{l,m_l}^{n_1,n_2}|n, l, m_l\rangle,$$

(2.5)

where the modified Clebsch-Gordan coefficients are related to the Wigner 3J symbols by [24] $C_{lm_l}^{n_1n_2} = \langle n, n_1, n_2, m_l|n, l, m_l\rangle$,

$$C_{lm_l}^{n_1n_2} = (-1)^{(1-n+m_l+n_1-n_2)/2+l}\sqrt{2l+1} \times \begin{pmatrix} \frac{n-1}{2} & \frac{n-1}{2} & l \\ \frac{m_l+n_1-n_2}{2} & \frac{m_l-n_1+n_2}{2} & -m_l \end{pmatrix}.$$

(2.6)

In the remaining of this work, I will express atomic states following this format.

2.2 Energy Corrections

So far, I have emphasized the need for a DC electric field to be present in order to have well-defined circular states. However, the circularization method that I will

describe in Chapter III also requires a parallel DC magnetic field to be present. The most suitable stabilization scheme is one where $(3/2)nF > B/2$ (in atomic units) since this leads to circular states being less sensitive to stray electric fields. For the high-l state of interest here, the presence of this magnetic field of non-negligible amplitude ($\approx 10\ \mu$T$= 100$ mG) puts us in the Paschen-Back regime, where the energy splitting caused by the Zeeman shift (≈ 100 kHz) is larger than that of the fine structure correction (≈ 1 kHz). As a result, $\{|n, n_1, n_2, m_l, m_s\rangle\}$ is the most appropriate basis. In what follows, I present the energy corrections that need to be taken into account for the Rydberg constant measurement using this basis.

2.2.1 Quantum Defects

Alkali atoms are attractive to work with in part because they have a single valence electron. As a result, theoretical results obtained for hydrogen can also be adapted to atoms such as Rubidium which simplifies calculations greatly. One important difference between hydrogen and the alkalis is that the latter contain an ionic core, formed by the inner electrons and the nucleus. The interaction between the valence electron and the ionic core brings changes to the hydrogenic eigenvalues which are accounted for through the quantum defects as follows [24, 47]

$$E = -hcR_{\mathrm{Rb}}\frac{1}{(n^*)^2} = -hcR_{\mathrm{Rb}}\frac{1}{(n - \delta_l)^2}, \tag{2.7}$$

where $R_{\mathrm{Rb}} = \frac{M}{m_{\mathrm{e}}+M}\ R_\infty$ (M is the mass of Rb$^+$), n^* is called the effective principal quantum number and δ_l is the quantum defect. For high-l Rydberg states, such as circular states, $\delta_l \ll 1$ and Eq. 2.8 can be expanded as

$$E = -hcR_{\mathrm{Rb}}\left[\frac{1}{n^2} + \frac{2\delta_l}{n^3} + ...\right], \tag{2.8}$$

showing the n^{-3} dependency attributed to the quantum defect correction.

16

Table 2.1: Current experimentally determined quantum defects of rubidium.

l-state	δ_0	δ_2	Ref.
$ns_{1/2}$	3.131 180 4(10)	0.1784(6)	[49]
$np_{1/2}$	2.654 884 9(10)	0.2900(6)	[49]
$np_{3/2}$	2.641 673 7(10)	0.2950(7)	[49]
$nd_{3/2}$	1.348 091 71(40)	-0.602 86(26)	[49]
$nd_{5/2}$	1.346 465 72(30)	-0.596 00(18)	[49]
$nf_{5/2}$	0.0165192(9)	-0.085(9)	[50]
$nf_{7/2}$	0.0165437(7)	-0.086(7)	[50]
ng	0.004 00(2)	-0.018(15)	[48]

The quantum defect, δ_l is typically expanded using the Ritz formula as [48]

$$\delta_l(n) = \delta_0 + \frac{\delta_2}{(n - \delta_0)^2}, \tag{2.9}$$

where δ_0 and δ_2 are constants [49]. Table 2.1 shows experimentally determined values for δ_0 and δ_2 for different l-states of rubidium. Reference [48] also lists results for the quantum defect, $\delta_l(n)$, of the nh series for n=28, 29 and 30, but does not evaluate δ_l or δ_0 and δ_2. Taking a weighted average for these three n-values one finds a $\delta_{l=5}$ of 0.001 407 (20).

The second term in Eq. 2.8 can be further expanded into the polarization (δ_{pol}) and penetration (δ_{pen}) quantum defects terms. The polarization quantum defect comes from the polarization of the ionic core by the valence electron and the penetration quantum defect from interactions that occur when the valence electron overlaps spatially with the ionic core. These quantum defects are related by $\delta_l = \delta_{\mathrm{pol}} + \delta_{\mathrm{pen}}$.

In the proposed experiment, where transitions from circular to near-circular states are driven, $\delta_{\mathrm{pen}} = 0$ because the probability density of circular Rydberg states can be taken to be zero in the ionic core region (Fig. 1.2). Core polarization, however, must still be considered, with the shift due to the effective dipole polarizability, α'_{d}, being the leading term, followed by an almost negligible shift due to the effective quadrupole polarizability, α'_{q}. We can treat this quantum defect term as a perturbation where

the polarization potential is given by [51]

$$\hat{V}_{\text{pol}} = \frac{-e^2}{16\pi^2\epsilon_0^2} \left[\frac{1}{2} \frac{\alpha_d'}{\hat{r}^4} + \frac{1}{2} \frac{\alpha_q'}{\hat{r}^6} + ... \right], \tag{2.10}$$

where the values of α_d' and α_q' are obtained from [48] and can be converted to SI units [27]. The analytically known expressions for $\langle r^{-4} \rangle$ and $\langle r^{-6} \rangle$ in atomic units are [47]

$$\langle r^{-4} \rangle = \frac{3n^2 - l(l+1)}{2n^5(l - \frac{1}{2})l(l + \frac{1}{2})(l+1)(l + \frac{3}{2})}, \tag{2.11}$$

$$\langle r^{-6} \rangle = \frac{35n^4 - 5n^2(6l(l+1) - 5) + 3(l-1)l(l+1)(l+2)}{8n^7(l - \frac{3}{2})(l-1)(l - \frac{1}{2})l(l + \frac{1}{2})(l+1)(l + \frac{3}{2})(l+2)(l + \frac{5}{2})}. \tag{2.12}$$

For $4 \lesssim l \ll n$, Eq. 2.10 leads approximately to a δ_{pol} of (in atomic units)

$$\delta_{\text{pol}} \approx \frac{3}{4} \frac{\alpha_d'}{l^5} \left[1 - O_d \left(\frac{l^2}{n^2} \right) \right] + \frac{35}{16} \frac{\alpha_q'}{l^9} \left[1 - O_q \left(\frac{l^2}{n^2} \right) \right], \tag{2.13}$$

where the $O(l^2/n^2)$ are higher order terms. Since the present experiment requires high precision, and because the numerators in Eq. 2.11 change significantly for l approaching n, in the proposed experiment, where high-angular-momentum states are employed, the exact analytic expressions for $\langle r^{-4} \rangle$ and $\langle r^{-6} \rangle$ above need to be used.

The quadrupole term in Eq. 2.10 becomes negligible at large r values such as the ones found in circular Rydberg states. The dipole polarizability term leads to corrections of the order of a hundred Hz.

2.2.1.1 Polarizabilities

The polarizabilities in the polarization quantum defect are not well known. The most recent experimental limits are $\alpha_d' = 9.12(2)$ and $\alpha_q' = 14(3)$ (in atomic units) [48]. While the value for the dipolar polarizability is in rough agreement with previous theoretical and experimental values, the quadrupolar polarizability is not consistent

Table 2.2:
Calculated shifts for the dipole and quadrupole terms of the polarizability quantum defect potential in Eq. 2.10 for circular states at different principal quantum numbers, n.

n	Δ_d (kHz)	Δ_q (mHz)	$|\Delta_q/\Delta_d|(\times 10^{-6})$
25	-222	-1050	4.73
30	-50.6	-112	2.21
35	-14.5	-17.0	1.17
40	-4.94	-3.33	0.674
45	-1.91	-0.792	0.415
50	-0.816	-0.220	0.270

with any. The current uncertainties in the experimental values of polarizabilities are of order 10^{-3}, which lead to a relative uncertainty of the order of 10^{-12} in the proposed Rydberg constant measurement, making this one of the main sources of uncertainty.

2.2.1.2 Non-adiabatic Effects

The quantum defect theory discussed so far assumes that the Rb^+ response to the Rydberg electron's field is adiabatic. However, this is not necessarily the case. The non-adiabaticity of the electron's motion makes it necessary to redefine $\hat{V}_{\text{pol}}$ [52] and hence the polarizabilities as

$$\hat{V}_{\text{pol}} = \frac{-e^2}{16\pi^2\epsilon_0^2}\left[\frac{1}{2}\frac{\alpha_{\text{d}}\ y_0^d}{\hat{r}^4} + \frac{1}{2}\frac{\alpha_{\text{q}}\ y_0^q + \alpha_{\text{d}}\ y_1^d}{\hat{r}^6} + ...\right],\qquad(2.14)$$

where y_0^d, y_1^d, and y_0^q vary slowly with n and l. Comparing this expression to Eq. 2.10, we see that the corrected and the adiabatic polarizabilities are related as follows: $\alpha_{\text{d}}' = y_0^d\alpha_{\text{d}}, \alpha_{\text{q}}' = y_0^q\alpha_{\text{q}} + y_1^d\alpha_{\text{d}}$ [47]. Using Ref. [53] the corrected dipolar and quadrupolar polarizabilities can be calculated for ^{85}Rb. However, in the calculations presented here, experimentally-determined values for the polarizabilities are used which already include the non-adiabatic correction, hence no further corrections are needed.

2.2.2 Fine Structure Correction

For $S_{1/2}$, the fine structure correction is normally associated with a single nl-energy level splitting into two spectral lines, one for spin up and another for spin down. In general, however, when referring to fine-structure correction, there are multiple terms that are taken into account, all of which have an α^4 dependency: the relativistic mass correction, the spin-orbit coupling and the Darwin term [25]. To obtain the fine-structure corrections, one can either use perturbation theory or Dirac's theory which follows a fully relativistic approach [46]. In the following, I will present each term using perturbation theory. Since I am working with Rydberg atoms with large l, the form of the fine-structure shift is the same as for the hydrogen atom.

2.2.2.1 Spin-Orbit Coupling

The spin-orbit coupling arises due to interactions between the ionic core positive charge and the valence electron spin. In the frame of reference of the electron, the positive core moves around it creating a magnetic field, $\mathbf{B}$, which couples to its spin via $-\boldsymbol{\mu}_e \cdot \mathbf{B}$, where $\boldsymbol{\mu}_e$ is the spin magnetic moment. Using $\mathbf{B} = \frac{1}{c^2} \mathbf{v} \times \mathbf{E} = \frac{1}{c^2} \mathbf{v} \times \frac{e^2}{4\pi\epsilon_0} \frac{\mathbf{r}}{r^3}$, We can rewrite $\mathbf{B}$ in terms of the angular momentum $\mathbf{L}$ as $\mathbf{B} = \mu_0 e \mathbf{L} / 4\pi m_e r^3$. We can also write $\boldsymbol{\mu}_e$ in terms of the spin angular momentum, $\mathbf{S}$, as $\boldsymbol{\mu}_e = (g_e e / 2m_e) \mathbf{S}$ where g_e is the electron's g-factor (≈ 2).

If we put everything up to this point together we would get a spin-orbit Hamiltonian that would be too large by a factor of two. The missing $1/2$ comes from the Thomas precession which results from performing Lorentz transformations for a non-inertial frame of reference [54].

Adding the Thomas precession to everything else and using $\alpha = \mu_0 e^2 c / 4\pi\hbar$ I obtain the correct spin-orbit coupling Hamiltonian

$$\hat{H}_{\text{SO}} = \frac{\alpha\hbar}{2m_{\text{e}}^2 c} \frac{1}{\hat{r}^3} \hat{\mathbf{L}} \cdot \hat{\mathbf{S}}. \tag{2.15}$$

For a parabolic state in the Paschen-Back regime, this leads to an energy correction of

$$E_{\mathrm{SO}} = \frac{\alpha^4 m_{\mathrm{e}} c^2}{2} \sum_l |C_{lm_{\mathrm{l}}}^{n_1 n_2}|^2 \frac{m_{\mathrm{l}} m_{\mathrm{s}}}{n^3 l(l+1)(l+\frac{1}{2})}, \tag{2.16}$$

where $C_{lm_{\mathrm{l}}}^{n_1 n_2}$ is given in Eq. 2.6.

2.2.2.2 Relativistic Energy Correction

The relativistic contribution to the fine-structure shift results from replacing the classical kinetic energy of the electron, $p^2/(2m_e)$, in the Schrödinger equation with the more accurate relativistic expression, $\sqrt{p^2 c^2 + m_e^2 c^4} - m_e c^2$, where the term in the square-root is the total relativistic energy and the last term is the rest energy of the electron. Expanding this for small p we obtain

$$\frac{p^2}{2m_e} - \frac{p^4}{8m_e^3 c^2} + \dots \tag{2.17}$$

Therefore, we can include the relativistic kinetic energy by simply using first-order perturbation theory to add a correction to the previously obtained results of the Schrödinger equation. This yields a correction Hamiltonian of [25]

$$\hat{H}_{\mathrm{rel}} = -\frac{\hat{\mathbf{P}}^4}{8m_{\mathrm{e}}^3 c^2}. \tag{2.18}$$

Following the same procedure presented in [25], we can write $p^4 = 4m_e^2(\hat{H}_0 - \hat{V})^2$, where $\hat{H}_0 = \hat{p}^2/(2m_e)$ and $\hat{V} = e^2/(4\pi\epsilon_0 \hat{r})$ and arrive at a relativistic shift of

$$E_{\mathrm{rel}} = -\frac{\alpha^4 m_{\mathrm{e}} c^2}{2} \sum_l |C_{lm_{\mathrm{l}}}^{n_1 n_2}|^2 \left[\frac{1}{n^3(l+\frac{1}{2})} - \frac{3}{4n^4} \right]. \tag{2.19}$$

2.2.2.3 Darwin Term

Finally, the Darwin term takes into account uncertainties in the exact location of the valence electron due to the "Zitterbewegung", a QED effect. The Darwin term Hamiltonian is

$$\hat{H}_{\text{Darwin}} = -\frac{\pi\hbar^2}{2m_{\text{e}}^2 c^2} \frac{Ze^2}{4\pi\epsilon_0} \delta^3(\hat{\mathbf{r}}), \tag{2.20}$$

where $\delta^3(\hat{\mathbf{r}})$ is the delta function, which is zero everywhere except at $r = 0$. In other words, the Darwin term is only non-zero for s-states and hence does not play a role in the proposed measurement.

Putting together the fine structure terms relevant to the states of interest, we obtain the energy shift

$$E_{\text{FS}} = -\frac{\alpha^4 m_e c^2}{2n^3} \sum_l |C_{lm_l}^{n_1 n_2}|^2 \left[\frac{-m_l m_s}{l(l+1)(l+\frac{1}{2})} + \left(\frac{1}{(l+\frac{1}{2})} - \frac{3}{4n} \right) \right]. \tag{2.21}$$

As an example, for the $n = 51$ circular state, the relativistic correction is around 6 kHz while the spin-orbit correction is around 200 Hz.

In Dirac theory, where a full relativistic treatment is done with no magnetic field present, the energy levels are

$$E_{\text{Dirac}} = \frac{m_e c^2}{\sqrt{1 + \frac{Z^2\alpha^2}{\left[n-j-\frac{1}{2}+\sqrt{(j+\frac{1}{2})^2 - Z^2\alpha^2}\right]^2}}}, \tag{2.22}$$

where $j = l\pm(1/2)$ is the total angular momentum quantum number. This expression, when expanded in powers of α^2 yields the same results as perturbation theory in the presence of no magnetic fields.

2.2.3 Quantum Electrodynamic Corrections

The Lamb shift was experimentally discovered when an energy difference of ≈ 1 GHz between the states $2S_{1/2}$ and $2P_{1/2}$ of hydrogen was observed even though it was not originally predicted by the Dirac energy [46, 55]. Efforts to explain this discrepancy led to the development of QED theory. For circular Rydberg states, a first-order account of QED corrections is sufficient; the result is

$$E_{\text{Lamb}} = \frac{8Z^4\alpha^3}{3\pi n^3} hcR_\infty \sum_l |C_{lm_l}^{n_1 n_2}|^2 \left[L(n,l) + \frac{3}{8}\frac{c_{lj}}{2l+1} \right], \tag{2.23}$$

where

$$c_{lj} = \begin{cases} (l+1)^{-1} \text{ for } j = l + 1/2 \\ -l^{-1} \text{ for } j = l - 1/2 \end{cases}, \tag{2.24}$$

and the Bethe logarithm, $L(n,l)$ [56], can be extrapolated for $n \geq 4, l \geq 3$ as

$$L(n,l) = \frac{0.1623834}{2l+1} \left[\left(\frac{1}{l}\right)^{3/2} - \left(\frac{1}{n}\right)^{3/2} \right] \left[1 \pm \left(\frac{1}{2} - \frac{1}{4}\left(\frac{l+1}{n}\right)^{3/2} \right) \right]. \tag{2.25}$$

The first term in Eq. 2.23 is the vacuum polarization term and the second is the self energy term. The vacuum polarization term comes about from the quick formation and annihilation of electron and positron pairs. During their brief existence, these charges make the vacuum polarizable and hence cause changes in the net fields experienced by the electron. The self energy term accounts for the electron quickly absorbing and emitting a virtual photon from the vacuum field. This leads to an increase in the electron's effective mass and gives rise to the anomalous magnetic moment of the electron [46], which it is expressed by the electron's g-factor being $2 + \alpha/\pi$ (to lowest order) and not just 2. This change in the electron's magnetic moment can be introduced into energy level calculations by using the second term in squared brackets in Eq. 2.23 or using the corrected g-factor in Eqs. 2.15 and 2.16, in

this thesis, I follow the former.

In Eq. 2.23, the self-energy term is typically two orders of magnitude higher than the vacuum polarization term, with the values for the circular state of interest being 0.59 Hz and 1.1 mHz, respectively, and values for the near-circular state being 0.31 Hz and 0.89 mHz. These corrections are small and lead to a small transition energy shift due to the Lamb shift as shown in Table 5.1.

2.2.4   Hyperfine Structure Correction

Significantly smaller than the splitting caused by the spin-orbit coupling, the hyperfine structure arises due to the interaction of the nuclear spin with the orbiting valence electron.

First, I consider the interactions between the nuclear spin and the orbiting-electron magnetic field. I follow a similar procedure to that presented for the spin-orbit coupling term of the fine-structure Hamiltonian. I consider the potential $-\boldsymbol{\mu}_{\mathrm{N}} \cdot \mathbf{B}$ where the nuclear magnetic moment $\boldsymbol{\mu}_{\mathrm{N}} = (e/2m_{\mathrm{N}})g_{\mathrm{N}}\mathbf{I}$ with m_{N} being the nuclear mass, g_{N} the nuclear g-factor and $\mathbf{I}$ the nuclear spin. Using this and the expression for the magnetic field in terms of the angular momentum, $\mathbf{L}$, that I obtained before for the spin-orbit coupling yields

$$\hat{H}_1 = -\frac{e^2 \mu_0 g_{\mathrm{N}}}{8\pi m_e m_{\mathrm{N}}} \frac{1}{\hat{r}^3} \left(\hat{\mathbf{I}} \cdot \hat{\mathbf{L}} \right). \tag{2.26}$$

The magnetic moment of the valence electron caused by its spin also creates a magnetic field with which the nuclear spin interacts. I can calculate this magnetic field by using (Eq. 5.64 in [57])

$$\mathbf{B}_\mu(\mathbf{r}) = \frac{\mu_0}{4\pi} \left[\frac{3\hat{\mathbf{r}}(\hat{\mathbf{r}} \cdot \boldsymbol{\mu}) - \boldsymbol{\mu}}{r^3} + \frac{8\pi}{3} \boldsymbol{\mu}\delta(\mathbf{r}) \right], \tag{2.27}$$

where $\hat{\mathbf{r}}$ is the unit vector in the r direction and $\boldsymbol{\mu}$ is the magnetic moment. Using

this in the magnetic potential $-\boldsymbol{\mu}_{\mathrm{N}} \cdot \mathbf{B}_\mu$ I obtain the second part of the hyperfine Hamiltonian

$$\hat{H}_2 = -\frac{\mu_0 e^2 g_{\mathrm{N}} g_e}{16\pi m_{\mathrm{N}} m_e} \left[\frac{3(\hat{r} \cdot \hat{\mathbf{I}})(\hat{r} \cdot \hat{\mathbf{S}}) - (\hat{\mathbf{S}} \cdot \hat{\mathbf{I}})}{\hat{r}^3} + \frac{8\pi}{3}(\hat{\mathbf{S}} \cdot \hat{\mathbf{I}})\frac{\delta(\mathbf{r})}{\hat{r}^2} \right], \qquad (2.28)$$

where the last term is a contact term which will only be non-zero for s-states. Putting Eqs. 2.26 and 2.28 together results in the full hyperfine-structure Hamiltonian for the dipolar magnetic moment of the nucleus [58]

$$\hat{H}_{\mathrm{HFS}}^d = \frac{\mu_0 g_{\mathrm{N}} e^2}{4\pi m_e m_{\mathrm{N}}} \left(\frac{\hat{\mathbf{L}} \cdot \hat{\mathbf{I}}}{2r^3} - \frac{g_e}{4r^3}\hat{\mathbf{S}} \cdot \hat{\mathbf{I}} + \frac{g_e}{4r^3}3(\hat{\mathbf{S}} \cdot \hat{\mathbf{r}})(\hat{\mathbf{I}} \cdot \hat{\mathbf{r}}) + \frac{2\pi g_e}{3}\frac{\delta(r)}{r^2}\hat{\mathbf{S}} \cdot \hat{\mathbf{I}} \right), \quad (2.29)$$

which acts on the space $\{|n, n_1, n_2, m_l, m_s, m_i\rangle\}$, where m_i is the nuclear magnetic quantum number.

The expression for the energy shift is reached by using first-order perturbation theory and the analytic expression given in [46] for the r^{-3} matrix elements in the Paschen-Back regime. The hyperfine (magnetic dipole) energy shift is

$$\begin{aligned}
E_{\mathrm{HFS}}^d = m_i \sum_l &\frac{|C_{lm_l}^{n_1 n_2}|^2}{a_0^3 n^3(l+1)(l+\frac{1}{2})l}\frac{\mu_0 g_{\mathrm{N}} \hbar^2 e^2}{8\pi m_e m_{\mathrm{N}}}\left(m_l - \frac{g_e m_s}{2} \right. \\
&\times \left. \left[1 - 3\frac{2l^2 + 2l - 2m_l^2 - 1}{(2l+3)(2l-1)} \right] \right),
\end{aligned} \qquad (2.30)$$

which leads to a negligible energy shift (see Table 5.1). Note that Eq. 2.30 does not include the contact term since $l > 0$ for the case of interest.

For $I \geq 1$ and $l \geq 1$, the next term to consider is that which involves the quadrupole electric moment of the nucleus. That term can be calculated using [58]

$$\hat{H}_{\mathrm{HFS}}^q = -\frac{\sqrt{6}}{10\epsilon_0}\frac{Qe^2}{\hbar^2 I(2I-1)}\frac{Y_i^{(2)}}{\hat{r}^3}(\hat{\mathbf{I}} \cdot \hat{\mathbf{I}})^{(2)}, \qquad (2.31)$$

where Q is the nuclear quadrupole moment and $Y_i^{(2)}$ is the normalized spherical
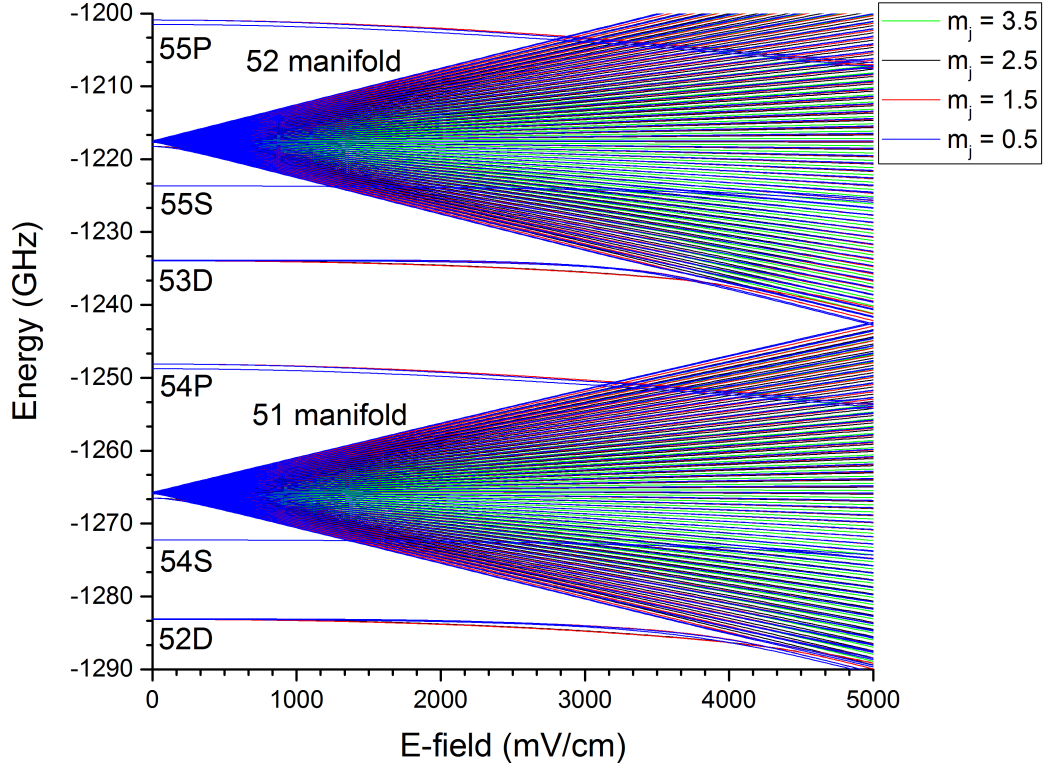
Figure 2.2: Calculated Stark-shifted atomic energies for rubidium as a function of electric field. Energies are with respect to the ionization threshold. States S, P and D are non-degenerate with the hydrogenic manifolds (high-l states) because of their large quantum defects.

harmonic of rank 2 and component i. As I and l increase in value, more orders of the nuclear moment can be considered. For rubidium-85 $I = 5/2$, which means I could consider up to the magnetic quadrupole moment. In the shift in Table 5.1, however, I only consider up to the nuclear magnetic dipole moment since this term alone is already very small and does not contribute a significant uncertainty.

Similar to the fine-structure, a relativistic derivation for the hyperfine structure can be done leading to two extra terms in the electric quadrupole nuclear moment portion [58]. Since the dipolar term discussed here is already small for our purposes, the extra terms resulting from the relativistic treatment are not taken into account.

2.2.5 Stark Shift

In hydrogen, the presence of an electric field lifts l-degeneracies. In rubidium, the quantum defects for low-l states lift these degeneracies even at zero electric fields. However, the high-l states, which follow a similar behavior to the hydrogen states and hence we often refer to them as the hydrogenic manifold, remain degenerate at zero electric field. Figure 2.2 shows calculated Stark-shifted energy levels as a function of electric field. As shown in the figure, the hydrogenic manifold exhibits a more drastic energy shift due to the electric field than the low-l states. Also, the shift experienced by the hydrogenic manifold is mostly linear while the shift of the low-l states is quadratic.

2.2.5.1 First-order Stark shift

To obtain the energy shift due to the Stark effect of high-l states I use degenerate perturbation theory. The Stark perturbation, $\hat{H}_{\mathrm{S}} = Fe\hat{z}$ with the electric field, $\mathbf{F}$, pointing along z, is in the off-diagonals of the Hamiltonian matrix (in spherical coordinates) while the unperturbed energy levels are in the diagonals. However, in the parabolic basis, $|n, n_1, n_2, m_{\mathrm{l}}\rangle$, with quantization axis along z, the Stark Hamiltonian is diagonal in the basis and hence no diagonalization of the Hamiltonian matrix is necessary. The first-order eigenvalues of the Stark Hamiltonian for high-l states in the parabolic basis are

$$E_{\mathrm{S}} = \frac{3}{2}Fea_0n(n_1 - n_2). \tag{2.32}$$

where a_0 is the Bohr radius. Notice that the different $n_1 - n_2$ states in the hydrogenic manifold fan out with a separation of $3Fea_0n/2$ which is referred to as the Stark frequency.

The states and transitions in the proposed Rydberg constant measurement are of the type $|n, 0, 0, n - 1\rangle \leftrightarrow |n + 2, 1, 1, n - 1\rangle$; in which cases the linear Stark shifts for

both levels, as well as for the transition, are identical zero. Due to the high sensitivity of Rydberg atoms to electric fields (see Table 1.1), being able to obtain a zero first-order Stark shift by simply selecting the appropriate states is critical to the success of the Rydberg constant precision measurement discussed here.

Since the low-l states are non-degenerate due to their different quantum defects (see Fig. 2.2), for these I must use non-degenerate perturbation theory which results in zero first-order Stark shift because $\langle nlm_l|\hat{z}|nlm_l\rangle = 0$.

2.2.5.2   Second-order Stark shift

For high-l states, the degeneracies are lifted by the first-order Stark shift and second-order non-degenerate perturbation theory can be used to obtain the quadratic Stark shift (see [25]). For parabolic coordinates, the Stark effect Hamiltonian yields an energy shift of [24, 35]

$$E_{\mathrm{SS}} = \frac{-4\pi\epsilon_0 a_0^3 F^2 n^4}{16} \left[17n^2 - 3(n_1 - n_2)^2 - 9m_l^2 + 19\right], \tag{2.33}$$

which is small for a stabilization electric field of the order of 3 mV/cm (see Table 5.1).

For low-l states, non-degenerate perturbation theory yields an energy shift of

$$\Delta_{n,l,m} = \frac{1}{2}\alpha_{n,l,m}F^2, \tag{2.34}$$

where $\alpha_{n,l,m}$ is the polarizability of the Rydberg state $|n, l, m\rangle$.

2.2.6   Zeeman Shift

For the stabilization of circular states, besides a dominant electric field, a weak magnetic field, B, in the z-direction that removes the remaining m_l degeneracies also needs to be applied. Similar to the fine and hyperfine structures, this external magnetic field interacts with the angular momentum and spin of the electron causing

an energy shift.

2.2.6.1 First-order Zeeman shift

The interaction Hamiltonian is once again $-\boldsymbol{\mu} \cdot \mathbf{B}$ where $\mathbf{B}$ this time is an external magnetic field and $\boldsymbol{\mu}$ depends on the regime we are working on. In a weak-field regime, where the fine structure is larger than the Zeeman shift, we consider the precession of the total angular momentum vector, $\mathbf{J} = \mathbf{L} + \mathbf{S}$, about $\mathbf{B}$. In the strong field (Paschen-Back) regime, which is our case, we must consider the precession of $\mathbf{L}$ and $\mathbf{S}$ separately since the magnetic field breaks their fine structure coupling. As a result, there are two moments that need to be considered and we have $-(\boldsymbol{\mu}_L + \boldsymbol{\mu}_e) \cdot \mathbf{B}$, where $\boldsymbol{\mu}_L = eg_L\mathbf{L}/(2m_e)$ where g_L is the electron's orbital g-factor ($g_L = 1$) and $\boldsymbol{\mu}_e = eg_e\mathbf{S}/(2m_e)$ where g_e is the electron's g-factor. This results in a Zeeman Hamiltonian

$$\hat{H}_Z = \frac{Be}{2m_e}(g_L \hat{L}_z + g_e \hat{S}_z), \tag{2.35}$$

where $\hat{L}_z$ and $\hat{S}_z$ are the orbital angular momentum and spin angular momentum operators along the z-direction, respectively. In the Paschen-Back regime, the parabolic states with spin, $|n, n_1, n_2, m_l, m_s\rangle$, are eigenstates of the Zeeman Hamiltonian. This shift is given by

$$E_Z = \frac{B\hbar e}{2m_e}(m_l + g_e m_s). \tag{2.36}$$

For the transition being considered for the Rydberg constant measurement, m_l and m_s are equal for both states involved and therefore the linear Zeeman shift of the transition is zero. This is of great importance for the proposed precision measurement and hence why this transition is chosen.

2.2.6.2 Diamagnetic shift

The Zeeman Hamiltonian from the previous section can be obtained from the dipole term in the minimal coupling Hamiltonian

$$\hat{H} = \frac{1}{2m_e}(2|e|\mathbf{A}(\hat{\mathbf{r}}) \cdot \hat{\mathbf{p}} + e^2\mathbf{A}(\hat{\mathbf{r}}) \cdot \mathbf{A}(\hat{\mathbf{r}})), \tag{2.37}$$

where $\mathbf{A}$ is the vector potential and it is related to the magnetic field by $\mathbf{A} = (1/2)\mathbf{B}\times \mathbf{r}$. In order to obtain the expression for the diamagnetic term, we must consider the second term instead. After some algebra and assuming the external magnetic field only has a z component we arrive at the diamagnetic Hamiltonian

$$\hat{H}_{\mathrm{D}} = \frac{e^2B^2}{8m_e}(\hat{x}^2 + \hat{y}^2), \tag{2.38}$$

where $\hat{x}$ and $\hat{y}$ are the x and y-direction position operators. This Hamiltonian can be rewritten in the spherical basis as

$$\hat{H}_{\mathrm{D}} = \frac{e^2B^2}{8m_e}(\hat{r}^2 \sin^2\hat{\theta}), \tag{2.39}$$

where the operator $\hat{\theta}$ is the angle with respect to the z-axis. Using Eq. 2.39, we obtain a diamagnetic energy shift of

$$E_{\mathrm{D}} = \sum_l \frac{e^2B^2}{8m_e}|C_{lm_l}^{n_1n_2}|^2 \left\langle nlm_l|\hat{r}^2 \sin^2\hat{\theta}|nlm_l\right\rangle, \tag{2.40}$$

where the angular matrix elements and the radial matrix elements are given in [46] for high-l states. As shown in Table 5.1, these second-order shifts lead to shifts in the order of Hz.

It is critical that the angle between the electric and magnetic field be close to zero for the shifts due to the magnetic field to be negligible, since any departure from
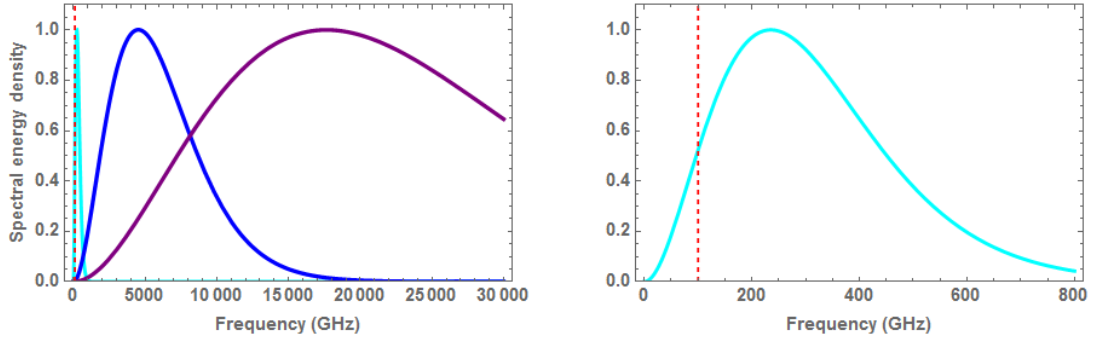
Figure 2.3: Left panel: blackbody spectra for 4 K (cyan), 77 K (blue) and 300 K (purple). All of the curves are normalized against their respective maxima in order to make them all clearly visible. The peak amplitudes of the 77 K and 4 K spectra are 24% and 1.3%, respectively, of the 300 K peak. The dashed red line shows the frequency of the transition of interest. Right panel: zoom in of the blackbody spectrum for 4 K.

zero would introduce x- or y-components of the fields, leading to the appearance of additional second-order shifts. These can be estimated using [35]

$$E_{Z\perp} = -\frac{m_l}{2} \frac{\mu_B^3 B_\parallel B_\perp^2}{(\frac{3}{2}ea_0nF)^2},\tag{2.41}$$

where $B_\parallel$ is the component of the magnetic field parallel to the stabilization electric field and $B_\perp$ is the component perpendicular to it. This expression yields an upper limit for the allowed angular misalignment between the fields of about one degree.

2.2.7 Blackbody Effects

Blackbody radiation is constantly being emitted by objects with temperatures higher than zero Kelvin. The frequency spectrum of such radiation is temperature dependent, with the spectrum for room temperature expanding over a range of about 50 THz, centered at about 18 THz. Lower temperatures yield spectral widths, peak amplitudes and locations that decrease with temperature (see Fig. 2.3).

Blackbody radiation has two effects on Rydberg atoms: the on-resonant portion

affects their lifetime and the off-resonant portion can cause an energy shift [59].

2.2.7.1   Blackbody Lifetime Reduction

Since Rydberg-Rydberg transition frequencies are in the same range as those of thermal blackbody radiation (see Fig. 2.3), thermal transitions lead to a lifetime reduction. Taking this into account leads to a total lifetime of $1/\tau_{\text{total}} = 1/\tau + 1/\tau_{\text{BBR}}$, where $1/\tau$ is the inverse of Eq. 1.3 and τ_{BBR} is the lifetime correction due to the Blackbody-induced transitions [24]. To calculate τ_{BBR}, the transition rate caused by the blackbody radiation, Γ_{BBR}, must be considered. Assuming this perturbation is small, we can use Fermi's golden rule [25]

$$\Gamma_{\text{BBR}}(\omega_b) = \frac{2\pi}{\hbar^2} |\langle f|V_{\text{b}}|i\rangle|^2 \delta(\omega_{\text{b}} - \omega_{fi}),\tag{2.42}$$

where ω_{b} is the blackbody angular frequency, ω_{fi} is the angular transition frequency between the final state, f, and the initial state, i, and $V_{\text{b}} = e\mathbf{r}\cdot\mathbf{F}_{\text{b}}$ is the perturbation due to the blackbody radiation. Integrating over ω_{b} and summing over all final states yields [59]

$$\Gamma_{\text{BBR}} = \sum_f \frac{2\pi e^2}{\hbar^2} |\mathbf{F}_{\text{b}}(\omega_{fi})|^2 |\langle f|r|i\rangle|^2,\tag{2.43}$$

where I only consider bound states, $\langle f|r|i\rangle$ is the radial matrix element and $|\mathbf{F}_{\text{b}}|^2$ is the blackbody field-amplitude squared per angular frequency unit which can be obtained using the spectral energy density form of the Planck radiation law

$$|\mathbf{F}_{\text{b}}|^2 = \frac{\hbar\omega_{\text{b}}^3}{4\pi^3\epsilon_0 c^3(e^{\hbar\omega_{\text{b}}/k_{\text{B}}T} - 1)},\tag{2.44}$$

where k_{B} is Boltzmann's constant and T is the temperature. Notice I have assumed, following [59], that the blackbody field is isotropic.

The radial matrix element in Eq. 2.43 will be large for near-by states only. For
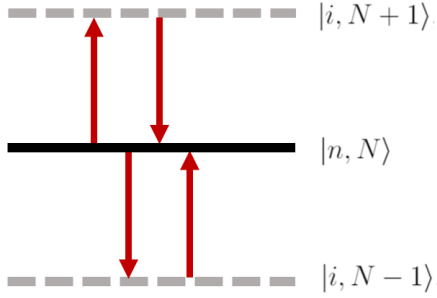
Figure 2.4: Schematic of interaction of the off-resonant portion of the blackbody radiation with atomic energy levels. The state $|n\rangle$ is the atomic state of interest while the state $|i\rangle$ is a perturbing state, N is the number of photons in the blackbody field.

ground state atoms, with transitions usually around the visible spectrum (430-770 THz), the $|\mathbf{F}_b|^2$ is essentially zero even at room temperature (see Fig. 2.3). For Rydberg atoms, however, these nearby transitions (typically 1-1000 GHz) tend to have non-zero values of $|\mathbf{F}_b|^2$ (see Fig. 2.3), with smaller values for smaller temperatures. Therefore, the lifetime of Rydberg atoms are affected by blackbody radiation while ground-state atoms are not. Also, this effect can be lowered by decreasing the temperature of the environment. The lifetime of the $n = 50$ circular state, for example, is reduced from $\tau_{\text{total}} = 30$ ms at 0 K to $\tau_{\text{total}} = 10$ ms at 4 K. For the Rydberg constant measurement, both states in the transition of interest are affected by this lifetime reduction thus, a linewidth in the range of $2 \times \frac{1}{2\pi\tau_{\text{total}}} = 30$ Hz is expected, which is sufficiently narrow for our goals.

2.2.7.2 Blackbody shift

The blackbody shift caused by the off-resonant portion is potentially of greater concern. To calculate this shift we follow the procedure presented in [59]. We use $V_b = e\mathbf{r} \cdot \mathbf{F}_b$ and the expression for an AC Stark shift [25]

$$\Delta_n = V_{nn} + \sum_{m \neq n} \frac{|V_{nm}|^2}{E_n^{(0)} - E_m^{(0)}}, \tag{2.45}$$

where $V_{nn} = \langle n|V|n \rangle$ is zero for our potential due to symmetry and $E_n^{(0)}$ and $E_m^{(0)}$ are the unperturbed energies for states n and m. These states and their energies are defined as (see Fig. 2.4)

$$|i, N - 1\rangle, E'_m = E_m + \hbar\omega_b(N - 1),$$

$$|n, N\rangle, E_n = E_n + \hbar\omega_b N,$$

$$|i, N + 1\rangle, E''_m = E_m + \hbar\omega_b(N + 1),$$

where the first part of the kets, $|i\rangle$ or $|n\rangle$, describes the atomic state and the second part of the kets describes the number of photons in the blackbody field, N. Similarly, the energies have two parts: atomic and field. Note that both of the two-photon transitions shown in Fig. 2.4 start and end in the same state. Using Eq. 2.45 and the energies above we obtain

$$\Delta_n = \sum_m \frac{1}{4} \int_0^\infty | \langle n|e\mathbf{F}_b \cdot \mathbf{r}|i \rangle |^2 \left[\frac{1}{E_n - E'_m} + \frac{1}{E_n - E''_m} \right] d\omega_b. \qquad (2.46)$$

Notice that $E_n - E'_m = \hbar(\omega_{fi} + \omega_b)$ and $E_n - E''_m = \hbar(\omega_{fi} - \omega_b)$, where $\hbar\omega_{fi} = E_n - E_m$. Typically, whenever resonant fields are considered, one of the two terms in Eq. 2.46 is negligible and therefore not carried out in the calculations. This approximation is referred to as the rotating-wave approximation. In our case, both terms are significant and hence we continue with Eq. 2.46 as it is. Finally, after some algebra and integrating over all blackbody frequencies we obtain the blackbody shift expression

$$E_{\text{BBR}}^i = \frac{e^2}{2\hbar} \sum_f \omega_{fi} | \langle f|r|i \rangle |^2 \int_0^\infty \frac{|\mathbf{F}_b|^2}{(\omega_{fi}^2 - \omega_b^2)} d\omega_b. \qquad (2.47)$$

Eq. 2.47 has an implicit dependency on the states being considered since ω_{fi} is defined by the transition in question and the radial matrix elements depend on the states involved. In Eq. 2.47, the integral has a pole for which the principal value

Table 2.3:
Calculated blackbody radiation shift in Hz for the states of interest for room temperature (300 K), liquid nitrogen temperature (77 K), liquid helium temperature (4 K) and outer-space temperature (1.2 K). Since nearby states experience very similar shifts, the transition shift is negligible even at room temperature.

n, l, m_l	300 K	77 K	4 K	1.2 K
51, 50, 50	2416.661	159.2007	0.4248	0.0288
53, 50, 50	2416.620	159.1981	0.4250	0.0299
53, 52, 50	2416.659	159.2013	0.4260	0.0312

integral must be done symmetrically. Also, Eq. 2.47 shows that the direction of your shift will depend on ω_{fi} where lower states cause a shift upward in energy and higher states cause a shift downward in energy.

Approximations for the limiting cases of Eq. 2.47 are given in [24]. In our case, the transition frequency of interest is about 100 GHz, which is on the order of the peak of the radiation spectrum at 4 K (see Fig. 2.3). As a result, in order to calculate the blackbody shift, Eq. 2.47 has to be explicitly evaluated. For extending the results to parabolic states, Eq. 2.5 can be used. For single states, the blackbody shifts amount to a couple of kHz but the *transition* shift is negligible (see Table 2.3). Therefore, using cryogenic temperatures of 4 K is necessary purely to prevent linewidth broadening.

2.2.8 Ponderomotive Optical Lattice

In order to take advantage of the long lifetimes of circular states, it is necessary to trap the Rydberg atoms. To achieve this, it is proposed to use a three-dimensional standing-wave optical lattice, where the atoms are trapped via the ponderomotive potential [60]. This ponderomotive potential emerges from the last term in the minimal-coupling Hamiltonian (Eq. 2.37) which is proportional to laser intensity and arises when a quasi-free Rydberg electron is placed in a rapidly oscillating field.

The wavelength of the lattice is chosen to match a "magic" condition for the desired transition. A "magic"-wavelength lattice is achieved when the states of interest
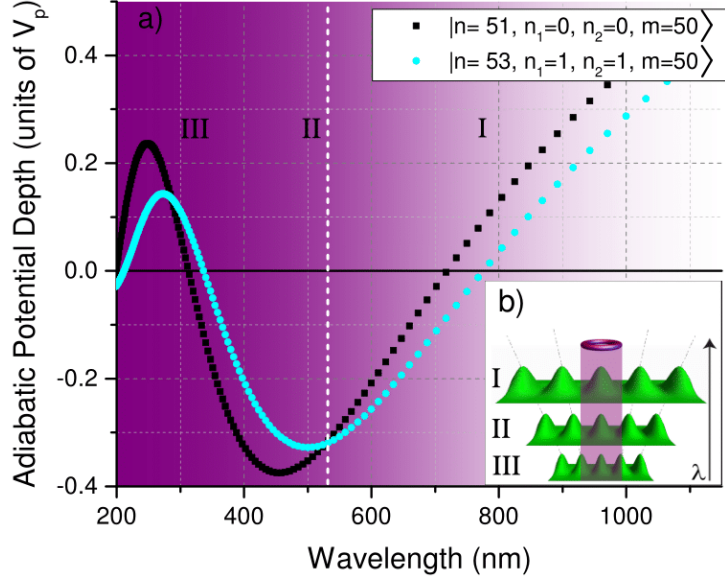
Figure 2.5: a) Ponderomotive adiabatic potential depth (in units of the free electron potential, V_p, the energy of a free electron in the lattice laser field) as a function of wavelength for the two states of interest in a one-dimensional lattice formed by counter-propagating beams ($\alpha = 0$). The points at which the two plots cross are the "magic" wavelengths for this particular pair of states. The magic wavelength we choose for this experiment is shown with a white dashed line, and it occurs at about 532 nm. b) Schematics of the projection of the wavefunction density onto the lattice, as the wavelength is varied and the atom size remains fixed. Labels I, II and III correspond to those in part a). The oscillatory behavior and flip in signs in a) are related to how many lattice periods fall within the volume of the atom [1].

are subject to equal lattice-induced potentials. To illustrate this, in Fig. 2.5a we show adiabatic lattice-potential depths obtained from Eq. 2.49 for the two states of interest, n=51 and n=53, as a function of wavelength. In the figure it is seen that for the two states considered there are two options to achieve magic conditions, 290 nm and 532 nm. For the proposed experiment we choose a 532-nm lattice since it is the second-harmonic of a Nd:YAG laser. Despite this, experimental imperfections can lead to non-zero lattice-induced shifts which we must account for.

2.2.8.1 Lattice-Induced Shift

In its interaction with the optical-lattice field, the Rydberg electron behaves as a quasi-free particle. For a plane-wave linearly-polarized field of the form $\hat{\mathbf{x}}F_L(\mathbf{r})\sin(\omega t)$ ($\hat{\mathbf{x}}$ is a unit vector), Eq. 2.37 leads to the free-electron ponderomotive potential

$$V_{\mathrm{p}}(\mathbf{r}) = \frac{e^2|\mathbf{F}_L(\mathbf{r})|^2}{4m_{\mathrm{e}}\omega_L^2},\tag{2.48}$$

where ω_L is the angular frequency of the laser electric field and $|\mathbf{F}_L(\mathbf{r})|^2$ is proportional to the spatially-varying field intensity, $I(r)$, through $|\mathbf{F}_L(\mathbf{r})|^2 = 2I(r)/n_i c\epsilon_0$, where n_i is the index of refraction of the medium (in our case, $n_i = 1$) [61]. The ponderomotive potential is the average kinetic energy of the free electron in the lattice laser field. This potential is also polarization- and phase-independent as can be seen from to the dot-product in Eq. 2.37 and the complex modulus in Eq. 2.48, respectively.

In our case, the ponderomotive potential also has a dependence on the center-of-mass position, $\mathbf{R}$, since the electron is not entirely free. The potential $V_{\mathrm{p}}(\hat{\mathbf{r}} + \mathbf{R})$ is added as a perturbation to the Rydberg electron's Hamiltonian. Diagonalization of the Rydberg Hamiltonian yields the Born-Oppenheimer (BO) adiabatic potential surfaces,

$$V_{\mathrm{ad}}(\mathbf{R}) = \frac{e^2}{2m_{\mathrm{e}}}\int|\psi(\mathbf{r})|^2|\mathbf{A}(\mathbf{r}+\mathbf{R})|^2 d^3r,\tag{2.49}$$

for the atom's center-of-mass motion, as well as the associated adiabatic Rydberg-electron wavefunction, $\psi(\mathbf{r};\mathbf{R})$ [60].

Generally, $\psi(\mathbf{r};\mathbf{R})$ is unknown and must be simultaneously solved for along with the BO potentials [62]. In our regime, where the shifts due to the parallel electric and magnetic stabilization fields are much larger than the optical shifts, the adiabatic states are given by the parabolic basis states, $|n, n_1, n_2, m_{\mathrm{l}}, m_{\mathrm{s}}\rangle$. This greatly simplifies the calculation of the BO adiabatic potential because $\psi(\mathbf{r};\mathbf{R})$ is no longer dependent on $\mathbf{R}$. Since in our case, the optical lattice is formed by three sets of lattice beams,
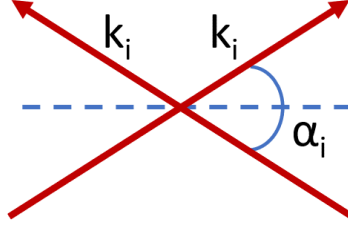
Figure 2.6: Schematics of two lattice beams with an angle α_i between them. This angle α_i can be changed to adjust the periodicity of the resulting standing wave.

the three-dimensional BO adiabatic potential follows from

$$V_{\mathrm{ad}}(\mathbf{R}) = \int |\psi_{n,n_1,n_2}(\mathbf{r})|^2 \sum_i \frac{e^2 |F_{L\mathrm{i}} \cos(\Delta\mathbf{k}_\mathrm{i} \cdot (\mathbf{R}+\mathbf{r}))|^2}{m_\mathrm{e}\omega_{L\mathrm{i}}^2} d^3r. \qquad (2.50)$$

In the integral in Eq. 2.50, $|\psi_{n,n_1,n_2}(\mathbf{r})|^2$ acts as a weighting factor and only needs to be calculated once. There, i is the summing index over optical-lattice directions (for a 3D lattice, $i = 1, 2, 3$), which need not be orthogonal to each other; F_{Li} is the field amplitude of a single beam; $\psi_{n,n_1,n_2}(\mathbf{r})$ is the $\mathbf{R}$-independent Rydberg electron wavefunction; $\mathbf{r}$ is the valence electron (relative) position, ω_{Li} is the angular frequency of the lattice beam (notice we assume we have a monochromatic field); and $|\Delta\mathbf{k}_\mathrm{i}| = |\mathbf{k}_{\mathrm{i}1} - \mathbf{k}_{\mathrm{i}2}| = 2k_\mathrm{i}\cos(\alpha_\mathrm{i}/2)$, where $\mathbf{k}_{\mathrm{i}1}$ and $\mathbf{k}_{\mathrm{i}2}$ are the wavevectors corresponding to the pair of lattice beams along the ith direction, and α_i is the angle between a pair of counter-propagating beams (see Fig. 2.6).

The ratio of laser intensities of the lattice axes (typically up to three) and the aspect ratio between the atom's size (defined by its known state) and the optical lattice periodicities (defined by λ_i and α_i) (Fig. 2.5 and Fig. 2.7) can be experimentally controlled. This allows for variation of the depth and the minimum potential value of $V_{\mathrm{ad}}(\mathbf{R})$ (see Fig. 2.5) and to realize a "magic"-lattice condition (where the two states in the transition experience the same energy shift in the BO potential $V_{\mathrm{ad}}(\mathbf{R})$).

For the purpose of precision measurement, the lattice depth should be kept as
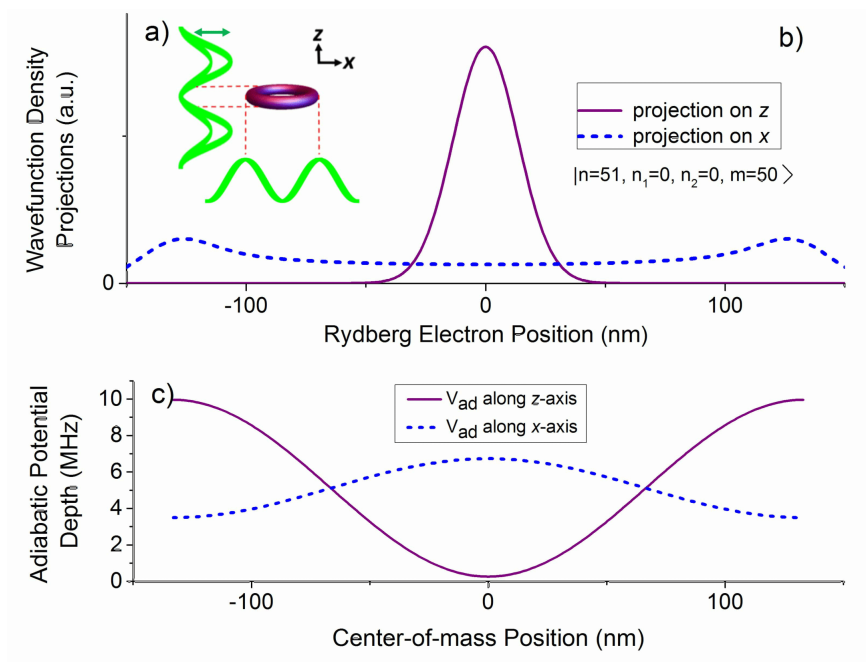
Figure 2.7: Effects of wavefunction projections on the depth of the BO adiabatic potential for a 532-nm lattice extending along x and z, with single-beam intensities 4×10^9 W/m^2 ($\alpha_i = 0$). a) Alignment of the optical-lattice standing-waves and the circular-state probability distribution. The amplitude of the z-direction lattice is modulated in time. b) Projections of $|\psi|^2$ along x and z. The overlap of the projections with the optical-lattice standing waves determines the BO adiabatic trapping potentials along the respective coordinate directions (see Eq. 2.50). c) Trapping potentials (as a function of the center-of-mass position of the atom) calculated from Eq. 2.50; the zero position corresponds to a lattice field node. The different depths and phases are a result of the quite distinct wavefunction projections onto x and z.

small as possible but still large enough to trap atoms at their given temperature. Also, the lattice shift should be smaller than the stabilization fields in order to ensure well defined states for use in Eq. 2.50. Hence, the laser-cooling temperature sets minimum values for the fields that we use in both trapping and stabilization of our states. The hierarchy of shifts is shown in Fig. 2.8 and in Table 2.4 for MOT temperatures ($\sim$ 100μK), temperatures in gray optical molasses ($\sim$ 1μK) [12, 63] and Bose-Einstein condensate (BEC) temperatures ($\sim$ 10 nK). Table 2.5 shows the corresponding typical field magnitudes and provides guidance in designing the circular-state stabilization
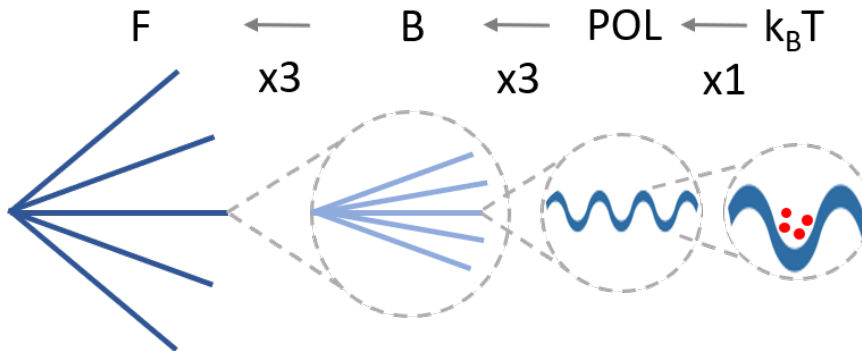
Figure 2.8: Hierarchy of shifts for the proposed Rydberg constant measurement. Notice that the lattice depth needed to trap atoms at a given temperature sets the field magnitudes used in the experiment for trapping and internal-state stabilization. To trap more atoms, the depth of the lattice can be larger than the thermal energy of the atoms, however, this also means larger stabilization fields.

scheme.

2.2.9 Doppler Effect with POL Spectroscopy

The same ponderomotive term that traps atoms is also used to drive transitions between circular and near-circular states [23, 64]. This is possible by modulating the amplitude of the lattice along one direction at a frequency that matches that of the atomic transition we want to drive. To help understand this, let us start with an amplitude-modulated field that moves in the z direction $F(z,t) = F_0(t)e^{-ikz}$ where $F_0(t) = F_0\cos^2(\Omega t/2)e^{-i\omega t}$ is the time-dependent field amplitude, k is the wavevector ($2\pi/\lambda$, λ being the optical wavelength) of the running wave, ω is the optical angu-

Table 2.4: Hierarchy of level shifts in three atomic temperature regimes. All energies are expressed in kHz. Thermal Energy = $k_BT/2$.

T (μK)	Thermal Energy	POL	Magnetic	Electric
100	1000	3100	9400	28000
1	10	31	94	280
0.01	0.1	0.31	0.94	2.8
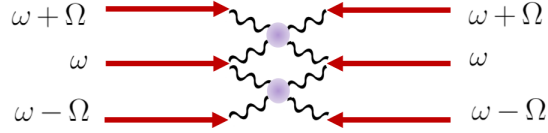
Figure 2.9: Schematics of the frequencies involved in ponderomotive spectroscopy. The atom (purple) scatters from one mode of the lattice to the other (red), with different possible combinations shown. Notice that the net frequency between a photon of frequency ω and a counter-propagating one of frequency $\omega\pm\Omega$ would be Ω (frequency of modulation of the amplitude), which can be tuned to a microwave atomic transition frequency.

lar frequency of the wave and Ω is the microwave angular frequency at which the amplitude of the wave is modulated. The amplitude expression can be rewritten as

$$
\begin{aligned}
F_0(t) &= \frac{F_0}{4}(2 + e^{i\Omega t} + e^{-i\Omega t})e^{-i\omega t} + \text{c.c.} \\
&= \frac{F_0}{4}(2e^{-i\omega t} + e^{-i(\omega-\Omega)t} + e^{-i(\omega+\Omega)t}),
\end{aligned}
\tag{2.51}
$$

which clearly shows that the running wave has three frequencies: ω, $\omega - \Omega$ and $\omega + \Omega$ (see Fig. 2.9). Notice that on the second line and the rest of this section I do not carry out the complex conjugate (c.c.).

To show how transitions are driven, I can use the minimal coupling Hamiltonian (Eq. 2.37) and $\mathbf{F} = -\frac{1}{c}\frac{\partial \mathbf{A}}{\partial t}$. The vector potential is given by

$$
A(z,t) = -cF(z)\frac{F_0}{4}\left[\frac{2i}{\omega}e^{-i\omega t} + \frac{i}{(\omega-\Omega)}e^{-i(\omega-\Omega)t} + \frac{i}{(\omega+\Omega)}e^{-i(\omega+\Omega)t}\right],
\tag{2.52}
$$

Table 2.5: Magnetic and electric fields suitable for three temperature regimes. The fields satisfy $(3/2)nF > B/2 > k_{\mathrm{B}}T \approx$ optical-trap depth, for $n=51$.

T (μK)	Magnetic Field (mT)	Electric Field (mV/cm)
100	0.67	290
1	6.7×10^{-3}	2.9
0.01	6.7×10^{-5}	0.029

where $F(z)$ is the spatially-varying part of the electric field which equals e^{-ikz} for a running wave and $2\cos(kz)$ for a standing wave. Since our analysis is for a lattice, I consider the standing wave case, $A(t)2\cos(kz)$. Therefore, the second term in Eq. 2.37 couples the final state, f, and the initial state, i, by

$$
\begin{aligned}
\langle f|\mathbf{A}^* \cdot \mathbf{A}|i\rangle &= 2|A(t)|^2 \langle f|\cos^2(kz)|i\rangle \\
&= 2|A(t)|^2 \left\langle f \left| \left[1 - (kz)^2 + \frac{(kz)^4}{3} + ... \right] \right| i \right\rangle,
\end{aligned}
\tag{2.53}
$$

where I have expanded $\cos^2(kz)$ for small kz which is valid for typical optical lattices and Rydberg-atom sizes and $\mathbf{A}^*$ is the complex conjugate of the vector potential. The first term in the expansion yields zero coupling while the second and higher terms couple the states. Since this coupling does not arise from the dipole term (included in the first term in Eq. 2.37), we are not restricted by dipole-selection rules and in fact can drive $\Delta l = 0$ transitions as was shown in [23]. A more rigorous derivation of this can be found in [65], where it is shown that transitions with $\Delta l = 0, 1, 2, 3, ...$ can be driven with an amplitude-modulated ponderomotive optical lattice.

For the ponderomotive spectroscopy to be possible, the optical-field intensity must vary substantially within the volume of the atom so that the second and higher-order terms in Eq. 2.53 are large enough to couple the states. Furthermore, the lattice amplitude modulation frequency must be resonant with an atomic transition or a sub-harmonic of it [64]. The first condition makes Rydberg atoms natural candidates for using this spectroscopy method because the size of these atoms is comparable to the spatial variation of lattices made with typical wavelengths in the infra-red. On the other hand, for a ground state atom, the field amplitude would appear constant within the volume of the atom, and therefore there would not be any coupling even if the field were modulated at the transition frequency.

Ponderomotive spectroscopy involves the inelastic scattering of two counter-propagating

optical-lattice photons of angular-frequency difference Ω [66] (see Fig. 2.9), which is at the atomic transition frequency. When considering the Doppler effect in traditional two-photon spectroscopy, the field seen by an atom of velocity $\mathbf{v}$ is proportional to

$$e^{-2i\omega t + i[(\mathbf{k}_1 - \mathbf{k}_2)\cdot\mathbf{v}t] + i(\mathbf{k}_1 - \mathbf{k}_2)\cdot\mathbf{r}_0}, \tag{2.54}$$

where $\mathbf{v}$ is the center-of-mass velocity of an atom, $\mathbf{k}_1$ and $\mathbf{k}_2$ are wave vectors of the beam propagating along a given direction and $\mathbf{r}_0$ is the initial position of the atom. If the time-dependent terms are put together we can immediately see that the atom will see a Doppler shifted frequency of $\Omega' = 2\omega + [(\mathbf{k}_1 - \mathbf{k}_2) \cdot \mathbf{v}]$. In the case of counter-propagating beams with the same wavelength, the wave vectors cancel each other out resulting in no first-order Doppler shift.

When ponderomotive spectroscopy is employed to drive transitions, it is found that Eq. 2.54 approximately accounts for the overall widths of the spectra (indicated by the arrows in Fig. 2.10), because $\mathbf{k}_1$ and $\mathbf{k}_2$ are counter-propagating but differ in magnitude by Ω/c. More importantly, Eq. 2.54 fails to describe the central, narrow peaks observed in ponderomotive spectroscopy which are Doppler-free and Fourier-limited. The transition is driven when two photons from opposite directions are absorbed and their frequency difference equals the atomic frequency (see Eq. 2.52). For an atom with center-of-mass position $z(t)$ in one dimension, we find that the drive term seen by the atom is proportional to [65]

$$\cos(2kz(t))e^{-i\Omega t}, \tag{2.55}$$

where Ω is the frequency at which the lattice amplitude is modulated. Equation 2.55 shows that the effective Rabi frequency seen by the atoms has a phase that does not depend on their velocity. As presented in [65], the phase of the resulting effective Rabi frequency changes by π at every lattice inflation point. This means that atoms
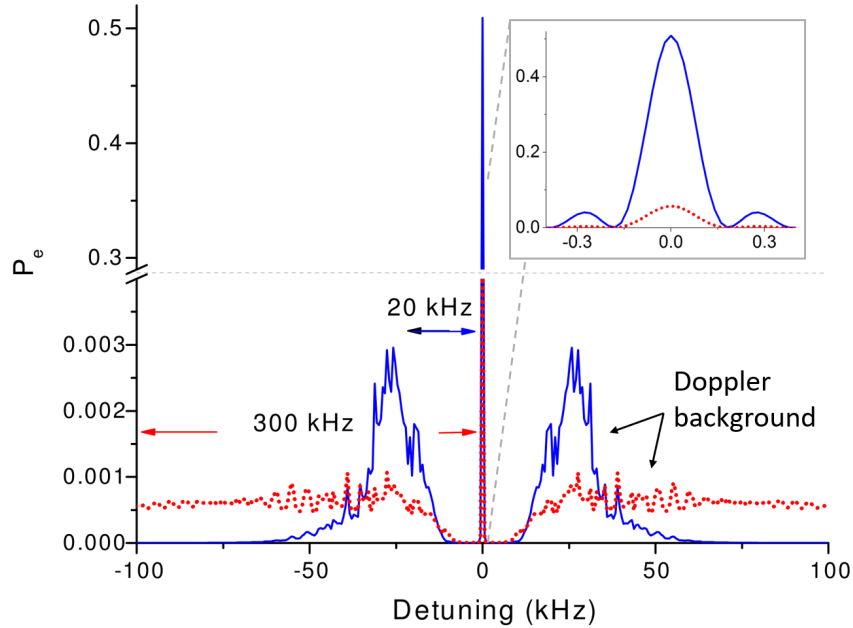
Figure 2.10: Simulation of the excited-state population, P_e, as a function of detuning for two temperature regimes: 100 μK (red dashed line) and 1 μK (blue solid line) for a potential depth of 35 kHz (motivated by Table 2.4) and an interaction time of 5 ms. The inset shows that the widths of the narrow features at the center are Fourier-limited. The arrows indicate the approximate half widths of the Doppler-broadened background signals.

trapped in individual wells experience effective Rabi frequencies with constant phases that do not depend on the details of the center-of-mass motion at all (the atoms just have to be trapped and not leave the lattice potential well). As a result, the Doppler-free peaks originate from atoms that are trapped. On the other hand, the features on the sides (which do follow Eq. 2.54) are due to atoms that are not trapped in a single lattice well and roam over many wells. Those atoms experience effective Rabi frequencies with phase jumps of value π at each lattice inflection point they traverse. This results in the usual Doppler-broadened side features in Fig. 2.10.

In order to model the spectra, we employ a simulation program that treats the center-of-mass dynamics of the atoms (due to lattice-induced forces) classically and the internal, modulation-driven dynamics quantum-mechanically [23, 64, 67]. The

effects of temperature on the population fraction that becomes excited into the upper state are shown in Fig. 2.10 for a potential depth of 35 kHz in a one-dimensional lattice. The central, Fourier-limited features shown correspond to trapped atoms (no Doppler effect). As the temperature is lowered, while the fraction of atoms trapped in the optical-lattice wells increases (leading to a corresponding increase of the area under the central peaks in Fig. 2.10) the linewidth of the central feature remains Fourier-limited. Hence, for a fixed lattice depth temperature changes affect the number of atoms that are trapped but not the width of the central feature of interest. For a substantial number of atoms to be captured at this lattice depth, molasses temperatures (1 μK) are required, as shown in Fig. 2.10. At 100 μK, only about 6% of the population is trapped, whereas 1 μK yields 51% trapped population. When temperatures are lowered, the full width of the Doppler-broadened background signal is $\approx 4v\omega/\pi c$, where the thermal velocity $v = \sqrt{k_{\mathrm{B}}T/M_{\mathrm{atom}}}$ (see Eq. 2.54). The gaps between the central peak and the onset of the Doppler background reflect the fact that atoms within a range of velocities are trapped. The trapped atoms experience no Doppler shift and generate the Fourier-limited feature at the center of the spectrum. They essentially undergo recoil-free absorption within the lattice wells. Having no Doppler effect in the proposed precision measurement is essential, making the ponderomotive spectroscopy an ideal technique.

CHAPTER III

Experimental Setup

A large portion of my graduate work consisted of designing and building the experimental setup that was used in the precision measurements presented in this thesis. The set up was made with the proposed Rydberg constant measurement in mind, which resulted in a lot of attention being given to having very good control of the environment in which the spectroscopy was to be performed. The precision measurements presented in this thesis serve to demonstrate the suitability of this setup for measurements of this nature.

In this chapter, I present the setup specifications and the methods used for cooling, detecting and electric and magnetic-field zeroing. Even though in the experimental results presented in this thesis we do not make use of circular Rydberg atoms, they are a key aspect of the proposed Rydberg constant measurement and significant time was devoted to preparing the system for the circularization of the atoms. Therefore, I also briefly discuss the circularization method for which the spectroscopy enclosure was designed.

3.1 Ultra-High Vacuum System

The heart of the experimental setup consists of a stainless steel vacuum chamber which has 11 horizontal viewing ports, each with different optical coatings (see Fig. 3.1

46
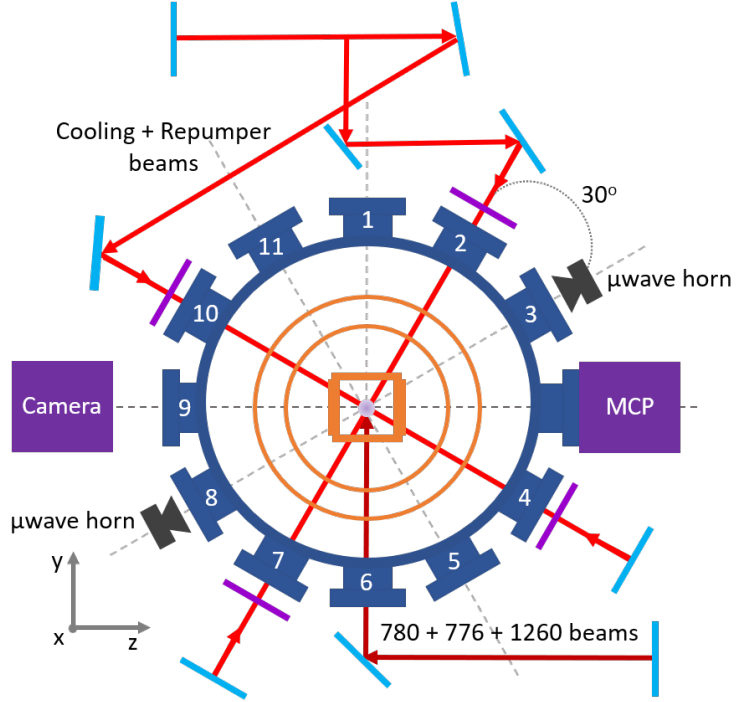
Figure 3.1: Top view schematics of upper chamber where the numbers on each view
port correspond to those used on Table 3.1. Also shown are parts of the
laser beam paths for cooling (cooling + repumper beams) and excitation
(780 + 776 + 1260 nm beams), microwave horns, detection micro-channel
plate and camera used to monitor molasses. The thin blue rectangles are
mirrors, the orange rings inside the chamber are the copper buckets that
are in thermal contact with the cryostat and the orange square shows the
centered spectroscopy enclosure. Drawing is not to scale.

and Table 3.1), several connections that allow for the control of voltages and currents
from outside of vacuum (see Fig. 3.2) and a micro-channel plate (MCP) used for
detection. A cryostat with two inner buckets, one for liquid nitrogen (outer) and one
for liquid helium (inner) is in thermal contact with the main vacuum chamber. The
main purpose of this cryostat is to decrease the blackbody radiation effects discussed
in Chapter II, although it is also useful for lowering the chamber pressure. Pressures
in the system can be between 6.0×10^{-9} Torr (with no liquid nitrogen present) to
2.0×10^{-9} Torr (with liquid nitrogen temperatures). For the experiments presented
in this thesis, only liquid nitrogen was used in the cryostat, liquid helium will be
employed for the Rydberg constant measurement where much narrowed linewidths

Table 3.1:
List of optical anti-reflection (AR) coatings on the vacuum windows of the upper chamber. The numbers correspond to those shown in Fig. 3.1. For the windows, the size column refers to diameters. The AR coatings on the glass cell are inside and outside, reflection $< 0.5\%$ at zero degrees.

Windows	Size (cm)	780 nm	532 nm	1064 nm	Uncoated
1,6	7	X	X		
2,3,4,8,10	7	X			
5,9	7			X	
7,11	7				X
top	3.38	X	X		
Bottom of glass cell	3 by 3	X	X		
Sides of glass cell	7.5 by 3				X

are needed to achieve the desired precision.

Inside the main vacuum chamber there are several layers (see Fig. 3.3). First, two copper buckets, each in thermal contact with the two different buckets of the cryostat, help shield the center of the vacuum chamber from blackbody radiation. Further in, and also in thermal contact with the cryostat, there is the aluminum outer shell of the spectroscopy enclosure (see Fig. 3.13 towards the end of the chapter). This layer further shields from thermal radiation and holds a pair of in-vacuum coils which, depending on the direction of the currents, can produce a MOT magnetic field or a constant-magnitude magnetic field at the center of the enclosure. Inside this spectroscopy enclosure, and held by several delicate macor pieces, there are six sets of copper plates with small viewports to allow optical and microwave signals to reach the center. These copper plates are used to control the electric fields at the location of the atoms. To deliver DC voltage control to these electrodes, we use Manganin wire (MWS wire industries ID 71398) with a voltage rating of 3800 V. Radio-frequency (RF) signals are delivered using twisted pair wires coated in Kapton (Accuglass KAP-28AWG-TWIST-5).

The lower portion of the main vacuum chamber is attached to a glass cell shaped
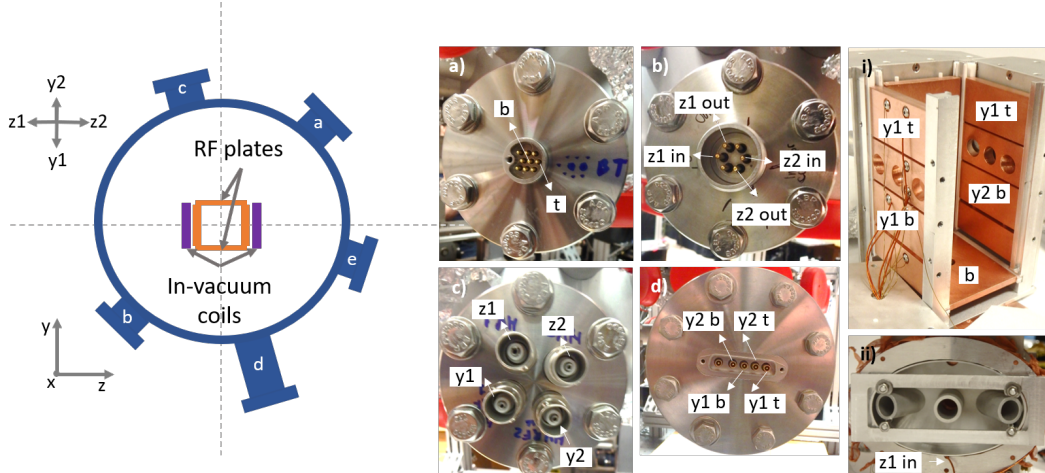
Figure 3.2: The left schematics show a top view of the vacuum chamber showing the lower row of ports (upper row is shown in Fig. 3.1) which contain connections to the in-vacuum electronics. The different directions are labeled as z1, z2, y1 and y2. e) Shows the location of the ion gauge which we use to measure the pressure in the upper chamber. a) Shows the connector that controls voltages on the top (shown as t) and bottom (shown as b) electrodes of the spectroscopy enclosure (see i). These voltages are meant to only be low DC voltages to eliminate stray electric fields along the x direction (the vertical direction). b) Shows the connector that controls the currents of the two in-vacuum coils (see ii, which shows one of the coils mounted on the spectroscopy enclosure). We define clock-wise (counter-clock wise) current as going from z1in (z2in) to z1out (z2out) when looking from z2 (z1). c) Shows the high-voltage connector. Even though the connection is high voltage, we also send low DC voltages through in order to eliminate stray electric fields in the y and z directions. Notice that even though the RF plates are four in total, we apply the same DC voltages to all four simultaneously (connectors y1 and y2), see Fig. 3.13. d) Shows the RF connector which applies the signal that will be used in the circularization of Rydberg atoms.

as a rectangular box, the bottom of which has anti-reflection coatings of 532 and 780 nm. Surrounding this glass cell is a 3D-printed structure that holds a set of four coils that create the MOT magnetic field needed for the first-stage atom cooling.

The main vacuum chamber and the glass cell each have their own ion pump attached to them, as well as a port for turbo pumps to be connected. A gate valve between the two bodies makes it possible to pump each portion of the system separately and facilitates solving any problems specific only to one of the two portions.
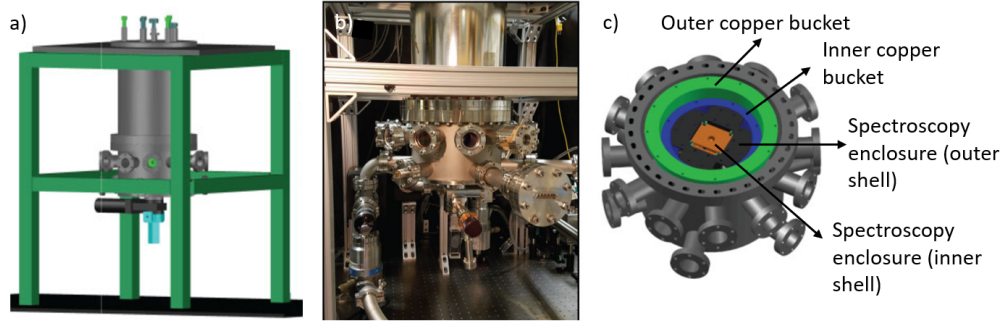
Figure 3.3: Figure from [2]. a) Auto-CAD drawing of system showing the glass cell in light blue, the main vacuum chamber and the cryostat on top. The green structure is an 80-20 which helps hold the entire system and which also holds the compensation coils (not shown). b) A picture of the assembled vacuum system. c) Auto-CAD drawing of the inside of the vacuum chamber showing the different layers.

The rubidium source used in the system is in a separate vacuum flange which is heated during experiments to release rubidium gas into the glass cell. It is connected to the glass cell via a gate-valve which can be controlled to change the amount of rubidium entering the cell. An L-shaped aluminum piece guides the rubidium vapor flow into the center of the cell first where they are cooled, instead of allowing the vapor to directly flow into the vacuum pump.

3.2 Cooling of ^{85}Rb

I use cold atoms to reduce interaction-time broadening and to limit the interaction volume, thereby reducing field inhomogeneity effects. To this end, I use a combination of a magneto-optical trap (MOT) and molasses to cold atoms to approximately tens of μK.

3.2.1 Cooling Lasers

In this work, I use ^{85}Rb D2 line hyperfine structure for atom cooling, with the main cooling transition being $5S_{1/2}, F = 3 \rightarrow 5P_{3/2}, F = 4$ (see Fig. 3.4). An extra

laser beam tuned to the transition $5S_{1/2}, F = 2 \rightarrow 5P_{3/2}, F = 3$ is used to re-pump atoms back to the cooling transition after they exit the cycle via spontaneous decay to state $5S_{1/2}, F = 2$.

The cooling lasers are external-cavity diode lasers (ECDL) where one side of the cavity is formed by the reflective back surface of the diode and the other by a diffraction grating mounted on an optical mount. In this Littrow configuration [68], as the angle of the grating is changed by tweaking the horizontal knob of the optical mount, the output wavelength of the laser changes by

$$\lambda = \frac{2\sin\alpha}{Gm}, \tag{3.1}$$

where G the groove density of the diffraction grating, m is the diffraction order, λ is the selected laser wavelength and α is the angle between the light ray and the normal of the grating. The zeroth diffraction order serves as the output of the laser while the first order is reflected back and acts as optical feedback. The wavelength of the laser can also be changed by tweaking the current supplied to the diode and its temperature.

The laser frequency is stabilized by using saturated absorption spectroscopy [69]. In this method, a portion of the laser sent to the vacuum chamber is separated and split into two. These beams are sent through a vapor cell filled with rubidium and one of them is retro-reflected back such that it is counter-propagating with one of the two incoming beams (see Fig. 3.4). Since the vapor cell contains a thermal sample, the single beam drives transitions that result in Doppler-broadened features one for each of the two ground states of each isotope, resulting in a total of four Doppler curves. The two counter-propagating beams drive transitions that result in Doppler curves with "hole burning" (see Fig. 3.4) or two-photon Doppler free signals as explained in Chapter II. The two signals are collected in photo-diodes and their electric signals
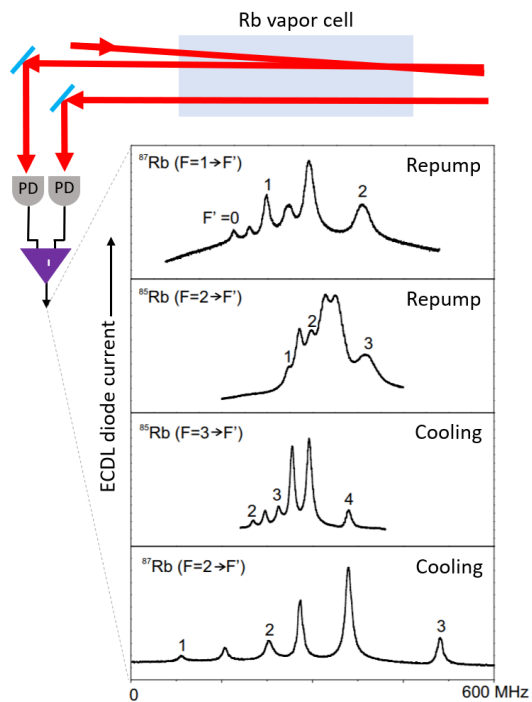
Figure 3.4: Schematics of a sample optical setup for saturation absorption spectroscopy and resulting rubidium hyperfine structure spectra. Spectra from [3].

are amplified and subtracted. The resulting signal (shown in Fig. 3.4 as a function of laser frequency) can be used in a proportional-integral-derivative (PID) feedback circuit to select and maintain a specific laser frequency [70]. The feedback loop is complete by sending correcting voltages to a piezo attached to the grating. This corrects for natural frequency drifts in the laser and small environment disturbances.

Moreover, these home-made ECDLs are temperature stabilized using a different feedback loop where a thermistor monitors the temperature of the diode housing, the reading is sent to a temperature controller and the output of this is sent to a thermo-electric coupler (TECs). This loop protects the laser from overheating and from temperature fluctuations in the environment.

Even though the same cooling laser is used for the glass cell MOT and the upper chamber molasses, their optical setups vary. For the primary MOT two beams are put
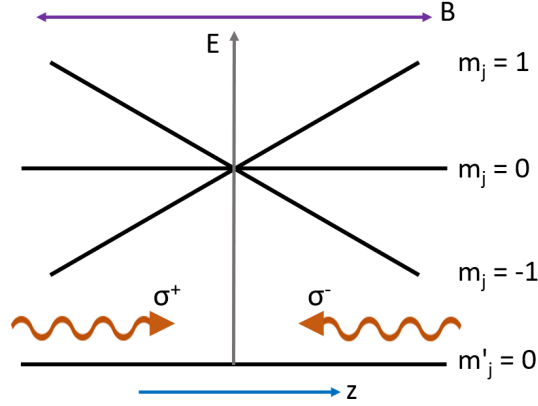
Figure 3.5: a) Example schematics of Zeeman shifted energy levels $J' = 0, m'_j = 0$ (ground state) and $J = 1, m_j = 0, \pm 1$ (excited state) that can be used in a magneto-optical trap to cold atoms.

through anamorphic prisms in order to stretch the beam shape along one direction. This results in two elliptical beams with semi-minor axes of about 2 cm and semi-major axes of about 5 cm. These beams are retro-reflected to confine atoms in 2D. Typical powers are about 70 mW per beam.

For the optical molasses, we detune the frequency of the molasses beam by -2 MHz (relative to the D2 cooling transition) using an acousto-optic modulator (AOM) and split it into three beams which are all retroreflected. The three pairs of beams are about a centimeter in diameter and are circularly polarized with counter-propagating pairs having orthogonal polarizations. Typical powers are about 10 mW along the transverse beams and 20 mW along the vertical beam. More power is sent along the vertical arm because this beam is used to both push atoms from the glass cell to the upper chamber and for cooling in the upper-chamber molasses setup.

3.2.2 Magneto-Optical Trap

The magneto-optical trap (MOT) uses optical beams and magnetic-field gradients to cool down atoms to typical temperatures of hundreds of μK. As an example, Fig. 3.5 shows a schematics of a $J = 0$ to $J = 1$ transition with the different m_j levels Zeeman

shifted linearly with the magnetic field (as expected from Eq. 2.36). In Fig. 3.5, atoms moving away from the center of the trap, where the magnetic field is minimum, become resonant with the optical beam moving in the opposite direction at a given location in the magnetic-field gradient. This results in the atom experiencing a force in the direction of propagation of the optical beam (toward the center of the trap) of the form [10, 71]

$$\mathbf{F}(x_i) = \frac{\hbar k \gamma |\Omega|^2 \hat{\mathbf{x}}_i}{8} \left[\frac{1}{\gamma^2 + (\delta + kv_i + \beta z)^2} - \frac{1}{\gamma^2 + (\delta - kv_i - \beta z)^2} \right], \qquad (3.2)$$

where k is the wave vector of an optical beam, γ is the decay rate of the excited state, Ω is the Rabi frequency, $\delta = \omega_0 - \omega$ is the detuning of the optical light radial frequency (ω) from the atomic transition radial frequency (ω_0), v_i is the velocity of the atom along the direction x_i and $\beta = \frac{g_e e}{2m_e} \frac{\partial B}{\partial z}$, where $\frac{\partial B}{\partial z}$ is the magnetic field gradient created by the MOT coils, in our case.

In order for this scheme to work, it is critical that the two counter-propagating optical beams in each direction have orthogonal circular polarizations, σ^+ and σ^- (see Fig. 3.5). Also, the magnetic field must have a minimum point where the cold atoms collect. A quadrupole magnetic field is produced with field gradients typically of about 20 G/cm (see Fig. 3.6).

To produce the magnetic fields, we use two different MOT-coil configurations. The primary MOT (at the location of the glass cell) uses a $2D^+$ MOT [72, 73] which consists a set of four racetrack-shaped coils that produce a magnetic field gradient with a minimum along the line of symmetry of the coils (see Fig. 3.6). This magnetic field has the form

$$\mathbf{B} = \alpha x \hat{\mathbf{x}} + \beta y \hat{\mathbf{y}} + (\alpha + \beta) z \hat{\mathbf{z}}, \qquad (3.3)$$

where α and β are magnetic field gradients. If we set $\beta = -\alpha$, we obtain the $2D^+$ MOT configuration which results in a string of cold atoms along the line of symmetry.

Table 3.2: Specifications of the sets of coils in the experimental setup. The primary MOT is that obtained in the glass cell (lower part of the experimental setup). Note that the coils in the upper chamber can be used to create a constant, stabilization magnetic field or a MOT gradient field by simply making the current direction the same or opposite, respectively. The parameters a_{in}, a_{out}, b_{in}, b_{out} are illustrated in the figure below, z_{in} and z_{out} are distances from the location of the atoms. All dimensions are in cm.

	Shape	Turns per layer	Layers	a_{in}	a_{out}	b_{in}	b_{out}	z_{in}	z_{out}
Primary MOT	racetrack	9	7	1.0	1.5	2.25	-	1.76	2.76
In-vacuum coils	elliptical	14	9	3.6	4.3	2.2	2.9	3.4	4.8
Compensation coil x-direction	circular	8	2	12.1	12.3	-	-	10.2	11.6
Compensation coil y-direction	rectangular	10	7	12.7	13.5	27.9	-	29.9	31.8
Compensation coil z-direction	rectangular	10	10	12.7	13.9	30.5	-	34.3	36.1
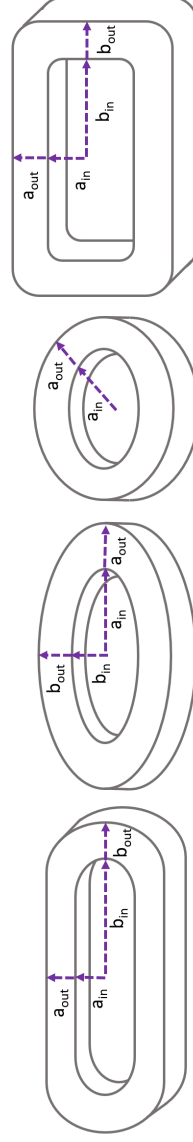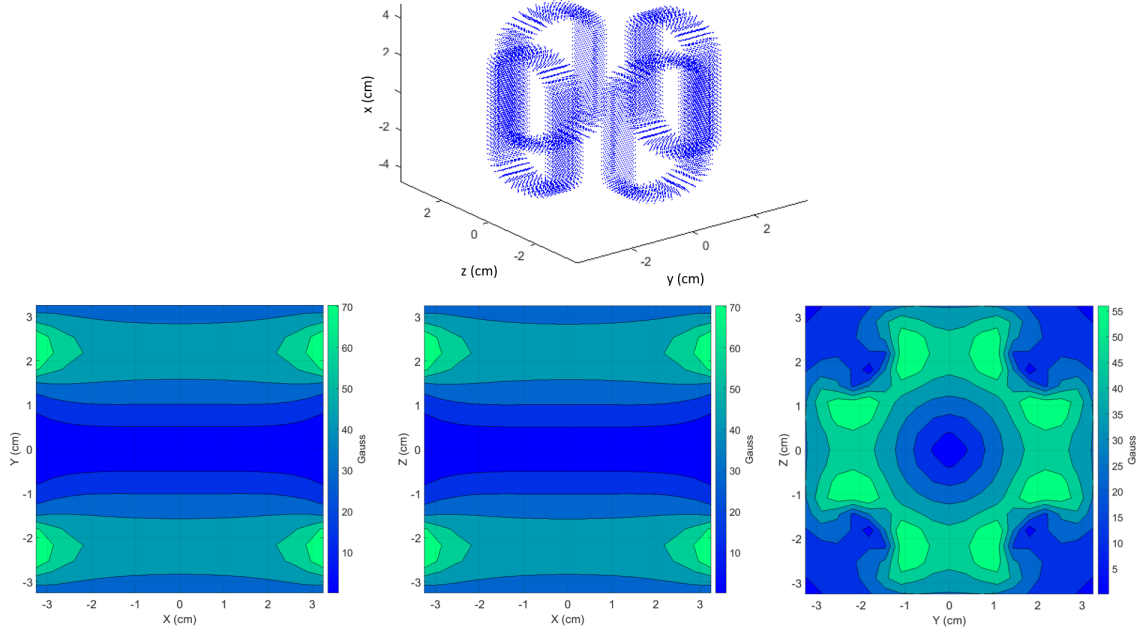
Figure 3.6: Top panel: schematics of the coils used to obtain the 2D$^+$MOT in the experimental setup. The coils rest on a 3D-printed structure which wraps snugly around the glass cell and it is supported from above to avoid causing strain. Bottom panel: calculation results of the total magnetic field, in Gauss, produced by the 2D$^+$MOT coils when the coils are set to 3.0 A. In the calculations, the coils are divided into small, finite pieces and the Biot-Savart's law is used to obtain the magnetic field. We assume the wire occupies 70% of the space allotted for the coil.

Therefore, this configuration yields a larger number of atoms than a regular MOT would and makes it a good source of slow atoms for the upper chamber.

The atoms from the primary MOT are pushed upward to the secondary chamber by a imbalance in the powers of the vertical beam and its retro-reflection used for the cooling in the upper chamber. Even though the upper chamber is designed to produce an optical molasses, the directions of the currents through the in-vacuum coils can be set to produce a MOT magnetic field and hence obtain a MOT. This configuration is more widely used in AMO experiments and produces a spherical MOT since the magnetic potential only has a point where the magnetic field is minimum [10]

$$\mathbf{B} = -\alpha(x\hat{\mathbf{x}} + y\hat{\mathbf{y}}) + 2\alpha z\hat{\mathbf{z}}, \tag{3.4}$$

56

where α is the magnetic-field gradient. Notice that applying offset magnetic fields in any direction would only move around the spatial location of the magnetic-field minimum (B=0).

Even though I have the capability of using a MOT in the upper chamber, for the experiments presented in this thesis it is best to not have a magnetic-field gradient and switching the MOT magnetic field to achieve no gradient would result in unwanted long-lived Eddy currents. Hence, I prefer to use only optical molasses for the cooling of the atoms in the upper chamber.

3.2.3   Optical Molasses

In contrast to a MOT, optical molasses are obtained with no magnetic field present, instead atoms are cooled down due to the Doppler effect and the light polarization gradient caused by counter propagating beams. Initially, it was thought that the cooling in an optical molasses would be only due to the force that an atom of velocity v_i moving along the ith-direction would experience from two counter-propagating beams [71]

$$\mathbf{F}(x_i) = \frac{\hbar k \gamma |\Omega|^2 \hat{\mathbf{x}}_i}{8} \left[\frac{1}{\gamma^2 + (\delta + kv_i)^2} - \frac{1}{\gamma^2 + (\delta - kv_i)^2} \right]. \tag{3.5}$$

However, when optical molasses were first obtained the observed temperatures were below the expected Doppler limit temperature, $T_D = \frac{\hbar \gamma}{2k_B}$ [11, 74]. To understand this, it needed to be taken into account the light polarization gradient caused by the two counter-propagating beams of orthogonal polarizations and its effects on the m_j sub-levels of the atoms. The result is a Sisyphus cooling mechanism [4, 10] where an atom is optically-pumped to $\pm m_{max}$, depending on the polarization at the location in which it is optically pumped. As the atom continues to move (and the polarization and light shift continues to change) the atom "climbs" a potential (losing kinetic
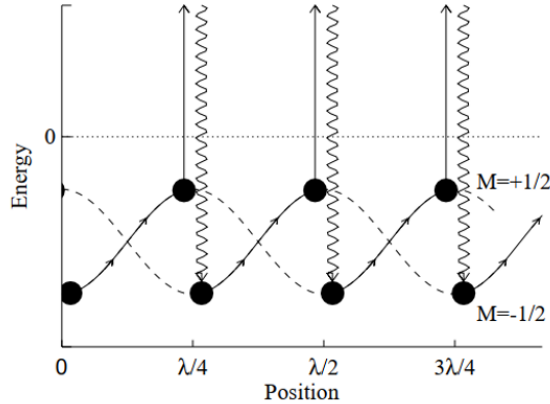
Figure 3.7: Figure from [4]. Schematics of Sisyphus cooling for ground states $m_j = -1/2$ and $m_j = 1/2$ with two orthogonal linearly polarized counter-propagating beams. At $z = \lambda/4$, polarization is purely σ^- resulting in optical pumping to the $m_j = -1/2$ state. Similarly, at $z = \lambda/2$, polarization is purely σ^+ resulting in optical pumping to the $m_j = 1/2$ state.

energy) and it decays into an m_j level with smaller energy shift. As a result, the kinetic energy of the atom first converted to potential energy is finally radiated away from the system when it decays (see Fig. 3.7).

Three different combinations of transitions can yield optical molasses: $J \to J+1$ (bright molasses), and $J \to J$ or $J \to J-1$ (gray molasses, sometimes called blue molasses due to the blue detuning used) [12, 63]. In bright molasses both states are coupled to the optical field and hence there is photon scattering that limits how low the temperature can be. On the other hand, some of the states involved in gray molasses are "dark states", meaning that they are not coupled to the optical field resulting in no light shift and lower photon scattering rates. Therefore, gray molasses can yield temperatures considerably lower than bright molasses.

Compared to MOTs, molasses can achieve temperatures two orders of magnitude lower. Also, molasses yield two to four orders of magnitude lower densities of cold atomic samples than MOTs due to the lack of spatial confinement the magnetic field gradient in a MOT offers. For the precision measurements discussed in this thesis, working with typical molasses densities ($\lesssim 10^8$ cm^{-3}) is ideal in order to avoid

Rydberg-Rydberg interactions which can cause linewidth broadening. In particular, I work with 3D bright optical molasses with circularly polarized beams.

3.3 Three-photon Rydberg Excitation

I employ a three-level excitation scheme, $5S_{1/2} \rightarrow 5P_{3/2}$ (wavelength of 780 nm), $5P_{3/2} \rightarrow 5D_{5/2}$ (776 nm), and $5D_{5/2} \rightarrow nF_{7/2}$, or $nP_{3/2}$ (1260 nm). For the proposed Rydberg constant measurement, excitation to the $nF_{7/2}$ Rydberg state is chosen in order to be able to prepare the atoms in the $m_l = 3$ state necessary to circularize atoms using the adiabatic rapid passage (see next section).

The 780-nm laser, like those used in the cooling of the atoms, is an ECDL that is frequency-stabilized with saturated absorption spectroscopy. The laser beam going into the vacuum chamber has a waist of about 430 μm and power of about 350 μW ($1I_{sat}$= 7 mW/cm^2).

The 776 and 1260-nm lasers are cat-eye reflector ECDLs (MogLabs CEL002) [75], where the coarse wavelength selection is done by changing the angle of a rotatable filter and the external cavity includes a partially transmitting cat-eye reflector. Both lasers are current and temperature controlled with MogLabs' DLC202 diode laser controllers.

To frequency stabilize the 776-nm laser, I use a modified saturated absorption spectroscopy scheme [5] (see Fig. 3.8), where the return beam operates on the $5S_{1/2} \rightarrow 5P_{3/2}$ transition (780-nm beam).

Finally, the 1260-nm laser is locked using a pressure-tuned Fabry-Perot [76] with a free spectral range (FSR) of about 375 MHz (FSR= $c/2n_i L$, where n_i is the index of refraction and L the length of the cavity). To scan the frequency of the 1260 laser, a bellow attached to one end of the cavity can be mechanically moved with a stepper motor which causes the pressure inside the cavity (and therefore its index of refraction) to change. Therefore, by locking the laser to one of the Fabry-Perot peaks
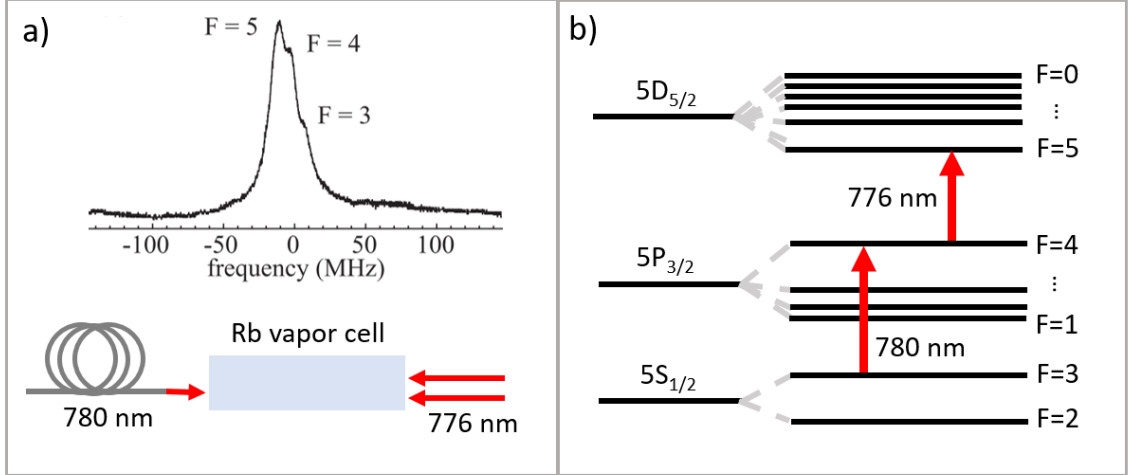
Figure 3.8: a) Simplified optics schematics for the 780 and 776-nm modified satura-
tion absorption spectroscopy setup and an example of the resulting signal
used in the 776-nm lock (spectrum from [5]). b) Atomic energy levels
involved. As the spectrum shows, the small splittings between the differ-
ent F-levels in the $5D_{5/2}$ make it difficult to resolve them. Note that the
hyperfine levels of the $5D_{5/2}$ state are inverted.

and "scanning" the bellow length, I can move the Fabry-Perot peaks in frequency
space and hence the frequency of the 1260 laser. The full scan range of the cavity is
2 GHz and the scaling factor is 12.8 kHz/step.

The reference signals from the 776 nm modified saturation absorption spectroscopy
and the 1260 nm Fabry-Perot are received by photo-diodes and each sent to a MogLabs'
DLC202 diode laser controllers. The DLC202 controller has an internal 250 kHz os-
cillator which dithers the current. This helps produce an error signal, the slope of
which is used to lock to the desired frequency peak.

Both 776 and 1260 nm lasers are free-space propagated into the vacuum chamber.
Their beam waists are approximately half a milli-meter. I send approximately 9 mW
of 776 power ($1I_{sat}$= 120 mW/cm^2) and 1.3 mW of 1260 power into the vacuum
chamber.

3.4   Circularization of Rydberg Atoms

In order to circularize atoms in the proposed Rydberg constant measurement experiment, the system was designed to perform the modified adiabatic rapid passage (ARP) method [77, 78]. This method was selected because it offers very efficient ($>$ 90%) and clean (no state-mixing) population transfers from low-m_l states to circular states. Another circularization technique considered was the "$\mathbf{E}\times\mathbf{B}$" or cross-field method [79] which allows higher principal quantum numbers to be reached. However, this method was not chosen because it can easily yield mixed states [77].

Obtaining a high-l, high-m_l Rydberg state can be challenging due to large number of degeneracies and the fact that they are not optically accessible. The ARP method employs a combination of DC and AC electric fields to lift degeneracies and to dress the resulting Stark states, respectively. The result is that hydrogenic Stark states that would otherwise cross now anti-cross, allowing for adiabatic transitions between states to occur when the DC electric field is slowly varied. In other words, the two applied fields create a "ladder" of anti-crossings with increasing m_l which can be climbed by slowly sweeping the DC electric field while the AC electric field remains at a fixed frequency (see Fig. 3.9).

The AC electric field frequency is set to match the energy difference between $\Delta m_l = +1$ states (see Fig. 3.9), which is determined by the amplitude of the DC electric field applied. In order to use the ARP method in rubidium the initial state must be prepare in $m_l = 3$, where the energy levels match those of hydrogen and a single RF frequency can be used to drive all transitions.

The modified ARP also entails applying an external DC magnetic field, besides the DC electric field, to lift the remaining m_l degeneracies. This is particularly helpful in preventing driving transitions where $\Delta m_l = -1$, which are possible when the RF polarization is not completely σ^+. At the end of the ARP method, when the DC electric field ramp is done, the state should have changed from $|n, m_l = 3\rangle$ to
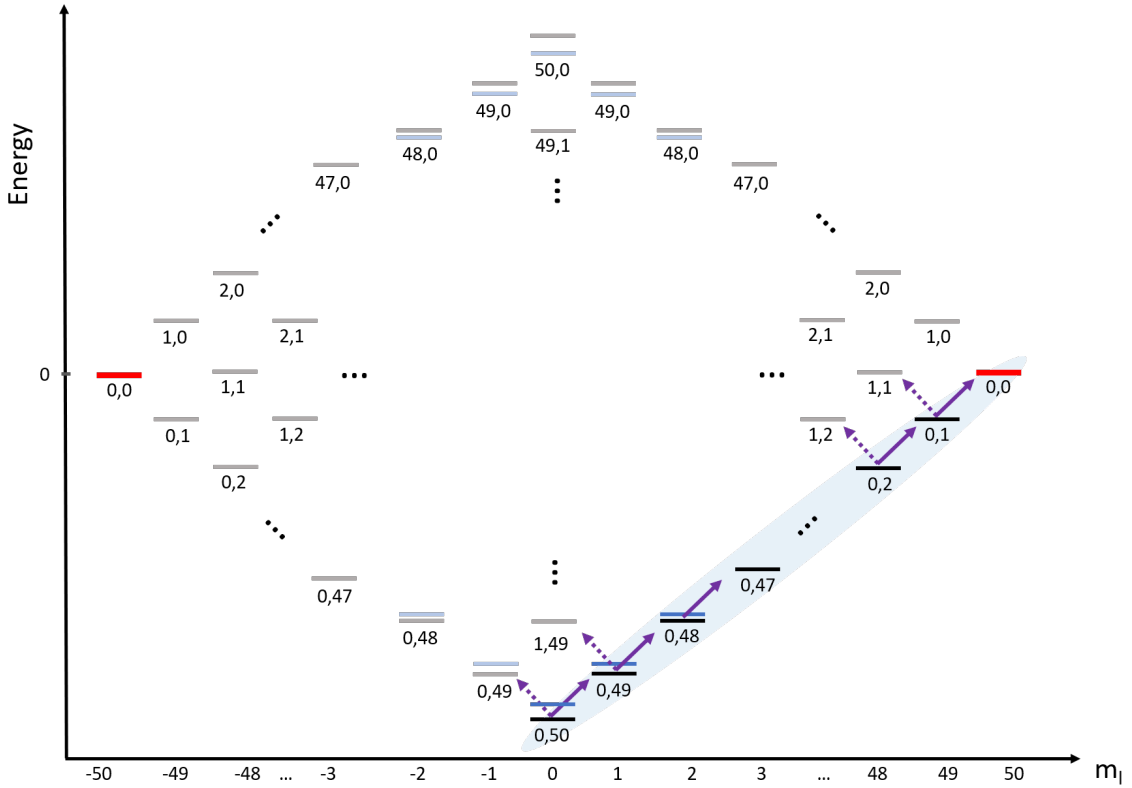
Figure 3.9: Schematics of the hydrogenic atomic levels (black and gray lines) involved
in the ARP method for $n = 51$. The blue energy levels shown correspond
to the low-l states in rubidium which are detuned due to quantum defects.
The numbers below each level correspond to n_1, n_2. The red levels are
the target circular states which can be reached with σ^+ (for $+m_l$) or
σ^- (-m_l) RF polarization. The transitions in this figure are shown with
purple arrows, σ^+ (σ^-) corresponds to solid (dashed) arrows. If the RF
polarization is not perfect, the dashed transitions can occur at the same
time as the solid transitions, yielding mixtures in the final states. We
intend to mitigate this by using a parallel magnetic field which lifts m_l
degeneracies and hence detunes $\Delta m_l = -1$ transitions ("modified ARP",
not shown in the figure).

$|n, m_l = n - 1\rangle$ (circular state) after passing adiabatically through $n - 4$ crossings.

3.5   Detection Method

Thanks to its weakly-bound valence electron, a Rydberg atom can be ionized with
experimentally achievable electric fields (≈ 1 kV/cm). To detect Rydberg states in

the system, I ionize the excited Rydberg atoms by applying a ramped-up high-voltage (HV) pulse to the pair of electrodes along the z-axis (Fig. 3.10). Once the HV ramp frees up ions, they are accelerated towards a micro-channel plate (MCP). There, the ions collide with a phosphor screen and cause an electronic signal which is amplified and then detected by a photon counter. The counter has two timing gates which determine when to count the signal within the experimental cycle. Typically, I use gate A to count the number of Rydberg atoms in the initial Rydberg state and gate B to count those in the final Rydberg state.

The electric-field strength required to ionize Rydberg atoms is proportional to $1/(16n^4)$ for low-l ($l \leq 3$ for Rb) and $1/(9n^4)$ for high-l states [24]. The scaling is different because, as the electric field strength is increased, low-l states go over anti-crossings adiabatically until they reach ionization. On the other hand, high-l states go over anti-crossings diabatically until reaching ionization. For any l, the higher the n, the lower the electric field needs to be to rip the electron from the Rydberg atom. The application of a ramped HV DC field thus allows me to distinguish among the ion signals from the different Rydberg states that are excited.

Figure 3.10 shows the low and high-voltage DC lines in the system. The high voltage is produced by a Stanford Research Instruments HV power supply and fed to a DEI switch which, when triggered, switches from a specified low DC voltage (supplied by a measuring computing box) to the specified HV value. To diminish the noise in the output of the DEI switch, a clamp switch is used. An RC component is then used to introduce a smooth rise to the otherwise square HV pulse. The rise time of the HV pulse is about 20 μs. The amplitude of HV used varies with the principal quantum numbers involved in the transition, with typical values used between 400 and 700 V for $n = 43 - 57$.
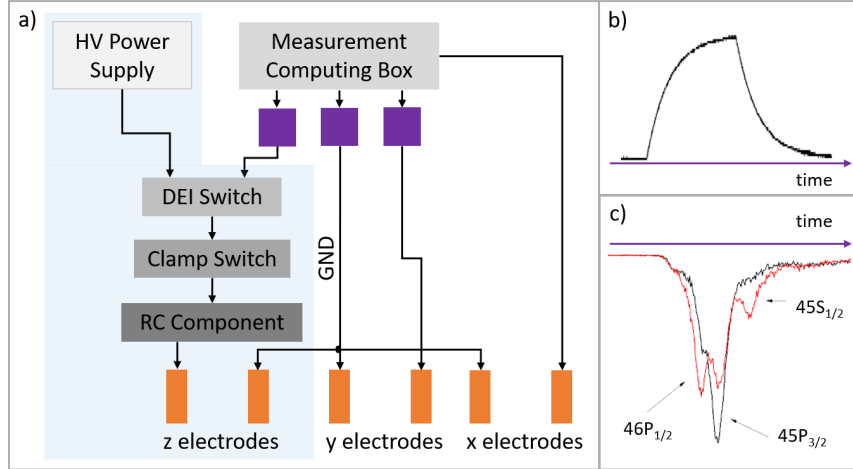
Figure 3.10: a) Schematics of the out-of-vacuum electronics controlling the DC voltages. The shaded area to the left indicates the high voltage electronics. The purple squares are voltage dividers with gains of 0.3 which are used to decrease the noise from the outputs of the measurement computing box. The line going to the x electrodes does not have a voltage divider because larger voltages (> 2 V) are needed along that direction to achieve a net electric-field of zero at the location of the atoms. The orange rectangles represent the in-vacuum electrodes. Not shown are the vacuum interface connectors. b) An oscilloscope trace of the field-ionization (FI) pulse sent to the z electrodes, the rise and decay times are determined by the RC component and the capacitance of the HV cable (1 nF). c) An example of zoomed in (in time) oscilloscope traces of detected signal. The black curve shows counts in the $45P_{3/2}$ state after a three-photon excitation to that state. The red curve shows counts also in the $45S_{1/2}$ and $46S_{1/2}$ which are driven via single-photon microwave transitions. The three different states can be separated thanks to the slow rise of the ionization field.

3.6 Electric-field Zeroing

Due to the high sensitivity of Rydberg atoms to electric fields, it is essential to have precise control of the electric fields in the system in all three dimensions. To this end, three pairs of rectangular copper plates oriented normal to the x, y and z directions are used to cancel out any unwanted stray electric fields. This makes minimizing unwanted shifts and broadening of the spectroscopic peaks possible.
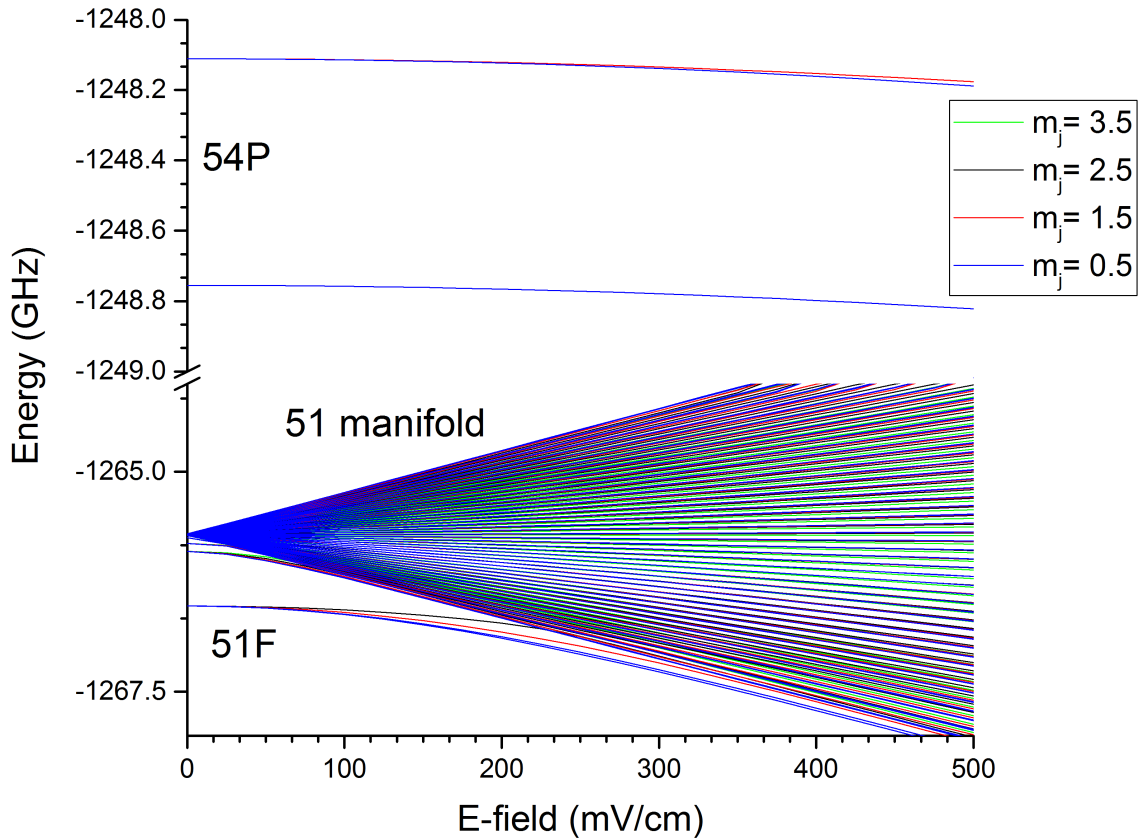
Figure 3.11: Calculated Stark map for n=51 states. Note that the 51F state has a more drastic response to the electric field than that of the 54P state. Energies are with respect to the ionization threshold.

3.6.1 Stark Maps and Calibration

To determine the voltages that need to be applied to the electrodes to cancel out stray electric fields, I perform spectroscopy following the three-level excitation scheme discussed previously. I apply a voltage to one axial direction at a time and measure the population of a nF Rydberg state as a function of 1260-nm laser frequency. This is repeated for a series of voltage steps for each direction. We refer to these as Stark maps (see Fig. 3.12). As the voltage is stepped, the net electric field at the location of the atoms changes and hence the Stark shift of the atomic energy levels changes.
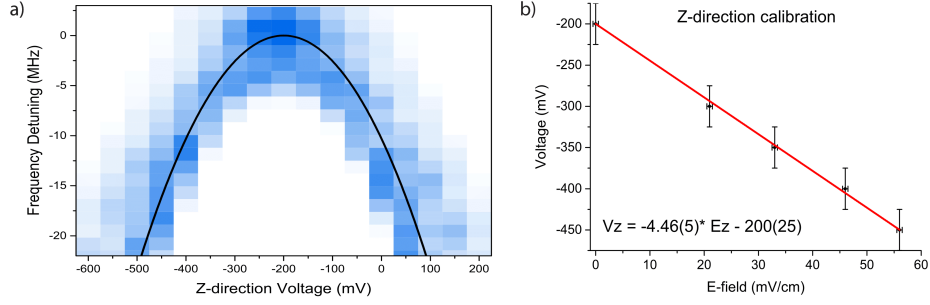
Figure 3.12: a) Experimentally-observed Stark map for 54F state (blue squares) along the z-direction and overlay of corresponding calculated Stark response using the obtained calibration factors (black line). b) Extraction of calibration factors using calculated and observed Stark maps.

For Rydberg atoms, the energy shift follows a parabolic shape according to

$$\Delta_{n,l,m} = \frac{1}{2}\alpha_{n,l,m}F^2, \tag{3.6}$$

where $\alpha_{n,l,m}$ is the polarizability of the Rydberg state $|n, l, m\rangle$. The vertex of the parabola is the location of zero net electric field (see Fig. 3.11).

The three-photon excitation gives access to nP and nF states. However, as seen in Fig. 3.11, F states are more sensitive to electric fields than P states. Therefore, I opt to do Stark maps with F states at high principal quantum numbers.

Once a Stark map is obtained along each direction, one can extract calibration factors, i.e. what voltage is needed to produce a given electric field. To do that, I first determine the zero electric-field point on the Stark Map by determining the vertex of the parabola and assign this also as the zero detuning (reference) point. From there, I select several shifted points and compare them to the calculated Stark maps using the detuning as a link between the applied voltages and the calculated electric fields. A plot of this is shown in Fig. 3.12b, where the error bars for the voltage are determined by the voltage step size and the error bars for the electric field are determined by the electric field step size used in the calculations. A linear fit yields the desired calibration factor. In Fig. 3.12, the solid line over the Stark map is

Table 3.3: Comparison between experimentally obtained electric-field calibration values and calculations using ANSYS Maxwell. All electric fields shown are in mV/cm. The Maxwell simulation values result from applying 1000 mV to one pair of plates at a time.

Direction	Experimentally Observed	Maxwell Result	Factor difference
x	202	143	1.4
y	207	318	0.6
z	269	242	1.1

obtained using the extracted calibration factor for that direction, showing very good agreement. Table 3.4 contains a summary of all experimentally-extracted calibration factors.

The calibration factors are further verified by comparing them to direct calculations using the ANSYS Maxwell software, a finite-element electromagnetic simulation software. These simulation results are obtained from a model of the copper electrodes in the experiment, applying voltages on pairs of electrodes and running the software to obtain the resulting electric field value at the center of the electrode package. A comparison between the experimental and simulated values is shown in Table 3.3; there is fairly good agreement.

3.6.2 Electrodes

The electrodes that control electric fields are housed in the spectroscopy enclosure. These electrodes have several purposes. First, as already described, voltages may be applied to them to cancel out unwanted stray electric fields at the location of the atoms. How well the field may be zeroed depends on the noise in the applied voltages.

The voltages are controlled independently in each direction. The x-direction electrodes (top and bottom plates, see Fig. 3.13) are controlled directly with a computer-controlled analog voltage supply (measurement computing USB 3114, see Fig. 3.10). One electrode is grounded while the other can receive a voltage from zero to ± 5 V.
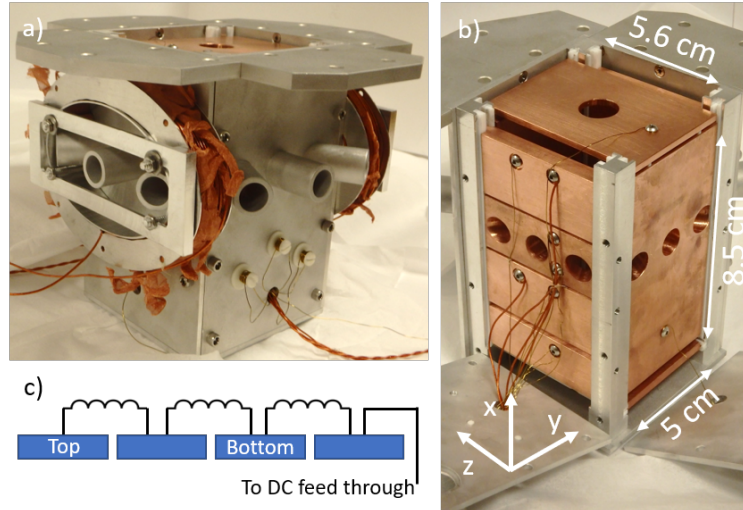
Figure 3.13: a) The fully assembled spectroscopy enclosure. The eliptical pieces on two sides are the in-vacuum coils. On two of the sides of the enclosure there are three inductors placed on the surface (white ceramic screws pictured on the bottom half of the right face) which are meant to block AC signals from the in-vacuum DC circuit. b) The inner layer of the spectroscopy enclosure, which consists of the electrodes. There are a total of 12 electrodes: four exclusively for DC voltage control and eight for a combination of AC and DC signals. The distances between parallel plates are marked. c) Schematics of the circuit connections for the in-vacuum inductors in the DC line. These inductors filter out RF signals from the DC line. The number of loops on each inductor was adjusted until the RF disturbance in the resulting DC signal was minimal, resulting in 18 turns with a reactance of about 3 kΩ per inductor.

The noise in the x-direction voltage is about 2 mV. Since the typical zeroing voltages in this direction are of the order of a couple of volts, this noise is less than 1% of the voltage sent.

The y-direction electrodes are controlled by the same source as those of the x-direction but a voltage divider is added to the line before the in-vacuum plates in order to reduce noise. This is because the typical zeroing voltages in this direction fall in the tens of milli-volts, in other words, it is more sensitive to noise. After the voltage divider, the noise is 0.4 mV, which is less than 5% of the voltage applied. As in the case of the x-electrodes, one electrode is grounded while the other can receive a voltage from 0 to ± 1 V.

Table 3.4: Electric field characterization. Use the following expression: $V_i = fE_i - V_{i0}$ where V_i and E_i are the voltage and electric field (in mV/cm) in the i direction, f is the calibration factor in cm and V_{i0} is the voltage that corresponds to net zero electric field in the i direction. Note that V_{i0} can vary slightly day-to-day but the calibration factor does not. All voltages are in mV.

Direction	Calibration Factor	Zeroing Voltage	Systematic Noise
x	-12(2)	-1467(35)	2.0
y	-4.83(17)	0	0.4
z	-4.46(5)	-200(25)	0.4

In the z-direction, one plate is grounded while the other is set to a low DC voltage for most of the experimental cycle to help zero the electric field. The low DC voltage is also controlled by the measurement computing USB 3114 and sent through a voltage divider to minimize noise (see Fig. 3.10). As a result, in this direction the noise is 0.4 mV, which is less than 0.5% of the typical zeroing voltage.

A second purpose of the z-direction electrodes is detection. At the end of each experimental cycle, the same z electrode that receives low DC voltage receives a high voltage pulse that ionizes Rydberg atoms and accelerates the ions towards a micro-channel plate for detection (more details in the previous section).

Another function of the electrodes, this time the pair along the y direction, is to produce the time-dependent RF electric field necessary for circularizing the atoms. This pair of electrodes is actually divided into four separate pieces each being held apart by small macor cylinders (see Fig. 3.13). The first piece from the top receives a 0-degree shifted RF signal while the third receives the same signal but with a 180-degree phase shift, and the second and fourth pieces are grounded. This leads to an electric field that points in the vertical direction (parallel to the plates, see Fig. 3.14) and changes directions from up to down at the location of the atoms as the input RF field oscillates. Figure 3.14 shows the electronics used to achieve this control of the RF field.
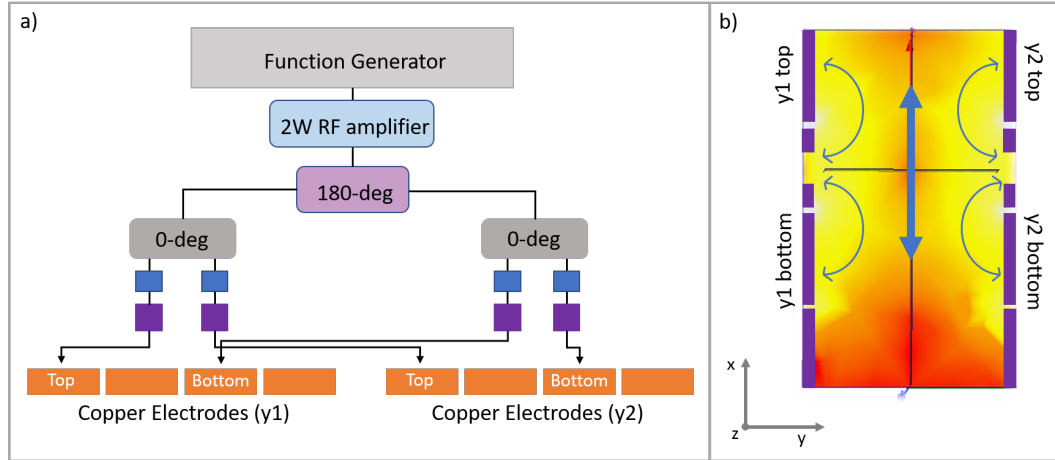
Figure 3.14: a) Schematics of the electronics along the RF line. The 180-degree splitter divides the signal in two with a relative phase difference of 180 degrees. The 0-degree splitter splits the signal equally in two with no phase difference introduced. Blue rectangles are in-line capacitors which are placed as filters to prevent DC signals from affecting the RF line. Purple rectangles are adjustable phase shifters to correct for small deviations in the relative phases. b) The yellow and orange background shows simulation results of the RF field using the ANSYS HFSS software where the yellow indicates the highest electric field amplitude and the darker orange is the lowest electric field amplitude. The simulation shows a constant amplitude at the location of the atoms (where thick blue arrow is). The blue arrows help visualize the direction of the RF electric field and the purple rectangles show roughly the location of the electrodes.

The RF response of the electrode package was tested outside of vacuum. One key aspect to check was that the phases of the plates were matched, meaning that the top pieces from the two plates facing each other were in phase but 180-degrees out of phase with the third pieces on each side. This was done by connecting the RF twisted-pair wires to a LeCroy oscilloscope, using XY mode and adjusting the in-line phase shifters until each plate was phase-matched as needed. A phase-matched pair yields an XY signal that is a straight line with a positive slope, since the two amplitudes increase and decrease at the same time. A pair that is 180 degrees out of phase results in a straight line with a negative slope, a pair with a 45 degrees offset displays a circle, and phase offsets in between display an ellipse.
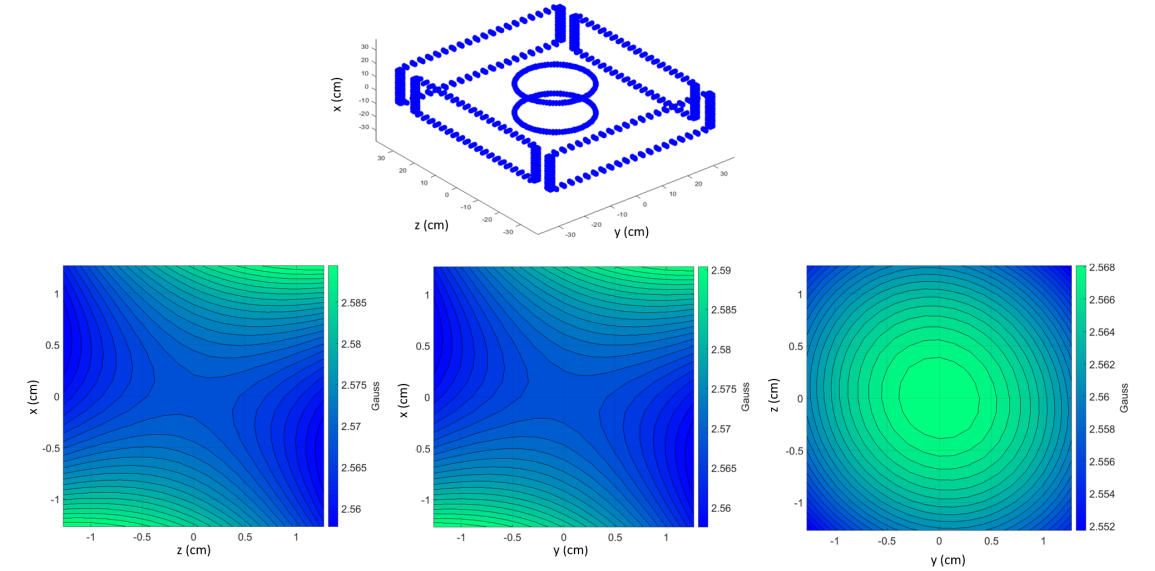
Figure 3.15: Top panel: schematics of the compensation coils in the experimental setup. The circular pair is wrapped around the vacuum chamber while the two rectangular pairs are supported by the 80-20 structure that holds the entire system. Bottom panel: calculations of the total magnetic field, in Gauss, produced by the compensation coils when the rectangular coils are set to 1.5 A and the circular coils to 3.0 A. In the calculations, the coils are divided into small, finite pieces and the Biot-Savart's law is used to obtain the magnetic field. We assume the wire occupies 50% of the space allotted for the coil.

3.7   Magnetic-field Zeroing

Minimizing the stray magnetic fields is also critical for precision measurements in the experimental setup. To this end, I led the design, construction and characterization of three pairs of compensation coils that produce constant magnetic fields that help cancel out undesired fields at the location of the atoms. Figure 3.15 shows the geometry of the compensation coils as well as simulations showing the magnetic field distribution near the center of the spectroscopy enclosure. Each coil pair has the same current direction. These currents are controlled with Kepco power supplies remotely controlled with the same measuring computing box used to control voltage to the electrodes. The uncertainty in the currents is 5 mA.

3.7.1 Magnetic Field Zeroing with Microwave Spectroscopy

To know the magnetic field produced at the location of the atoms by each compensation coil pair, I use microwave spectroscopy on the $54P_{3/2} \rightarrow 55D_{5/2}$ transition. In contrast with the proposed experiment for the Rydberg constant measurement, in this case I am in a regime of low magnetic field where the typically observed shifts are on the order of 0.1-1 MHz, which is small compared to the fine structure splittings (54P has a fine structure splitting of 642 MHz while the 55D state has a splitting of 70 MHz). The energy shift caused by the magnetic field B along the z direction is

$$E_{Z,J} = \mu_B B m_j g_j, \tag{3.7}$$

where μ_B is the Bohr magneton and

$$g_j = 1 + (g_e - 1)\frac{j(j+1) - l(l+1) + s(s+1)}{2j(j+1)}, \tag{3.8}$$

where g_e is the electron's g-factor. Figure. 3.16b shows all of the possible transitions for the three possible polarizations σ^+, σ^- and π, each of which has four transitions. I must take all polarizations into account because initially the unknown, non-zero magnetic field defines the quantization axis, which might be at a random angle with respect to our axis. Figure. 3.16a shows the calculated atomic energy levels as a function of magnetic field (using Eq. 3.7 and Eq. 3.8). The three main branches represent each of the polarizations, where the circularly-polarized outer branches respond more to the magnetic field.

To zero the magnetic field, I use Figure. 3.16a as a guide. I drive the $54P_{3/2} \rightarrow 55D_{5/2}$ transition and look for a linear response of the transition frequency shift to the field. I first prepare the $54P_{3/2}$ state via the three-photon excitation scheme described previously and drive the one-photon microwave transition to the $55D_{5/2}$. I pulse the
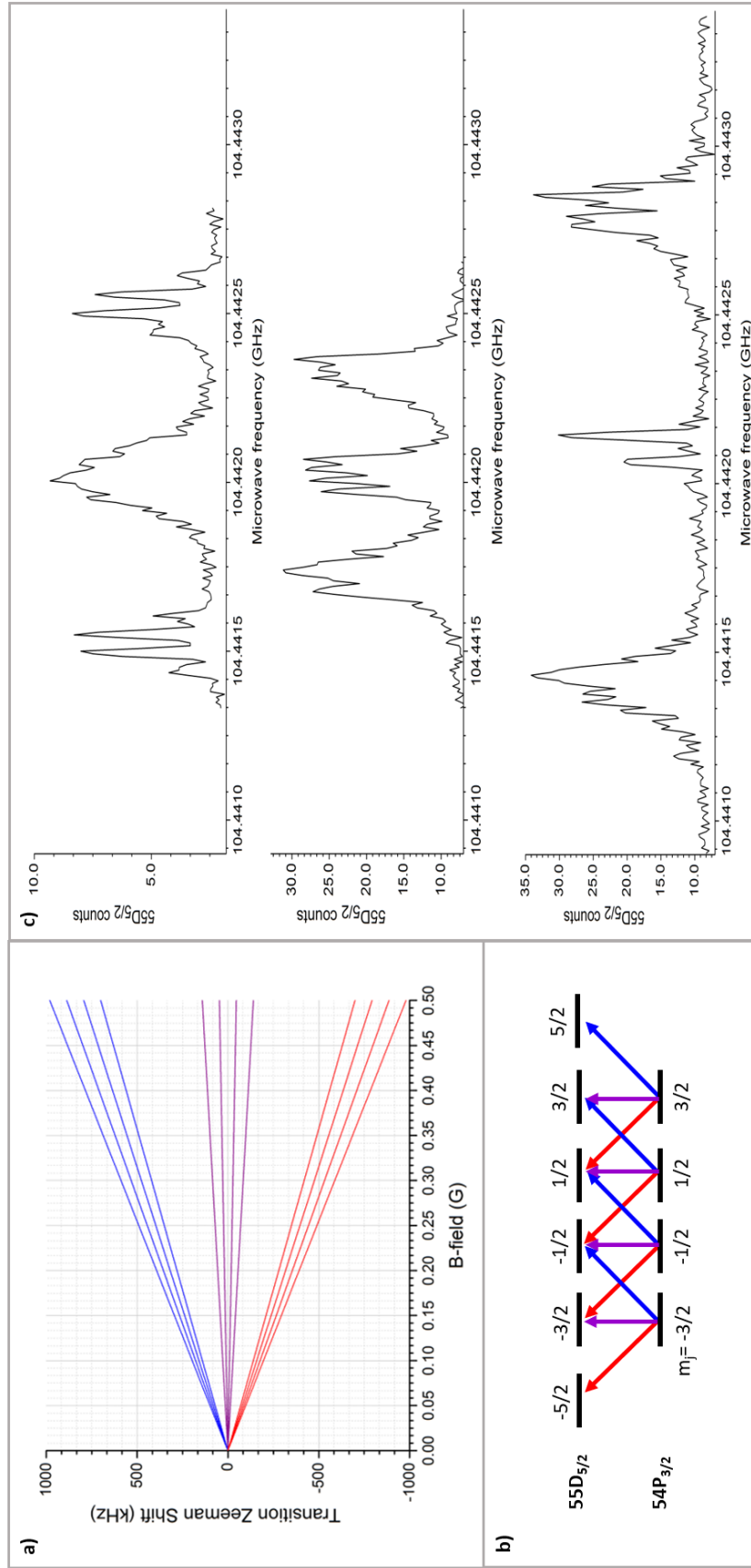
Figure 3.16: a) Calculation of Zeeman splitting as a function of magnetic-field amplitude for different microwave polarizations: σ^+ (blue), π (purple) and σ^- (red). b) Schematics of the m_j states involved and the transitions each polarization drives. c) Magnetic field calibration scans for all three directions. A non-zero magnetic field is applied along the x, y and z directions (from top to bottom).

output of a microwave generator and feed it to a frequency x2 multiplier which is connected to a horn. The horn is placed near the vacuum chamber viewing port 3 as shown in Fig. 3.1. The pulse is 40 μs long and occurs after the three-photon excitation pulses and before the field-ionization pulse. The microwave power is adjusted to minimize power broadening and obtain as narrow a linewidth as possible, which is typically the Forrier-limited linewidth (22 kHz wide for the interaction time used). I also use this transition to do electric field zeroing with finer resolution due to the narrower linewidths (our optical linewidths are about 3-5 MHz).

As the magnetic field is varied, the spectral lines should diverge in one direction and converge in the other direction onto a single point (this is the minimum magnetic field point) before starting to diverge again. This is exactly what it is shown in the experimental data in Figure 3.17, where I scan the microwave frequency over the $54P_{3/2} \rightarrow 55D_{5/2}$ transition for different current steps of the coils that are along the y and z directions. By repeating this procedure for all three directions and doing a couple of iterations, I reach current settings which result in minimal magnetic fields. The smallest magnetic field I can confidently attain in the experimental setup is limited only by the uncertainty in the current which is 5 mA in each direction and limits the magnetic-field minimum to about 2.5 mG. This is enough for the precision measurements discussed in this thesis.

3.7.2 Magnetic Field Calibration

After the magnetic field is minimized well, the calibration scans can be done. To do so, the same transition is scanned over but this time a large magnetic field is intentionally applied along one direction at a time. The resulting scans are shown in Fig. 3.16 where the currents for the y and z directions were set to 0 A and the current for the x direction was set to 1 A. These current values are chosen because they are roughly 1 A away from the determined zero magnetic field values. By examining
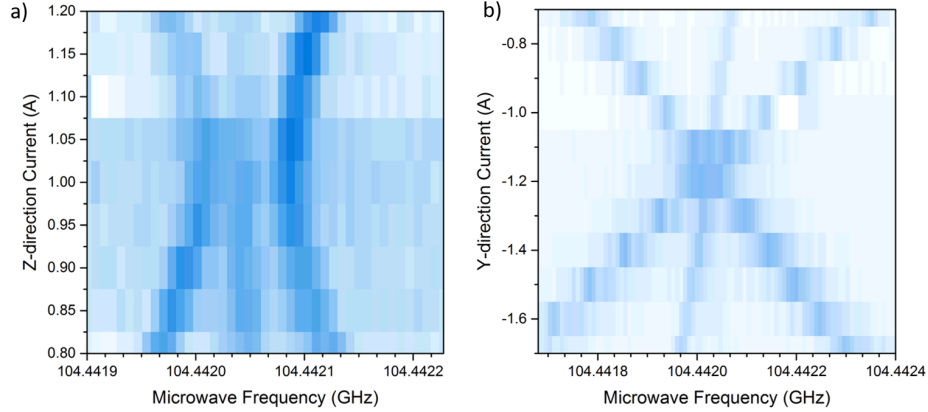
Figure 3.17: Experimentally obtained magnetic field maps when a) scanning one direction while the other two are not minimized and b) scanning one direction when all other directions are minimized. Comparing a) and b) it can be seen that how much the lines come together depends on the magnetic field along the other two directions. The field minimum is always where the three branches come closest. Here, darker blue means higher population with the difference between the two scans being the location of the molasses with respect to the excitation beams.

the scans in Fig. 3.16 we can expect the z direction to have the largest calibration factor because the spectral lines are the most sensitive to the current change. The individual peaks in all of the scans are Fourier-limited (22 kHz wide) while there are five unresolved peaks (containing 2-4 unresolvable peaks) which are broader. While all three scans show the three branches we expect from the calculations shown in Fig. 3.16, each direction has its own signature spectrum. The x direction has well-resolved outer features which correspond to the circularly-polarized branches, while the linearly-polarized branch is unresolved. The y direction is the opposite, with the central feature being well resolved and the outer peaks not. Finally, the z direction is similar to y but instead of four peaks in the linearly polarized branch, only two appear. These differences are probably caused by the quantization axis being aligned with the direction of the non-zero magnetic field, which is different in each scan. In the case of the z direction this results in only $m_j = \pm 3/2$ in the $54P_{3/2}$ state being populated, limiting the number of transitions possible. The different resolutions of

Table 3.5:
Experimentally determined calibration factors, magnetic field zeroing currents and the uncertainty in magnetic field (from 5 mA resolution due to equipment) for the coil pairs in each direction. In the experimental set up, the directions are labeled as A&B (y), C&D (z) and Top&Bottom (x).

Direction	Calibration Factor (mG/A)	Zeroing Current (A)	B-field Unc. (mG)
x	325.55(1)	-1.170(5)	1.6
y	353.85(1)	0.100(5)	1.8
z	162.86(2)	1.050(5)	0.81

each branch might be due to different coupling factors from the changing quantization axis.

Despite the differences among the scans, roughly the same procedure can be used to extract the calibration factors from them. I determine the central frequency for each peak in the scan and take the frequency difference between pairs of peaks. I compare the experimentally observed frequency differences with those from the calculation in Fig. 3.16 and extract preliminary magnetic field values. Finally, I average all extracted field values and divide the result with the change in current from the previously determined zero-field current value. The resulting calibration factors are shown in Table 3.5, where the uncertainties shown are due to the uncertainties in magnetic field (≈ 3 mG, based on the linewidth of the scans used to zero the magnetic field which limits how small a peak separation can be observed) and in the current (determined by half the smallest current step possible with the available equipment, 5 mA).

CHAPTER IV

Precision Measurement of $nS_{1/2}$ Rubidium-85 Hyperfine Structure Splittings

Hyperfine structure splittings hold important information about the nucleus of an atom such as the value of the electronic wavefunction at the location of the nucleus and nuclear quadrupole moment [58]. Moreover, hyperfine states are used in quantum computation with ions and neutral atoms [80, 81]. This makes the implications of knowing the hyperfine splittings well far-reaching. The most recent experiments for hyperfine structure splittings of $nS_{1/2}$ Rydberg states of Rubidium have yielded uncertainties of at best 60 kHz for rubidium-85 [49] (relative uncertainty of 0.089) and 9 kHz and below for rubidium-87 [82] (relative uncertainty of 0.0021). In this chapter I present precision measurements of the rubidium-85 splittings with uncertainties of 2 kHz and below (relative uncertainties of 0.01 and below). I use these splittings, ν_{HFS}, and

$$\nu_{\text{HFS}} = \frac{A_{HFS}}{[n - \delta_s(n)]^3}, \tag{4.1}$$

to extract the hyperfine structure constant, A_{HFS}, with an uncertainty of 170 MHz, which is an improvement of an order of magnitude from previous measurements which had uncertainties of 1.4 GHz [49].
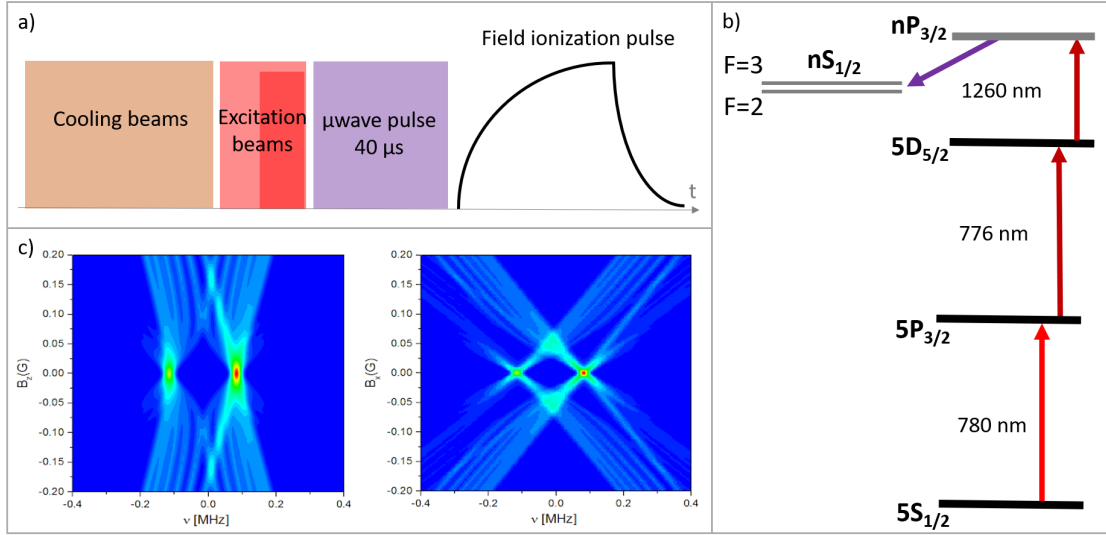
Figure 4.1: a) Timing sequence used in each experimental cycle. b) Excitation scheme, where the $nP_{3/2} \rightarrow nS_{1/2}$ transition is a microwave transition. c) Calculations of the $45P_{3/2} \rightarrow 45S_{1/2}$ F=3 (right peak) and F=2 (left peak) hyperfine peaks as parallel (left panel) and transverse (right panel) magnetic field is changed. Highest excited-state population is shown in red, while dark blue is essentially zero. Using this transition to perform magnetic-field zeroing is challenging due to the many energy levels available. However, once the magnetic field has been zeroed properly using a different transition, ensuring a constant net field of zero for the hyperfine structure measurements is relatively simple since small deviations lead to broader linewidths.

4.1   Procedure

I perform the precision measurements in the vacuum chamber described in Chapter III which has electric and magnetic field control in all three directions. Atoms are cooled in an optical molasses and Rydberg states are reached via a three-photon excitation scheme $5S_{1/2} \rightarrow 5P_{3/2}$ (wavelength of 780 nm), $5P_{3/2} \rightarrow 5D_{5/2}$ (776 nm), and $5D_{5/2} \rightarrow nP_{3/2}$ (1260 nm) (see Fig. 4.1). I then scan the frequency of a microwave source to drive the transition $nP_{3/2} \rightarrow nS_{1/2}$ for $n = 43, 44, 45$ and 46. The excitation beams as well as the microwave signal are all pulsed (see Fig. 4.1). The population in the excited state is measured by applying an electric-field ionization ramp which
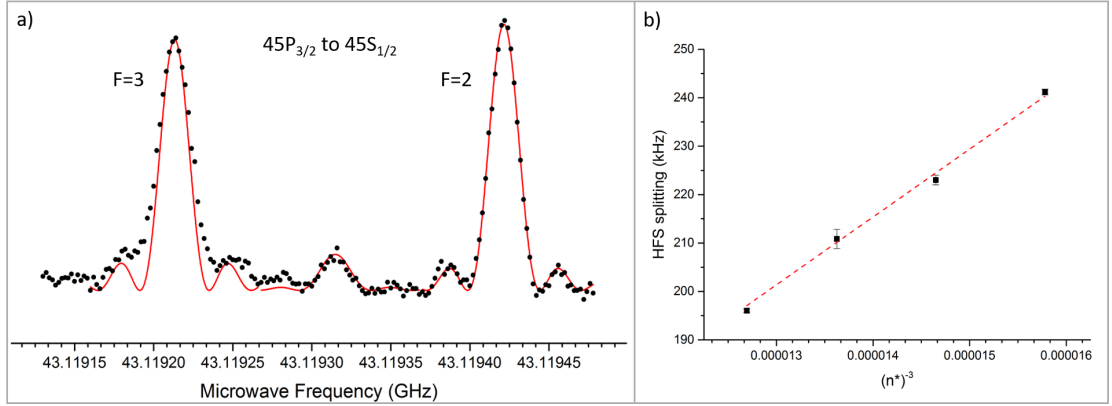
Figure 4.2: a) Averaged scan for the $45P_{3/2} \rightarrow 45S_{1/2}$ transition (average of 6 scans with 300 experimental cycles per scan). The red lines follow Eq. 4.2 and are meant to guide the eye. The two largest peaks are the F=3 and F=2 hyperfine structure peaks of the $45S_{1/2}$, the smaller peak in the middle is thought to be from the interaction of an atom in the $45S_{1/2}$ F=3 state and another atom in the $45S_{1/2}$ F=2 state. b) Hyperfine structure splittings as a function of n^{*-3} where $n^* = n - \delta_l(n)$, the dashed red line is meant to highlight the linear dependency which is expected.

results in the $nP_{3/2}$ state ionizing first (at lower electric-fields) closely followed by the $nS_{1/2}$ state. To distinguish the populations, I use separate photon-counter gates, one only for $nS_{1/2}$ and the other for all possible states. I monitor the percent of population in the $nS_{1/2}$ state as the microwave frequency is scanned.

4.2   Results

I am able to obtain Fourier-limited peaks, which for the pulse width, $\tau = 40\mu$s, results in linewidths of 22 kHz (see Fig. 4.2). In the scans, the Fourier sidebands are also resolvable with the expected periodicity of $\omega_\mu \tau = n\pi$, where ω_μ is the microwave radial frequency. In order to obtain this resolution, it is critical to perform excellent zeroing of the magnetic and electric fields in the excitation area. The stray magnetic fields are zeroed down to $\leq$2.5 mG by changing the currents in three pairs of orthogonal compensation coils and observing the resulting Zeeman shift on the

microwave spectral lines as discussed in Chapter III. For this procedure, I use the $54P_{3/2} \rightarrow 55D_{5/2}$ transition which yields a cleaner spectrum than that which would result from $nP_{3/2} \rightarrow nS_{1/2}$ transitions (see Fig. 4.1). Similarly, the electric field is also zeroed by first performing Stark spectroscopy [83] with high $nF_{7/2}$ states, where line-shape center location is measured as a function of voltages applied to in-vacuum electrodes (see Chapter III for more details). By also using microwave spectroscopy as a final step, a finer detection of unwanted electric field shifts can be attained thanks to the narrow linewidths.

Table 4.1 lists the extracted hyperfine structure splittings for $n = 43, 44, 45$ and 46 with their respective statistical uncertainties. A sample curve for $n = 45$ is shown in Fig. 4.2, where the red curves are meant to guide the eye and follow

$$P_e = A \left[\frac{\Omega^2}{\Omega^2 + (\nu - \nu_c)^2} \right] \sin^2 \left[\frac{1}{2} \tau \sqrt{\Omega^2 + (\nu - \nu_c)^2} \right], \tag{4.2}$$

where P_e is the excited-state population, A is the amplitude of the function, Ω is the on-resonance Rabi frequency, ν is the microwave frequency being scanned, ν_c is the main peak's center frequency and τ is the interaction time, which for these experiments is fixed at $40\mu s$. I use Eq. 4.2 to determine the line-center for each peak. The scan shown in Fig. 4.2 is the average of 6 scans, each with 300 experimental repetitions. For the other n-states (shown in Fig. 4.2b), 3-4 averages are taken, each with 300 experimental cycles as well. The individual A_{HFS} are extracted by using the format of Eq. 4.1. To obtain the final A_{HFS} displayed in Eq. 4.3, a weighted average of all A_{HFS} in Table 4.1 is done.

The resulting expression for the $nS_{1/2}$ hyperfine splitting is

$$\nu_{\text{HFS}} = 15.37(17)\text{GHz} \frac{1}{[n - \delta_s(n)]^3}, \tag{4.3}$$

where $\delta_s(n)$ is the quantum defect of ns-states obtained using Eq. 2.9 and values

Table 4.1:
Measured hyperfine structure (HFS) splittings for different $nP_{3/2} \to nS_{1/2}$ transitions of rubidium-85 and their respective hyperfine structure constants, A_{HFS}. Only statistical uncertainties are displayed.

n	HFS splitting (kHz)	A_{HFS} (GHz)
43	241.2(6)	15.284(39)
44	223(1)	15.222(77)
45	211(2)	15.47(12)
46	196.0(4)	15.440(30)

Table 4.2: Uncertainty budget for the A_{HFS} measurement of rubidium-85 ns states.

Source	Uncertainty in A_{HFS} (MHz)
Statistical	151
Magnetic field	52
Rydberg counts	46
Electric field	33
AC shift	24

from Table 2.1. The A_{HFS} of 15.37(17) GHz is in good agreement with the previous measurement from [49] of 14.6(14) GHz.

4.3 Uncertainty Budget

The main source of uncertainty that limits the measurement is the statistical uncertainty of 151 MHz. I also explored several other possible sources of uncertainty to the measurement for which results are shown in Table 4.2. To check for effects in the splitting due to stray electric fields, I apply well known electric fields one direction at a time and record the hyperfine splitting at each electric-field step (see Fig. 4.3). I find that there is no significant change in the splitting due to electric fields, meaning that the two peaks are affected equally by stray electric fields within the attained resolution. This is expected since the two peaks are from an nS state and hence respond to the applied electric fields equally.

To explore the effects of magnetic-fields, I follow a similar procedure as for the
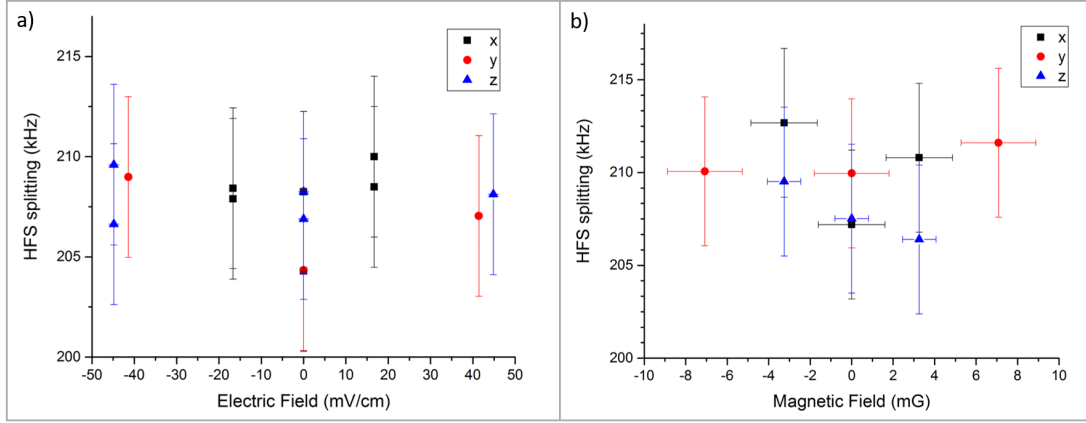
Figure 4.3: Measured hyperfine structure splitting as the electric (a) and magnetic (b) fields are changed one direction at a time. For both instances, the remaining two directions are kept fixed at the minimum magnetic or electric field values. All scans were done for the $45P_{3/2} \rightarrow 45S_{1/2}$ microwave transition.

electric field where the hyperfine structure splitting is recorded as the magnetic field is changed one direction at a time (see Fig. 4.3). I find that within ±10 mG, there is no significant change in the measured splitting. This is in good agreement with the calculations shown in Fig. 4.1c, where within those magnetic field values (±10 mG) the splitting does not seem to change, only a small broadening of the lines is observed.

Another possible concern would be the effect of Rydberg-Rydberg interactions. To investigate this, I make measurements as a function of number of detected Rydberg atoms and find that the hyperfine splitting does not change as I vary the number of Rydberg atoms up to 16 (see Fig. 4.4). As the number of detected Rydberg atoms increases past that point, a slight increase in the hyperfine structure splitting is observed. I do not expect effects from van der Waals interactions in the measurements because of the low density of the cold atomic clouds in the setup, estimated to be about 10^7 cm^{-3} (MOT densities have been measured to be a maximum of 1.5×10^9 cm^{-3}). From there, at most 45 ions from ionized Rydberg atoms are detected on the microchannel plate (MCP) which has a detection efficiency of about 30%. Therefore, I must

have approximately 150 Rydberg atoms in the sample or 3.5×10^4 cm^{-3} (assuming a molasses radius of 1 mm). The van der Waals interaction can be expressed as C_6/D^2, where C_6 is the van der Waals coefficient and D is the density of the sample. From [84] I have $C_6 = 5.4 \times 10^{-58}$ Jm^6 (for s-states) and use the estimated density of Rydberg atoms in the sample to arrive at a calculated van der Waals shift of 6.7×10^{-46} Hz, which is negligible. The measurements in Table 4.1 were all done in the low Rydberg-atom regime (16 Rydberg counts and below). That combined with the estimates presented above lead me to expect measurements to have no significant van der Waals shifts.

I also check for AC-Stark shifts caused by the microwave used to drive the $nP_{3/2} \rightarrow nS_{1/2}$ transitions. To this end, I measure the hyperfine structure splitting for different microwave powers and observe no significant difference in the range of powers tested (see Fig. 4.4b). Notice that I do not do higher microwave powers because this would cause an unwanted broadening of the peak's linewidth. Based on the fittings, I estimate -39 dBm to correspond to a Rabi frequency of 8-9 kHz while powers of -40 dBm and below correspond to about 5 kHz. Using these values, calculated matrix elements of about $1000ea_0$ and a calculated AC polarizability of 1 MHz/(V/m)^2 (for $n = 43\text{-}46$ the AC polarizability remains roughly the same), we obtain sub-Hertz expected AC Stark shifts (using Eq. 3.6) which is well below the statistical uncertainty.

The hyperfine structure splitting of the $nP_{3/2}$ state is expected to be small. Since there is no clear indication of sub-splitting of the two observed features, I conclude that the $nP_{3/2}$ hyperfine splitting for these n numbers are below the width of the peaks. Moreover, I repeated the measurements on separate days and found that the day-to-day change in the measured hyperfine splittings were in agreement with each other within error. The systematic uncertainties presented in Table 4.2 are the standard error of the mean values from the data shown in Figures 4.3 and 4.4 and do not contribute significantly to the final uncertainty of A_{HFS}.
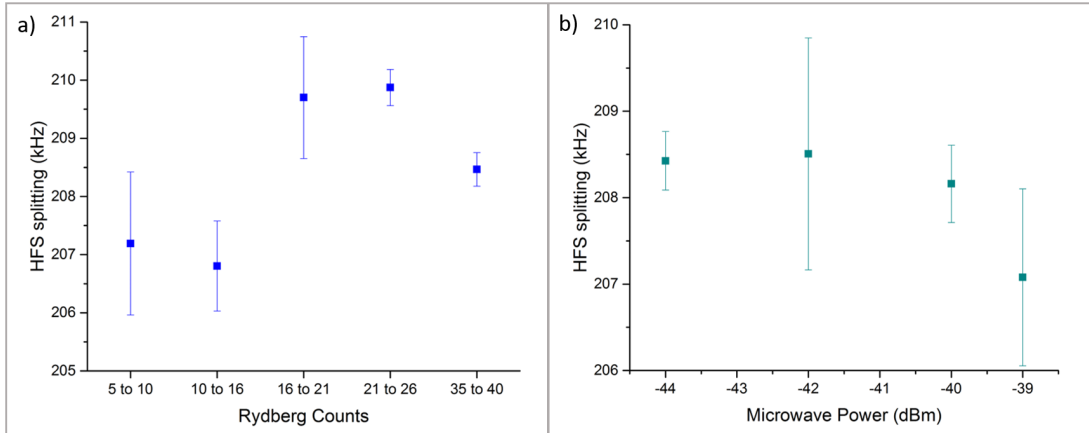
Figure 4.4: Measured hyperfine structure splitting for different number of Rydberg counts (a) and different microwave generator output powers (b). All of the systematic scans were done for $n = 45$.

4.4 Discussion

As shown in Fig. 4.2, a typical hyperfine structure splitting scan consists of the expected two main peak (F=3 and F=2) and a central feature. This central feature appears consistently in the scans, it is Fourier-limited and has Fourier sidebands. A possible explanation could be that this feature is caused by the interaction between a Rydberg atom in the F=3 hyperfine state and another in the F=2 state. Signal from such a molecule would appear exactly halfway between the F=3 and F=2 peaks, as it is the case for the feature we observe, but further analysis would be needed before it can be determined with certainty that this is from a mixed hyperfine state molecule.

In conclusion, I have measured the hyperfine structure splitting of $nS_{1/2}$ states of rubidium-85 with a precision that is an order of magnitude better than previously attained measurements and still within good agreement with such values. The main limitation to the precision was statistical uncertainty. Other effects such as Stark shifts, magnetic-field effects, Rydberg-Rydberg interactions and microwave AC shifts were accounted for but had small or no effect in the measured splittings.

CHAPTER V

A Study of Systematic Uncertainties in the R_∞ Measurement

In order to help solve the proton radius puzzle, we have proposed to perform a measurement of the Rydberg constant, R_∞, using cold circular states of rubidium. The idea is to use optical molasses to cool down rubidium atoms while in an optical lattice. As discussed in Chapter III, we will use a three-photon excitation scheme to prepare the atoms in a $nF_{7/2}, m_l = 3$ state which is necessary to circularize them using the modified adiabatic rapid passage (ARP). Once circular states are obtained, the DC electric and magnetic fields used in ARP will remain on to prevent the circular state from mixing with other nearby states. The frequency of a microwave transition between a circular and a near-circular state will be driven by amplitude-modulating the optical lattice (see Chapter II) [23]. Finally, to detect the state populations, we will use state-selective field ionization (see Chapter III). In simple form, the Rydberg constant will be extracted from

$$\nu_{a,b} = hcR_\infty \left(\frac{M}{M + m_e} \right) \left(\frac{1}{n_a^2} - \frac{1}{n_b^2} \right) + \Delta\nu_{a,b}, \tag{5.1}$$

where $\nu_{a,b}$ is the transition frequency between states a and b, n_a and n_b are the principal quantum numbers of those states and $\Delta\nu_{a,b}$ includes all energy shift corrections

that need to be accounted for. In Chapter II, a detailed review of these corrections is given. In this chapter, I present the expected corrections and their respective relative uncertainties for the sample atomic transition $|51, 0, 0, 50\rangle \rightarrow |53, 1, 1, 50\rangle$ (in parabolic basis). Ideally, this proposed measurement should be done with at least two other transitions to improve statistical uncertainties.

The uncertainty values presented in Table 5.1 at the end of this chapter are obtained by accounting for all possible sources of uncertainty in the calculation of the energy shift and propagating the error using

$$\delta f(x_1, ...) = \sqrt{\sum_i \left(\frac{\partial f}{\partial x_i} \delta x_i \right)^2}, \tag{5.2}$$

where $f(x_i, ...)$ is the energy shift expression which depends on parameters x_i and δx_i is the error for the ith parameter.

5.1 Lattice-induced Shift

The main source of uncertainty on the proposed ground-based experiment is the residual lattice-induced shift. The resulting relative uncertainty, $\delta \Delta \nu / \nu$, is 3.2×10^{-11} and it is mainly due to laser-intensity fluctuations.

The lattice shifts and uncertainty results presented in Table 5.1 are obtained through simulations based on Eq. 2.50 where I specify the two atomic states of interest, a laser-beam geometry, and the wavelengths and intensities of the beams that form the lattice. For these calculations, it is assumed that the alignment between the normal vectors of the lattice planes and the quantization axis is perfect. The relative beam intensities and other conditions can be chosen such that two pairs of lattice beams cause opposite transition shifts that cancel each other. To achieve this type of magic lattice in the simulations, the intensity of one of the beams is adjusted until the calculated transition lattice shift reaches a minimum. In Table 5.1, the

corresponding uncertainties are generated by the assumption that the intensities can be controlled with a 1% relative uncertainty. Note that even though close to "magic" lattice conditions (where both states involved in the transition experience the same light shift) can be obtained by carefully selecting what states to use (see Fig. 2.5), there is still a small but non-zero light shift difference between the two transitions states which is what we would try to compensate for by adjusting relative intensities.

Smaller lattice shift uncertainties are possible through the use of shallower lattices and fewer laser beams. To achieve this, lower atomic temperatures are needed (see Fig. 2.8), for which other well-known cooling methods can be employed [85]. Moreover, for a similar experiment in micro-gravity conditions, the depth of the lattice could be further decreased or even eliminated (except for driving transitions). This reduction of the lattice-induced uncertainty may be the only improvement necessary to achieve a competitive relative uncertainty in the Rydberg constant value. In Table 5.1, lattice-shift estimates are presented for two cases of the lattice depth: one suitable for ground-based experiments and the other for micro-gravity experiments. Table 5.1 also shows that the lattice-induced shift represents the by-far dominant source of systematic uncertainty and needs to be addressed first in any incremental improvement of the experiment.

5.2 Quantum Defect Correction

In Chapter II I discussed how quantum defects can be included in the hydrogenic theory to account for the effects of the valence electron penetrating and polarizing the ionic core. The quantum defect corrections are due to deviations from the hydrogenic $1/r$ potential. This applies to both the penetration [24] (zero for the case of circular states) and the polarization quantum defects. This issue could be avoided in the first place by using hydrogen instead of rubidium. However, experimental obstacles due to the large recoil energy of hydrogen and laser-cooling on the Lyman-α line are

prohibitive at this time, leaving rubidium as an attractive option.

For $l \geq 3$, the penetration quantum defect can be ignored since the overlap with the ionic core is essentially zero, leaving only the polarization quantum defect. In other words, quantum defect measurements of $l \geq 3$ can isolate the polarization quantum defect and hence a value for the polarizability of the ionic core of rubidium can be extracted. Experiments in which the quantum defects of g and h states in rubidium were measured to extract the polarizability have produced the best known results of the dipolar polarizability, α_d, 9.12(2) [48]. It is the uncertainty in α_d that makes the quantum defect correction one of the primary sources of uncertainty in Table 5.1. The uncertainty due to the quadrupolar energy level shift is negligible in the overall uncertainty budget, because of the $1/r^6$ dependence of that term [47, 48].

5.3   Stark and Zeeman Corrections

The second-order Stark shift leads to an uncertainty due to the uncertainty in the electric field amplitude. For molasses temperatures, the minimum electric field amplitude that we can apply to ensure circular-state stabilization is 2.9 mV/cm (see Table 2.5). Currently, the precision with which we know the electric field magnitude in the chamber is about $\pm$ 0.2 mV/cm for the x direction, $\pm$ 0.08 mV/cm in the y direction and $\pm$ 0.09 mV/cm in the z direction. This means that we can control the total electric field with a precision of $\pm$ 0.2 mV/cm which is about 7% of the necessary amplitude. This is more than sufficient for the precision measurements presented in Chapter IV, however, in the Rydberg constant measurement this would lead to a contribution to the relative uncertainty in ν of 1.0×10^{-11}, which is comparable to the contribution from the residual lattice shift. To achieve a precision comparable to the current precision of R_∞, we would need to know the electric field with a precision of at least 3.8%. We expect to improve the electric field uncertainty to 3% by using a lower noise voltage source to control the electric fields in the x direction. The values

shown in Table 5.1 assume this improvement.

The second-order Zeeman shift leads to an uncertainty due the error in the magnetic field amplitude. For molasses temperatures, the minimum field amplitude that we can apply to ensure circular-state stabilization is 6.7 μT (67 mG, see Table 2.5). The precision with which we know the magnetic field magnitude in the chamber is about 2.5 mG which means that the precision is about 3.7% of the necessary amplitude. This would lead to a relative uncertainty contribution of 7.5×10^{-13} which is below the current uncertainty of the Rydberg constant. The values displayed in Table 5.1 assume a 3.7% error in the field amplitude.

By performing the experiment under micro-gravity conditions, the second-order Stark and diamagnetic shift uncertainties can be decreased by four orders of magnitude (because the field magnitudes can be dropped by two orders of magnitude) and hence the uncertainties become insignificant within the total uncertainty budget.

5.4 Blackbody Radiation Correction

The blackbody shift is lowered three orders of magnitude by placing the system in thermal contact with liquid helium, which has a temperature of 4 K. Even so, at 300 K the blackbody radiation shift for the transition of interest is just -21 mHz, making this shift negligible for a wide range of typical experimental temperatures. The results of numerical calculations shown in Table 5.1 follow a similar procedure to that presented in [59]. However, we consider only bound states up to about n=300. This truncation of the basis set does not affect the results significantly. For example, if we compare results obtained when we consider states up to n=300 instead of n=750 in the calculation, at worst, the calculated shift for the individual states (about 2.4 kHz at 300 K and 0.42 Hz at 4 K) changes only by about 0.1 mHz at a temperature of 300 K and by nano-Hertz at a temperature of 4 K. This leads us to the conclusion that it is not necessary to include the continuum states in the calculations, which

is also reaffirmed in [59]. We treat the near-circular state as a sum of spherical states multiplied by their respective 3J symbols squared, as presented in Chapter II. The radiation field is taken to be isotropic inside our spectroscopy enclosure, since at the frequencies considered, the cavity density of states approaches that of free space. With this treatment, we obtain results comparable to those obtained in [59] for temperatures of 300 K. The radial matrix elements used in the calculations are correct to four significant figures. The main source of uncertainty for the shift presented in Table 5.1 is dictated by how well we know the temperature inside the spectroscopy enclosure. When calculating the blackbody shift uncertainty, it is assumed that the temperature is known to ± 0.5 K.

The main disturbance caused by the blackbody radiation is the broadening it induces on the spectral line due to thermally-induced decays and excitations. A precise determination of the location of our measured frequency is essential in obtaining a successful measurement of R_∞. Assuming a good signal-to-noise ratio, we expect to determine the line center to within 1/100 of the line-width. At a radiation temperature of 4 K, and for the states considered in this paper, the corresponding statistical uncertainty is 0.3 Hz, corresponding to a relative uncertainty of 3×10^{-12}.

5.5   Other sources of uncertainty

The following discussion shows that the remaining shifts listed in Table 5.1 present negligible uncertainties at the current level of precision (5.9×10^{-12}), but these are discussed here for completeness.

The finite-mass correction, which accounts for the non-infinite mass of the nucleus, consists of a dominant first-order term and several higher-order terms. The first order can be considered by multiplying the Rydberg constant by a factor of μ/m_e ($\mu = m_e M/(m_e + M)$) [46], where M is the Rb$^+$ mass. The correction is -605.08747 kHz, as shown in Table 5.1. The mass correction introduces an insignificant uncertainty

to our measurement since the mass of Rb^+ (84.911 245 324 a.u.) and that of the electron are well known (relative uncertainties of 4.4×10^{-8} [86] and 1.2×10^{-8} [34], respectively). The higher-order terms show up as factors of the form $(\mu/m_e)^\eta$ in the fine structure ($\eta = 1$), second-order Stark effect ($\eta = 3$), diamagnetic shift ($\eta = 1$), Lamb shift ($\eta = 2$) and hyperfine structure ($\eta = 1$) corrections. When the mass correction factor is considered for these, the shifts decrease by 3 mHz, 0.1 mHz, 6 μHz, 1 μHz, and 212 pHz, respectively. Since these differences are negligible, we do not carry out these corrections in the results shown in Table 5.1.

In contrast to measurements on low-lying states of hydrogen [29], through the use of circular states, we obtain low QED corrections, since the valence electron has zero probability of being in the vicinity of the nucleus, and the size of the Rydberg function becomes very large. The main source of uncertainty in the Lamb shift is the Bethe logarithm (relative uncertainty of 3.3×10^{-8} and 1.0×10^{-7} or less for the circular and near-circular states, respectively [56]), leading to a negligible uncertainty for our measurement.

Despite producing a relatively large shift, the fine-structure correction can be calculated very accurately since the fine-structure constant is well known (relative uncertainty of 2.3×10^{-10} [34]). As a result, the relative uncertainty introduced by the fine-structure shift is only 1.6×10^{-21}.

Even though the hyperfine-structure shift in itself is negligible, its uncertainty is nevertheless estimated. The main sources of this uncertainty are the electron mass, proton mass and Planck's constant (all of them with relative uncertainties of 1.2×10^{-8}) and the electron charge (relative uncertainty of 6.1×10^{-9}) [34]. The g-factors for the nucleus (0.000 293 640 0) and the electron (2.002 319 304 361 53) are also well known (relative uncertainties of 6.0×10^{-10} [58] and 2.6×10^{-13} [34], respectively).

Effective trapping of atoms in the lattice leads to zero first-order and negligible

second-order Doppler effects (see Fig. 2.10). As discussed in Chapter II, the first-order Stark and Zeeman shifts are zero for our transition. This is possible by choosing the lower and upper states so that either the shift on each individual state is zero (first-order Stark shift) or both states experience the same shift (first-order Zeeman shift).

5.6 Conclusion

The results shown in Table 5.1 lead to an expected relative uncertainty in the proposed measurement of the Rydberg constant in the low 10^{-11} range. In contrast with measurements performed with low-lying states of hydrogen (from which the best current uncertainty of 5.9×10^{-12} is obtained), our measurement is independent of nuclear effects and therefore could contribute to solving the proton radius puzzle [87]. In order to obtain a precision of 5.9×10^{-12} or better, we will need to ensure very good control of the lattice parameters, particularly the intensity ratios, to ensure "magic" lattice conditions. Another option is to further decrease the atomic sample temperature and hence the lattice depths. Additionally, the error in the electric field control along the x direction will need to be reduced to 3%. If the residual lattice shift uncertainty can be reduced to 2.0×10^{-12}, the expected total relative uncertainty will be 5.8×10^{-12}. It is towards this goal that the Rydberg constant measurement should proceed.

Table 5.1: Transition frequency shifts, relative transition shifts and relative uncertainties for ground-based experiment under conditions suitable for a kinetic temperature of 1 μK. Improved micro-gravity-conditions shifts and uncertainties are shown in square brackets for a temperature of 10 nK. The second-order Stark and diamagnetic shifts are lowered under these conditions since the field values are determined based on the kinetic temperature of the atoms. Here, I use $m_s = 1/2$. Blackbody radiation calculations done at 4 K.

Source	$\Delta\nu$	$\Delta\nu/\nu$	$\delta\Delta\nu/\nu$ $(\times 10^{-12})$
Residual Lattice Shift	0 (3) Hz [0 (0.1) Hz]	0	32 [1.0]
Dipolar Polarization Quantum Defect	120.1(3) Hz	1.283×10^{-9}	2.8
2$^{\text{nd}}$ order Stark	-6.8 (1) Hz [-0.73 (1) mHz]	-7.3×10^{-11}	4.4 [4.7×10^{-4}]
Diamagnetic	0.94 (4) Hz [94 (4) μHz]	1.0×10^{-11}	0.75 [7.5×10^{-5}]
Mass Correction	-605.08747 (3) kHz	6.4606271×10^{-6}	0.3
Lamb Shift	-84.1 (5) mHz	-8.98×10^{-13}	5.0×10^{-3}
Blackbody	0.64 (6) mHz	6.8×10^{-15}	6.2×10^{-4}
Quadrupolar Polarization QD	26 (5) μHz	2.8×10^{-10}	6.0×10^{-5}
2$^{\text{nd}}$ order Doppler	0.05 (7)nHz	5×10^{-22}	7.3×10^{-10}
Fine Structure	488.0332466612(5) Hz	$5.210818188587 \times 10^{-9}$	1.6×10^{-9}
Hyperfine Structure	32.89402(7) μHz	3.512153×10^{-16}	7.2×10^{-12}
1$^{\text{st}}$ order Stark	0 Hz	0	0
and Zeeman	0 Hz	0	0
1$^{\text{st}}$ order Doppler	0 Hz	0	0

CHAPTER VI

Discussion and Outlook

In this thesis, I have presented a proposal to measure the Rydberg constant with cold circular states of rubidium. A careful analysis of the sources of systematic for that precision measurement and the construction of the experimental setup for it were discussed. Moreover, a set of precision measurements of the hyperfine structure splittings of $nS_{1/2}$-states of rubidium-85 were presented. These achieved a hyperfine structure constant value which is almost an order of magnitude more precise than the best-precision values available in the literature. Furthermore, these experiments proved the usefulness of the experimental setup for precision measurements, in particular our capability to control magnetic fields at the location of the atoms well, an important feature for the future Rydberg constant measurement.

In this chapter I discuss the next steps to take towards performing the proposed Rydberg constant measurement along with several other precision measurements with Rydberg atoms that can be performed in the experimental setup. Additionally, I discuss how measuring R_∞ in microgravity can lower the resulting relative uncertainties by about an order of magnitude and review the impact of the proposed experiment on the proton size puzzle.

6.1 Future Work

The next milestone to achieve towards the proposed Rydberg constant measurement is to circularize the Rydberg states. After circularization is achieved in the experimental setup, a first trial of the Rydberg constant measurement could be done with microwave signals instead of the amplitude-modulated lattice. This would be a good proof-of-principle experiment which would provide valuable insights before performing the more-complex, proposed experiment with an amplitude-modulated lattice incorporated.

The Rydberg constant measurement and the experiments presented in this thesis are only the tip of the iceberg of the precision measurement experiments that can be done in the experimental chamber. First, a similar hyperfine structure splitting measurement could be performed for rubidium-87, where the typically larger splittings should lead to even better relative uncertainties. The rubidium source in our system contains both isotopes. In order to target rubidium-87 instead of rubidium-85, the only adjustment needed is simply changing the frequencies of the cooling and excitation lasers.

Second, based on preliminary g and h quantum defect measurements obtained in the system, the $l=0$ to 5 quantum defects could be measured with significantly better uncertainties than the currently available results [48–50]. This is for the most part thanks to the good electric and magnetic field controls available in the system. These measurements would consist of the usual three-photon excitation followed by one or two-photon microwave transitions to the final nl state of interest.

6.2 Solving the Proton Radius Puzzle

I have discussed an experimental method to help solve the proton radius puzzle using a cold-atom-based measurement of the Rydberg constant, which utilizes (near-

) circular Rydberg states and is thus free of QED shifts and sensitivity to nuclear charge overlap. Previous efforts to measure R_∞ with Rydberg atoms have encountered several experimental challenges which are addressed in this proposed measurement. The first-order Zeeman and Stark shifts are both zero, owing to appropriate selection of parabolic atomic states involved in the transition. With the use of cooling and trapping techniques, the interaction times are increased, leading to a reduction of the Fourier width. By using a new method of spectroscopy in modulated optical lattices, the Doppler broadening is eliminated. An implementation of the proposed experiment at atomic temperatures of about 1 μK is projected to yield a Rydberg constant value with an uncertainty in the low 10^{-11} range, limited almost exclusively by lattice-trap-induced shifts.

Since the proposed experiment differs from spectroscopy on low-lying atomic states in that it is entirely insensitive to the proton radius, it could help answer whether the discrepancy in the proton radius is due to an incorrect value of the Rydberg constant. To answer that question, a relative uncertainty in the low 10^{-11} range might be sufficient because the difference between the Rydberg constant from the muonic and electronic measurements is roughly 0.0004 m^{-1}. The expected limiting factor in the proposed R_∞ experiment, the trap-induced shift, could be very well addressed by performing the experiment under micro-gravity conditions.

6.3   Rydberg Constant Measurement in Microgravity

Performing atomic physics experiments in microgravity conditions is not a new idea [88–90]. Microgravity is attractive because it can offer longer interaction times and, in some cases, more compact experiments [88]. With the recent addition of the Cold Atom Laboratory (CAL) to the International Space Station (ISS), there are more opportunities to harvest the advantages of microgravity. A future iteration of the proposed Rydberg constant measurement is planned to be done in microgravity

conditions at CAL. This would lead to an expected relative uncertainty of the R_∞ value of at most $\approx 3 \times 10^{-12}$, which is almost a factor of two better than the current CODATA uncertatinty for R_∞ [34].

This improvement can be explained considering Fig. 2.8 from Chapter II, where the energy shift hierarchy is illustrated. In microgravity conditions, there is no need to employ a lattice to hold atoms from falling due to the very low gravity (although a shallow lattice would be used to drive transitions). Lowering the depth of the lattice, as shown in Fig. 2.8, has a domino effect through the field hierarchy for the experiment since it allows for lower magnetic and electric field amplitudes as well. This results in overall lower systematic relative uncertainties caused by the fields and the lattice (see the values in square brackets in Table 5.1), allowing for the significant improvement in the precision of R_∞.

APPENDIX

APPENDIX A

Incorporating an Optical Lattice on an Atom-Chip Experiment

Thanks to the support of the National Science Foundation (NSF) Graduate Research Opportunities Worldwide (GROW) grant I was able to spend five months working in the group of N.J. van Druten, R.J.C. Spreeuw, and H.B. van Linden van den Heuvell at the University of Amsterdam in the Netherlands. In this chapter I briefly introduce the setup I worked on during my time there, give the motivation for my particular project which consisted on incorporating a 1D optical lattice to the already existing setup and talk about what this new addition will be used for.

A.1   Introduction

The project I worked on is a Rydberg-atom system on a chip for quantum information processing applications. Rydberg atoms are attractive candidates for quantum information because the strengths of the their interactions can be tuned by changing simple experimental parameters such as principal quantum number [18]. Atom chips have the advantages of being compact, offering quick cooling and facilitating tighter atom traps. However, the surfaces of these chips can collect substrates of the alkali
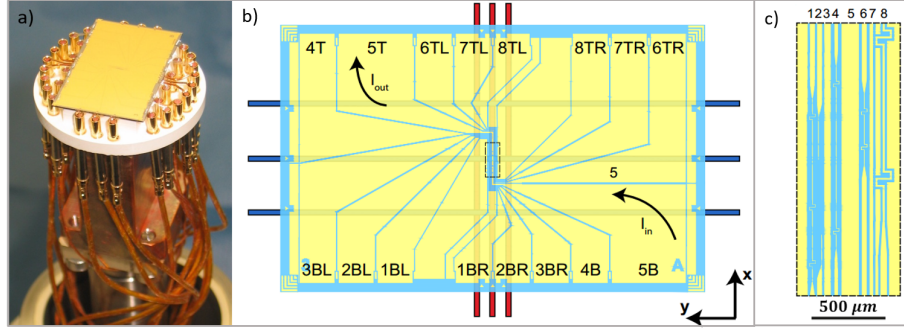
Figure A.1: a) Picture of atom chip being used in the experiment before being put inside the vacuum chamber. The dimensions are 16 mm × 25 mm. b) Schematics of the atom chip. Red and blue wires behind the chip are used in the early cooling stages to transfer cold atoms from a MOT that uses external current-carrying wires to a trap created by these chip wires. The chip wires are made out of gold. The surface of the chip is used as a mirror for one of the MOT beams. c) Shows in detail the center wires of the chip which are used for the last cooling stages which lead to Bose-Einstein condensates (BECs). Wire 5 is used for a Z trap, wire 3 is used for RF signals for evaporative cooling, and wire 4 is used for electric-field zeroing. The rest of the wires are not used in the work presented here, but some are capable of creating box traps of different lengths. For more details, see Ref. [6, 7].

metal being used which produce unwanted spatially imhomogenous electric fields. This phenomenon, combined with the high sensitivity of Rydberg atoms to electric fields, renders working with Rydberg atoms on atom chips a challenge. Nonetheless, some progress has been made [19, 91].

In our system [19], the electric-fields in two directions have been compensated such that only an electric-field gradient along the longitudinal direction of an elongated cold-atom cloud remains. Our goal is to use this electric-field gradient to spatially select lattice sites, a capability that would be necessary for quantum information processing.
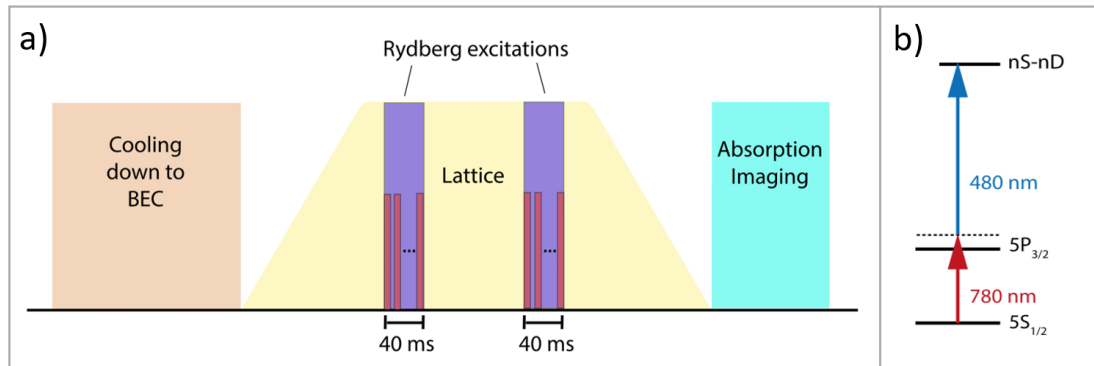
Figure A.2: Simplified schematics for the experimental timing sequence. The frequency of the red Rydberg laser is kept fixed during the first set of pulses while the frequency is scanned for the second set of pulses. (relative times not to scale).

A.2   Atom-Chip Experimental Setup

In this setup, we use rubidium-87 supplied by a dispenser inside a vacuum chamber. Using the chip and external coils, atoms are initially cooled down using a mirror magneto-optical trap (mirror-MOT) which consists of one pair of counter-propagating beams parallel to the surface of the chip and another pair reflected at a 45-degree angle from the gold-coated surface of the atom chip (see [19] for details). They are then transferred to an on-chip magnetic z-trap and evaporatively cooled, eventually forming a Bose-Einstein condensate (BEC) with temperatures of tens of nK about 100 μm away from the surface of the chip. The optical lattice is turned on adiabatically and remains on during the Rydberg excitation pulses (see Fig. A.2). The blue excitation beam is pulsed on for 40 ms while the red excitation beam is pulsed several times during that same time window, each individual pulse typically having a width between 4 and 20 μs. Population information is obtained through absorption imaging which employs an on-resonance beam perpendicular to the Rydberg excitation beams. Figure A.4a shows a sample absorption image of the obtained BEC. For more details on the experimental setup, please refer to [19].
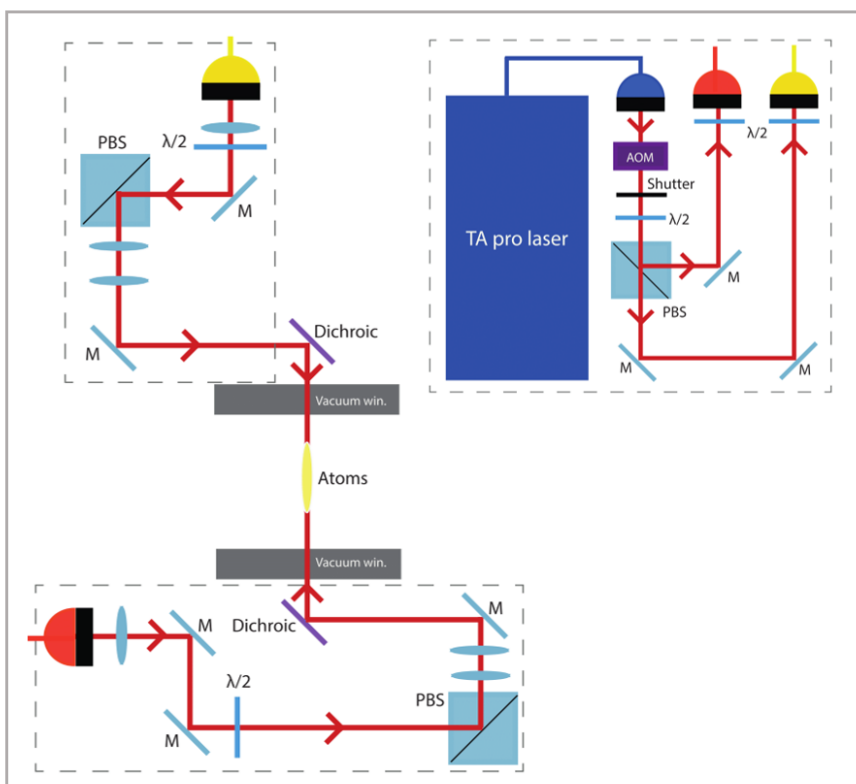
Figure A.3: Schematics showing the optical setup for the implemented 1D optical lattice.

A.3   1D Optical Lattice Implementation

My main task while working with the group in Amsterdam was to incorporate a one-dimensional optical lattice in their existing experimental setup. Figure A.3 shows the optical setup I put together.

The 860-nm light is provided by a Toptica TA pro laser with fiber-coupled output. An acousto-optic modulator (AOM) and a mechanical shutter control the lattice rise and decay times. I use the combination of the two to achieve smooth exponential rise and decay curves for lattice ramps since I must ensure adiabaticity while turning on and off. An arbitrary function generator (ARG) controls the RF input on the AOM. This input follows an inverted Gaussian shape (positive concavity) where at the minimum of the Gaussian the RF signal is zero and at the baseline of the Gaussian

the value is the maximum specified. In a single experimental cycle, the ARG sends out two Gaussian waveforms to the AOM and the shutter opens to catch the second half of the first Gaussian and closes after the first half of the second Gaussian. The end result is a smooth turn-on/turn-off with adjustable rise, decay and hold times.

To determine the timescales that are to be considered adiabatic, I follow [92] and use

$$\frac{dV_0}{dt} << \frac{16E_R^2}{\hbar}, \tag{A.1}$$

where V_0 is the lattice depth, t is the ramp time and $E_R^2 = \frac{\hbar^2 k^2}{2M}$ is the photon recoil energy with $k = 2\pi/\lambda$ and M the atomic mass of rubidium-87. In our case, $E_R = 2.105 \times 10^{-30}$ J and at first I assume $\Delta V_0 = 10E_R$. This yields $\Delta t \gg 31\mu s$. Therefore, I select ramp times of 100 μs. I keep the lattice on for about 345 ms, solely determined by the excitation stage duration (see Fig. A.2).

The first-order output of the AOM is split into two beams and sent through separate fibers. The output of each of these fibers forms one of the counter-propagating beams of the lattice inside the vacuum chamber (see Fig. A.3). The waist of the lattice beams after the fibers is selected such that the intensity over the length of the cold atom cloud does not change significantly and that it roughly matches the size of the cloud. The length of the atom cloud is about 1 mm which means the lattice beams need to have a Rayleigh range, $z_R = (\pi\omega_0^2)/\lambda$ (ω_0 is the beam waist), much larger than that value. At the same time, the waist of the lattice should be close to the waist of the atom cloud (50 μm) in order to avoid wasting lattice power. With these constraints I choose a trial lattice waist of 70 μm and check how much it changes over the length of the cloud with

$$\omega(z) = \omega_0\sqrt{1 + \left(\frac{z}{z_R}\right)^2}, \tag{A.2}$$

where ω is the size of the beam at a distance z along the propagation direction. This

Table A.1: Parameters of the implemented 1D optical lattice.

Parameter	Value
Wavelength	860 nm
Maximum depth	25 kHz
Beam waist	70 μm
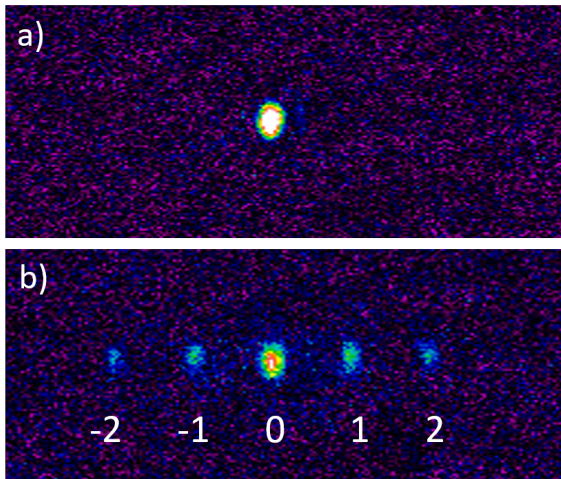
Figure A.4: Absorption images with a) BEC with no lattice present, and b) BEC with lattice turned on diabatically (momentum orders 0, $\pm$ 1 and $\pm$ 2 are visible).

results in a change in waist size of 0.11 μm corresponding to a change in intensity over the atom cloud of about 0.3%, which is negligible. Therefore, 70 μm is a good lattice waist for our purposes.

The alignment of the lattice is done in four main steps. First, the output beams from each fiber are aligned with the excitation beams that are known to be well aligned with the elongated atom cloud. Second, the coupling of one of the lattice beams into the opposite fiber is optimized. Then, one beam is blocked and the position of the BEC is checked for movement due to a dipole trap force. Since this is a radial force in the case of my Gaussian beams (points towards the maximum intensity region), if the BEC is not perfectly aligned with the beam, the cloud will experience a force towards the center of the beam. By adjusting the lattice beams to the point where moving a beam in any of the two directions causes the BEC to move in opposite directions, I
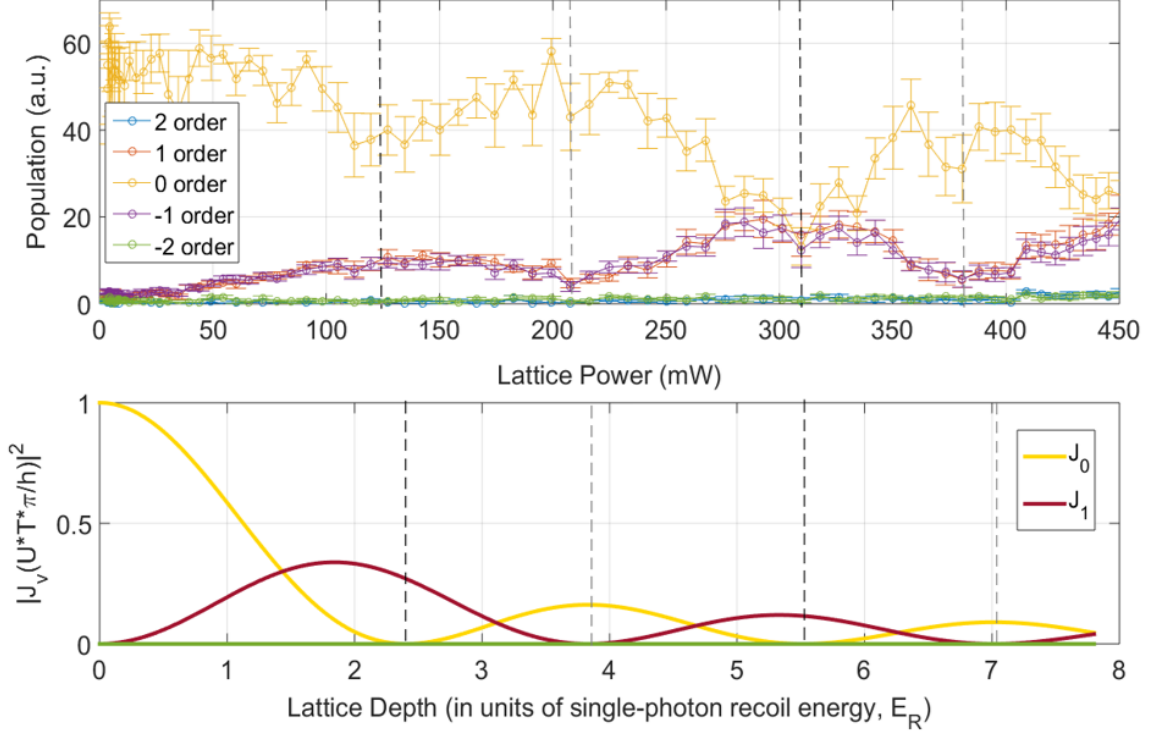
Figure A.5: Top panel: experimentally obtained population in each of the BEC orders as a function of lattice power. Bottom panel: calculated BEC orders' population as a function lattice depth obtained using Eq. A.3. Error bars on the top plot are due to fluctuations between repeated scans. The dashed lines mark the zeros of the curves.

can obtain very good alignment of each beam.

Finally, the alignment of both arms is optimized by obtaining Kapitza-Dirac scattering [92, 93]. When the lattice is turned on diabatically (in this case, a square pulse with duration of 100 μs), the resulting lattice-atom state can be spatially separated into a number of clouds with different momentum orders (Kapitza-Dirac scattering, see Fig. A.4). The population in the nth momentum order follows a Bessel function of the first kind [94]

$$P_n = J_n^2 \left(\frac{V_0 T_{pulse}}{2\hbar} \right),$$ (A.3)

where T_{pulse} is the lattice pulse duration. I used this to calibrate the lattice depth by taking images as the lattice power (and hence its depth) is changed.
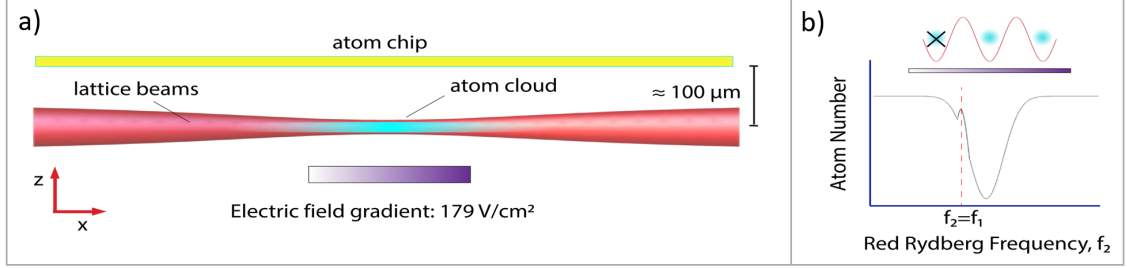
Figure A.6: a) Schematics of experimental setup highlighting the orientation of the lattice beams and atom cloud with respect to the electric field gradient along the x-direction. b) A sample spectrum that would result from the timing sequence. The vertical axis is the number of atoms in the ground state. The hole burning feature, which occurs at the frequency of the first red excitation pulse, f_1, would indicate the Stark shift and hence the specific location along the atom cloud being selectively addressed.

From Fig. A.5, I extract the four minima from the experimental and theoretical plots and fit a linear curve through them. This yields the calibration function $V_0 = 0.018P$, where V_0 is the lattice depth in units of E_R (recoil energy) and P is the lattice power in mW. Hence, we can achieve a maximum depth of about 25 kHz with about 230 mW on each lattice beam.

A.4 Future Work: Spatially Probing Lattice Sites

The optical lattice has been implemented to improve the longitudinal confinement of the atoms along the longitudinal direction, resulting in a linear array of traps. The existing electric-field gradient along the x-direction leads to a position-dependent Stark shift which causes broadening of the Rydberg spectrum [19]. However, this shift can also be used to selectively excite Rydberg atoms along this array of cold atoms.

This can be shown by first exciting atoms slightly off-resonantly with a set of Rydberg pulses, which depletes the ground-state atoms at a specific location along the atom cloud. With a second set of Rydberg pulses, where the red Rydberg beam

is scanned (see Fig. A.6), the entirety of the atom cloud is addressed but the location where the ground-state atoms were depleted by the first pulse does not yield any losses. This results in a hole burning spectrum (see Fig. A.6b). This spatially-selective excitation could be useful for quantum information.

BIBLIOGRAPHY

BIBLIOGRAPHY

[1] S. E. Anderson, K. C. Younge, and G. Raithel. Trapping Rydberg atoms in an optical lattice. *Phys. Rev. Lett.*, 107:263001, Dec 2011. doi: 10.1103/PhysRevLett.107.263001.

[2] K. Moore. High-precision spectroscopy using Rydberg atoms. 2017.

[3] H. J. Lewandowski, D. M. Harber, D. L. Whitaker, and E. A. Cornell. Simplified system for creating a Bose–Einstein condensate. *Journal of low temperature physics*, 132(5-6):309–367, 2003.

[4] H. J. Metcalf and P. Van der Straten. Laser cooling and trapping of neutral atoms. *The Optics Encyclopedia: Basic Foundations and Practical Applications*, 2007.

[5] D. P Fahey and M. W. Noel. Excitation of Rydberg states in rubidium with near infrared diode lasers. *Optics Express*, 19(18):17002–17012, 2011.

[6] N. V. Cisternas San Martín. Experiments with Rydberg atoms on a current-carrying atom chip. 2018.

[7] J. de Hond. Interacting Rydberg atoms on a chip. 2018.

[8] J. J. Balmer. About the spectral lines of hydrogen. *Annalen der Physik*, 261(5): 80–87, 1885.

[9] R. F. Stebbings. High Rydberg atoms: Newcomers to the atomic physics scene. *Science*, 193(4253):537–542, 1976.

[10] C. J Foot et al. *Atomic physics*, volume 7. Oxford University Press, 2005.

[11] P. D. Lett, R. N. Watts, C. I. Westbrook, W. D. Phillips, P. L. Gould, and H. J. Metcalf. Observation of atoms laser cooled below the doppler limit. *Phys. Rev. Lett.*, 61:169–172, Jul 1988. doi: 10.1103/PhysRevLett.61.169.

[12] Ch. Salomon, J. Dalibard, W. D. Phillips, A. Clairon, and S Guellati. Laser cooling of cesium atoms below 3 μk. *EPL (Europhysics Letters)*, 12(8):683, 1990.

[13] K.l B. Davis, M.-O. Mewes, M. R. Andrews, N. J. Van Druten, D. S. Durfee, D. M. Kurn, and W. Ketterle. Bose-Einstein condensation in a gas of sodium atoms. *Phys. Rev. Lett.*, 75(22):3969, 1995.

[14] M. H. Anderson, J. R. Ensher, M. R. Matthews, C. E. Wieman, and E. A. Cornell. Observation of Bose-Einstein condensation in a dilute atomic vapor. *science*, 269(5221):198–201, 1995.

[15] S. Haroche. Cavity quantum electrodynamics: a review of Rydberg atom-microwave experiments on entanglement and decoherence. In *AIP Conference Proceedings*, volume 464, pages 45–66. AIP, 1999.

[16] C. H. Greene, A. S. Dickinson, and H. R. Sadeghpour. Creation of polar and nonpolar ultra-long-range Rydberg molecules. *Phys. Rev. Lett.*, 85(12):2458, 2000.

[17] D. Jaksch, J. I. Cirac, P. Zoller, S. L. Rolston, R. Côté, and M. D. Lukin. Fast quantum gates for neutral atoms. *Phys. Rev. Lett.*, 85(10):2208, 2000.

[18] M. Saffman, T. G. Walker, and K. Mølmer. Quantum information with Rydberg atoms. *Reviews of Modern Physics*, 82(3):2313, 2010.

[19] N. Cisternas, J. de Hond, G. Lochead, R. J. C. Spreeuw, H. B. van Linden van den Heuvell, and N. J. van Druten. Characterizing the local vectorial electric field near an atom chip using Rydberg-state spectroscopy. *Phys. Rev. A*, 96(1):013425, 2017.

[20] J. A. Sedlacek, A. Schwettmann, H. Kübler, R. Löw, T. Pfau, and J. P. Shaffer. Microwave electrometry with Rydberg atoms in a vapour cell using bright atomic resonances. *Nature Physics*, 8(11):819, 2012.

[21] D. A. Anderson, S. A. Miller, G. Raithel, J. A. Gordon, M. L. Butler, and C. L. Holloway. Optical measurements of strong microwave fields with Rydberg atoms in a vapor cell. *Phys. Rev. Applied*, 5:034003, Mar 2016. doi: 10.1103/PhysRevApplied.5.034003.

[22] S. A. Miller, D. A. Anderson, and G. Raithel. Radio-frequency-modulated Rydberg states in a vapor cell. *New Journal of Physics*, 18(5):053017, 2016.

[23] K. R. Moore, S. E. Anderson, and G. Raithel. Forbidden atomic transitions driven by an intensity-modulated laser trap. 2015.

[24] T. F. Gallagher. *Rydberg Atoms*.

[25] J.J. Sakurai and J. Napolitano. *Modern Quantum Mechanics*. Pearson, 1994.

[26] N. Bohr. Atomic theory and mechanics. *Nature*, 116(2927):845, 1925.

[27] J. Mitroy, M. S. Safronova, and C. W. Clark. Theory and applications of atomic and ionic polarizabilities. *J. Phys. B*, 43(20):202001, 2010.

[28] E. Richard Cohen and Barry N. Taylor. The 1973 least-squares adjustment of the fundamental constants. *Journal of Physical and Chemical Reference Data*, 2 (4):663–734, 1973.

[29] P. J. Mohr and B. N. Taylor. Codata recommended values of the fundamental physical constants: 2002*. *Rev. Mod. Phys.*, 77:1–107, Mar 2005. doi: 10.1103/RevModPhys.77.1.

[30] E. Cohen and B. Taylor. The 1986 CODATA recommended values of the fundamental physical constants. *Journal of Research*, 92:85–95, 1987.

[31] P. J. Mohr and B. N. Taylor. Codata recommended values of the fundamental physical constants: 1998. *Journal of Physical and Chemical Reference Data*, 28 (6):1713–1852, 1999.

[32] P. J. Mohr, B. N. Taylor, and D. B. Newell. Codata recommended values of the fundamental physical constants: 2006. *Journal of Physical and Chemical Reference Data*, 80(3):633–1284, 2008.

[33] P. J. Mohr, B. N. Taylor, and D. B. Newell. Codata recommended values of the fundamental physical constants: 2010*. *Rev. Mod. Phys.*, 84:1527–1605, Nov 2012. doi: 10.1103/RevModPhys.84.1527.

[34] P. J. Mohr, D. B. Newell, and B. N. Taylor. Codata recommended values of the fundamental physical constants: 2014. *Journal of Physical and Chemical Reference Data*, 45(4):043102, 2016.

[35] J. C. De Vries. *A Precision Millimeter-Wave Measurement of the Rydberg Frequency.* PhD thesis, Department of Physics, Massachusetts Institute of Technology, USA, 2002.

[36] J. Hare, A. Nussenzweig, C. Gabbanini, M. Weidemuller, P. Goy, M. Gross, and S. Haroche. Toward a Rydberg constant measurement on circular atoms. *Instrumentation and Measurement, IEEE Transactions on*, 42(2):331–334, April 1993. ISSN 0018-9456. doi: 10.1109/19.278576.

[37] R. Pohl, A. Antognini, F. Nez, F. D. Amaro, F. Biraben, J. M. R. Cardoso, D. S. Covita, A. Dax, S. Dhawan, L. M. P. Fernandes, A. Giesen, T. Graf, T W. Hänsch, P. Indelicato, L. Julien, C.Y. Kao, P. Knowles, E.O. Le Bigot, Y.W. Liu, J. A. M. Lopes, L. Ludhova, C. M. B. Monteiro, F. Mulhauser, T. Nebel, P. Rabinowitz, J. M. F. dos Santos, L. A. Schaller, K. Schuhmann, C. Schwob, D. Taqqu, J. F. C. A. Veloso, and F. Kottmann. The size of the proton. 2010.

[38] R. J. Hill. Review of experimental and theoretical status of the proton radius puzzle. In *EPJ Web of Conferences*, volume 137, page 01023. EDP Sciences, 2017.

[39] R. Pohl, F. Nez, T. Udem, A. Antognini, A. Beyer, H. Fleurbaey, A. Grinin, T. W. Hänsch, L. Julien, F. Kottmann, et al. Deuteron charge radius and Rydberg constant from spectroscopy data in atomic deuterium. *Metrologia*, 54 (2):L1, 2017.

[40] R. Pohl, F. Nez, L. M. P. Fernandes, F. D. Amaro, F. Biraben, J. M. R. Cardoso, D. S. Covita, A. Dax, S. Dhawan, M. Diepold, et al. Laser spectroscopy of muonic deuterium. *Science*, 353(6300):669–673, 2016.

[41] H. Fleurbaey, S. Galtier, S. Thomas, M. Bonnaud, L. Julien, F.s Biraben, F. Nez, M. Abgrall, and J. Guéna. New measurement of the 1 s- 3 s transition frequency of hydrogen: Contribution to the proton charge radius puzzle. *Phys. Rev. Lett.*, 120(18):183001, 2018.

[42] A. Beyer, L. Maisenbacher, A. Matveev, R. Pohl, K. Khabarova, A. Grinin, T. Lamour, D. C. Yost, T. W. Hänsch, N. Kolachevsky, et al. The Rydberg constant and proton size from atomic hydrogen. *Science*, 358(6359):79–85, 2017.

[43] U. D. Jentschura, P. J. Mohr, and J. N. Tan. Fundamental constants and tests of theory in Rydberg states of one-electron ions. *Journal of Physics B: Atomic, Molecular and Optical Physics*, 43(7):074002, 2010.

[44] S. Strauch. The muon proton scattering experiment (muse) at the paul scherrer institute. *Bulletin of the American Physical Society*, 62, 2017.

[45] U. D. Jentschura, P. J. Mohr, J. N. Tan, and B. J. Wundt. Fundamental constants and tests of theory in Rydberg states of hydrogenlike ions. *Phys. Rev. Lett.*, 100: 160404, Apr 2008. doi: 10.1103/PhysRevLett.100.160404.

[46] H.A. Bethe, , and E.E. Salpeter. *Quantum Mechanics of One- and Two-electron Atoms*. Spinger-Verlag, Berlin, 1957.

[47] R. R. Freeman and D.l Kleppner. Core polarization and quantum defects in high-angular-momentum states of alkali atoms. *Phys. Rev. A*, 14:1614–1619, Nov 1976. doi: 10.1103/PhysRevA.14.1614.

[48] J. Lee, J. Nunkaew, and T. F. Gallagher. Microwave spectroscopy of the cold rubidium (n+1)d$_{5/2}$ → ng and nh transitions. *Phys. Rev. A*, 94(2):022505, 2016.

[49] W. Li, I. Mourachko, M. W. Noel, and T. F. Gallagher. Millimeter-wave spectroscopy of cold Rb Rydberg atoms in a magneto-optical trap: Quantum defects of the *ns*, *np*, and *nd* series. *Phys. Rev. A*, 67:052502, May 2003. doi: 10.1103/PhysRevA.67.052502.

[50] J. Han, Y. Jamil, D. V. L. Norum, P. J. Tanner, and T. F. Gallagher. Rb *nf* quantum defects from millimeter-wave spectroscopy of cold ^{85}Rb Rydberg atoms. *Phys. Rev. A*, 74:054502, Nov 2006. doi: 10.1103/PhysRevA.74.054502.

[51] L. J. Curtis. *Atomic structure and lifetimes: a conceptual approach*. Cambridge University Press, 2003.

[52] H. Eissa and U. Opik. The polarization of a closed-shell core of an atomic system by an outer electron: I. a correction to the adiabatic approximation. 1967.

[53] S. Krishnagopal, S. Narasimhan, and S. H. Patil. Multipolar polarizabilities and Rydberg states. *The Journal of chemical physics*, 83(11):5772–5777, 1985.

[54] G. F. Smoot. Thomas precession, February 1998.

[55] W. E. Lamb Jr and R. C. Retherford. Fine structure of the hydrogen atom by a microwave method. *Physical Review*, 72(3):241, 1947.

[56] G. W. Erickson. Energy levels of one-electron atoms. *J. Phys. Chem. Ref. Data*, 6:831–869, 1977.

[57] J. D. Jackson. Classical electrodynamics, 1999.

[58] E. Arimondo, M. Inguscio, and P. Violino. Experimental determinations of the hyperfine structure in the alkali atoms. *Rev. Mod. Phys.*, 49:31–75, Jan 1977. doi: 10.1103/RevModPhys.49.31.

[59] J. W. Farley and W. H. Wing. Accurate calculation of dynamic stark shifts and depopulation rates of Rydberg energy levels induced by blackbody radiation. hydrogen, helium, and alkali-metal atoms. *Phys. Rev. A*, 23:2397–2424, May 1981. doi: 10.1103/PhysRevA.23.2397.

[60] S. K. Dutta, J. R. Guest, D. Feldbaum, A. Walz-Flannigan, and G. Raithel. Ponderomotive optical lattice for Rydberg atoms. *Phys. Rev. Lett.*, 85:5551–5554, Dec 2000. doi: 10.1103/PhysRevLett.85.5551.

[61] H. Friedrich. *Theoretical Atomic Physics*. Spinger-Verlag, Berlin Heidelberg, 1991.

[62] K. C. Younge, S. E. Anderson, and G. Raithel. Adiabatic potentials for Rydberg atoms in a ponderomotive optical lattice. *New Journal of Physics*, 12(2):023031, 2010.

[63] D. Boiron, A. Michaud, P. Lemonde, Y. Castin, Ch. Salomon, S. Weyers, K. Szymaniec, L. Cognet, and A. Clairon. Laser cooling of cesium atoms in gray optical molasses down to 1.1 μk. *Phys. Rev. A*, 53:R3734–R3737, Jun 1996. doi: 10.1103/PhysRevA.53.R3734.

[64] K. R. Moore and G. Raithel. Probe of Rydberg-atom transitions via an amplitude-modulated optical standing wave with a ponderomotive interaction. *Phys. Rev. Lett.*, 115(16):163003, 2015.

[65] B. Knuffman and G. Raithel. Multipole transitions of Rydberg atoms in modulated ponderomotive potentials. *Phys. Rev. A*, 75:053401, May 2007. doi: 10.1103/PhysRevA.75.053401.

[66] K. R. Moore and G. Raithel. Measurement of the ^{85}Rb ng-series quantum defect using $\Delta l = 0$ microwave spectroscopy, 2016.

[67] Rydberg-atom trajectories in a ponderomotive optical lattice.

[68] W. Hong and O. J. Painter. Design and characterisation of a Littrow configuration external cavity diode laser. *California Institute of Technology*, 2005.

[69] D. W. Preston. Doppler-free saturated absorption: Laser spectroscopy. *American Journal of Physics*, 64(11):1432–1436, 1996.

[70] M. J. Willis. Proportional-integral-derivative control. *Dept. of Chemical and Process Engineering University of Newcastle*, 1999.

[71] P. R. Berman and V. S. Malinovsky. *Principles of Laser Spectroscopy and Quantum Optics*. Princeton University Press, 2011.

[72] K. Dieckmann, R. J. C. Spreeuw, M Weidemüller, and J. T. M. Walraven. Two-dimensional magneto-optical trap as a source of slow atoms. *Phys. Rev. A*, 58 (5):3891, 1998.

[73] Yu. B. Ovchinnikov. Compact magneto-optical sources of slow atoms. *Optics communications*, 249(4-6):473–481, 2005.

[74] S. Chu, L. Hollberg, J. E. Bjorkholm, A. Cable, and A. Ashkin. Three-dimensional viscous confinement and cooling of atoms by resonance radiation pressure. *Phys. Rev. Lett.*, 55(1):48, 1985.

[75] D. J. Thompson and R. E. Scholten. Narrow linewidth tunable external cavity diode laser using wide bandwidth filter. *Review of Scientific Instruments*, 83(2): 023107, 2012.

[76] E Hansis, T Cubel, J-H Choi, JR Guest, and G Raithel. Simple pressure-tuned fabry–pérot interferometer. *Review of Scientific Instruments*, 76(3):033105, 2005.

[77] P. Nussenzveig, F. Bernardot, M. Brune, J. Hare, J. M. Raimond, S. Haroche, and W. Gawlik. Preparation of high-principal-quantum-number "circular" states of rubidium. *Phys. Rev. A*, 48:3991–3994, Nov 1993. doi: 10.1103/PhysRevA.48.3991.

[78] R. G. Hulet and D. Kleppner. Rydberg atoms in "circular" states. *Phys. Rev. Lett.*, 51(16):1430, 1983.

[79] J. Hare, M. Gross, and P. Goy. Circular atoms prepared by a new method of crossed electric and magnetic fields. *Phys. Rev. Lett.*, 61:1938–1941, Oct 1988. doi: 10.1103/PhysRevLett.61.1938.

[80] R. Dumke, M. Volk, T. Müther, F. B. J. Buchkremer, G. Birkl, and W. Ertmer. Micro-optical realization of arrays of selectively addressable dipole traps: a scalable configuration for quantum computation with atomic qubits. *Phys. Rev. Lett.*, 89(9):097903, 2002.

[81] TP Harty, DTC Allcock, C J Ballance, L Guidoni, HA Janacek, NM Linke, DN Stacey, and DM Lucas. High-fidelity preparation, gates, memory, and read-out of a trapped-ion quantum bit. *Phys. Rev. Lett.*, 113(22):220501, 2014.

[82] A. Tauschinsky, R. Newell, H. B. van Linden van den Heuvell, and R. J. C. Spreeuw. Measurement of ^{87}Rb Rydberg-state hyperfine splitting in a room-temperature vapor cell. *Phys. Rev. A*, 87(4):042522, 2013.

[83] N. Cisternas, J. de Hond, G. Lochead, R. J. C. Spreeuw, H. B. van Linden van den Heuvell, and N. J. van Druten. Characterizing the local vectorial electric field near an atom chip using Rydberg-state spectroscopy. *Phys. Rev. A*, 96(1):013425, 2017.

[84] N. Thaicharoen, A. Schwarzkopf, and G Raithel. Measurement of the van der Waals interaction by atom trajectory imaging. *Phys. Rev. A*, 92(4):040701, 2015.

[85] H. J. Metcalf and P. Van der Straten. *Laser cooling and trapping.* Springer Science & Business Media, 2012.

[86] B. J. Mount, M. Redshaw, and E. G. Myers. Atomic masses of ^{6}Li, ^{23}Na, ^{39,41}K, ^{85,87}Rb, and ^{133}Cs. 2010.

[87] J. C. Bernauer and R. Pohl. The proton radius problem. *Scientific American*, 310(2):32–39, 2014.

[88] Ch. Salomon, N. Dimarcq, M. Abgrall, A. Clairon, Ph. Laurent, P. Lemonde, G. Santarelli, P. Uhrich, L. G. Bernier, G. Busca, et al. Cold atoms in space and atomic clocks: Aces. *Comptes Rendus de l'Académie des Sciences-Series IV-Physics*, 2(9):1313–1330, 2001.

[89] T. van Zoest, N. Gaaloul, Y. Singh, H. Ahlers, W. Herr, S. T. Seidel, W. Ertmer, E. Rasel, M. Eckart, E. Kajari, et al. Bose-Einstein condensation in microgravity. *Science*, 328(5985):1540–1543, 2010.

[90] H. Müntinga, H. Ahlers, M. Krutzik, A. Wenzlawski, S. Arnold, D. Becker, K. Bongs, H. Dittus, H. Duncker, N. Gaaloul, et al. Interferometry with Bose-Einstein condensates in microgravity. *Phys. Rev. Lett.*, 110(9):093602, 2013.

[91] D. Davtyan, S. Machluf, M. L. Soudijn, J. B. Naber, N. J. Van Druten, H. B. van Linden van den Heuvell, and R. J. C. Spreeuw. Controlling stray electric fields on an atom chip for experiments on Rydberg atoms. *Phys. Rev. A*, 97(2): 023418, 2018.

[92] J. H. Denschlag, J. E. Simsarian, H. Häffner, C. McKenzie, A. Browaeys, D. Cho, K. Helmerson, S. L. Rolston, and W. D. Phillips. A Bose-Einstein condensate in an optical lattice. *J. Phys. B*, 35(14):3095, 2002.

[93] Yu. B. Ovchinnikov, J. H. Müller, M. R. Doery, E. J. D. Vredenbregt, K. Helmerson, S. L. Rolston, and W. D. Phillips. Diffraction of a released Bose-Einstein condensate by a pulsed standing light wave. *Phys. Rev. Lett.*, 83(2):284, 1999.

[94] J. H. Huckans, I. B. Spielman, B. L. Tolra, W. D. Phillips, and J. V. Porto. Quantum and classical dynamics of a Bose-Einstein condensate in a large-period optical lattice. *Phys. Rev. A*, 80(4):043609, 2009.